



**HAL**  
open science

## NMR Characterization of the Influence of Zinc(II) Ions on the Structural and Dynamic Behavior of the New Delhi Metallo- $\beta$ -Lactamase-1 and on the Binding with Flavonols as Inhibitors

Gwladys Rivière, Saoussen Oueslati, Maud Gayral, Jean-Bernard Créchet, Naïma Nhiri, Eric Jacquet, Jean-Christophe Cintrat, François Giraud, Carine van Heijenoort, Ewen Lescop, et al.

### ► To cite this version:

Gwladys Rivière, Saoussen Oueslati, Maud Gayral, Jean-Bernard Créchet, Naïma Nhiri, et al.. NMR Characterization of the Influence of Zinc(II) Ions on the Structural and Dynamic Behavior of the New Delhi Metallo- $\beta$ -Lactamase-1 and on the Binding with Flavonols as Inhibitors. ACS Omega, 2020, 5 (18), pp.10466-10480. 10.1021/acsomega.0c00590 . hal-02604220

**HAL Id: hal-02604220**

**<https://hal.science/hal-02604220>**

Submitted on 16 May 2020

**HAL** is a multi-disciplinary open access archive for the deposit and dissemination of scientific research documents, whether they are published or not. The documents may come from teaching and research institutions in France or abroad, or from public or private research centers.

L'archive ouverte pluridisciplinaire **HAL**, est destinée au dépôt et à la diffusion de documents scientifiques de niveau recherche, publiés ou non, émanant des établissements d'enseignement et de recherche français ou étrangers, des laboratoires publics ou privés.

# NMR Characterization of the Influence of Zinc(II) Ions on the Structural and Dynamic Behavior of the New Delhi Metallo- $\beta$ -Lactamase-1 and on the Binding with Flavonols as Inhibitors

Gwladys Rivière, Saoussen Oueslati, Maud Gayral, Jean-Bernard Créchet, Naïma Nhiri, Eric Jacquet, Jean-Christophe Cintrat, François Giraud, Carine van Heijenoort, Ewen Lescop, Stéphanie Pethe, Bogdan I. Iorga, Thierry Naas,\* Eric Guittet, and Nelly Morellet\*



Cite This: *ACS Omega* 2020, 5, 10466–10480



Read Online

ACCESS |



Metrics & More

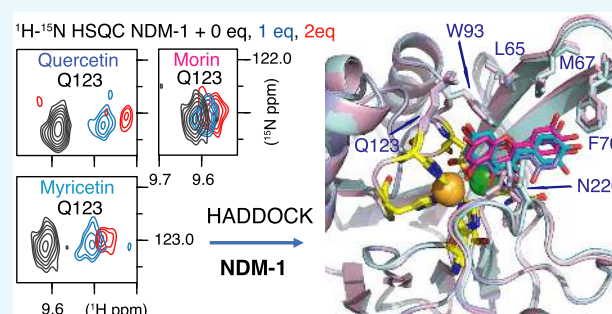


Article Recommendations



Supporting Information

**ABSTRACT:** New Delhi metallo- $\beta$ -lactamase-1 (NDM-1) has recently emerged as a global threat because of its ability to confer resistance to all common  $\beta$ -lactam antibiotics. Understanding the molecular basis of  $\beta$ -lactam hydrolysis by NDM is crucial for designing NDM inhibitors or  $\beta$ -lactams resistant to their hydrolysis. In this study, for the first time, NMR was used to study the influence of Zn(II) ions on the dynamic behavior of NDM-1. Our results highlighted that the binding of Zn(II) in the NDM-1 active site induced several structural and dynamic changes on active site loop 2 (ASL2) and L9 loops and on helix  $\alpha$ 2. We subsequently studied the interaction of several flavonols: morin, quercetin, and myricetin were identified as natural and specific inhibitors of NDM-1. Quercetin conjugates were also synthesized in an attempt to increase the solubility and bioavailability. Our NMR investigations on NDM-1/ flavonol interactions highlighted that both Zn(II) ions and the residues of the NDM-1 ASL1, ASL2, and ASL4 loops are involved in the binding of flavonols. This is the first NMR interaction study of NDM-1/inhibitors, and the models generated using HADDOCK will be useful for the rational design of more active inhibitors, directed against NDM-1.



## INTRODUCTION

Gram-negative bacteria (GNB), particularly *Enterobacteriales*, *Pseudomonas aeruginosa*, and *Acinetobacter baumannii*, have reemerged as major actors in antimicrobial resistance worldwide.<sup>1,2</sup> Pandrug resistance (PDR) and multidrug resistance (MDR) have been observed among them.<sup>3</sup> Currently,  $\beta$ -lactamase-mediated resistance does not spare even the newest and most potent  $\beta$ -lactams (carbapenems), whose activity is challenged by the class B metallo- $\beta$ -lactamases (MBLs) and by the serine-carbapenemases (classes A and D).<sup>4–6</sup> MBLs are by far the  $\beta$ -lactamases of greatest concern because there are currently not clinically useful inhibitors for this class.<sup>6</sup> The spread of MBL genes among *Enterobacteriales* is of great clinical concern, given the importance of these pathogens as causes of nosocomial and community-acquired infections and the fact that MBLs inactivate expanded-spectrum cephalosporins and carbapenems, the major antibiotics used to treat infections due to *Enterobacteriales*.

$\beta$ -Lactamases catalyze the opening of the  $\beta$ -lactam ring, thereby inactivating  $\beta$ -lactam antibiotics.<sup>7</sup> Based on their amino acid sequence, the  $\beta$ -lactamases have been grouped into four major classes. Classes A, C, and D use an active site serine to catalyze hydrolysis, while class B (MBLs) requires one or

two zinc ions (Zn(II)) for their activity.<sup>8</sup> Based on the structural diversity of the active sites, such as differences in metal content and residues involved in metal coordination, MBLs have been divided into three subclasses: B1, B2, and B3.<sup>8</sup>

The pandemic New Delhi metallo- $\beta$ -lactamase-1 (NDM-1) disseminating worldwide in Gram-negative organisms threatens to take medicine back into the preantibiotic era since mortality associated with infections caused by these “superbugs” is very high and the choices of treatment are very limited. NDM-1, a member of subclass B1 MBLs, has rapidly spread worldwide on several MDR plasmids.<sup>9–12</sup> Numerous NDM-1 structures, complexed or not with metal ions and a variety of substrates, are available in the Protein Data Bank (PDB). NDM-1 adopts the general  $\alpha\beta/\beta\alpha$  fold of MBLs,<sup>13–18</sup> consisting of two central  $\beta$ -sheets and five solvent-exposed  $\alpha$ -

Received: February 10, 2020

Accepted: April 15, 2020

Published: April 28, 2020



helices. Numerous experimental and theoretical studies have been conducted to define the catalytic mechanism of NDM-1.<sup>14,18–22</sup> The active site is a hydrophobic cavity, which consists of two Zn(II) (Zn1 and Zn2) surrounded by five mobile labeled loops called active site loops (ASL1–5) responsible for substrate binding and specificity.<sup>14</sup> Zn1 and Zn2 are coordinated, respectively, by H120, H122, H189 and D124, C208, H250, with different affinities,<sup>23,24</sup> and by a water molecule located between these two Zn(II) ions, which acts as a nucleophile during  $\beta$ -lactam hydrolysis.

Like all MBLs, NDM-1 is not sensitive to any commercially available serine- $\beta$ -lactamase inhibitors. The development of chemically active inhibitors for the NDM-1 enzyme has been extensively undertaken.<sup>17,25–46</sup> The metal chelator edetate disodium (EDTA) has also been shown to inactivate the enzymatic activity of NDM-1 by removing the catalytically required Zn(II) ions,<sup>17,47</sup> but its toxicity impedes its clinical use. Potent inhibitors of NDM-1 have also been identified through virtual screening of natural compounds, such as the natural product aspergillomaramine, analogous to the metal-ion chelator EDTA,<sup>48,49</sup> baicalin,<sup>50</sup> and magnolol, which has a significant impact on NDM-1 enzyme activity *in vitro*,<sup>51</sup> and hesperidin, which acts directly on key residues near the active site of NDM-1.<sup>52</sup>

To better understand the impact of Zn(II) on the structural and dynamic behavior of NDM-1, we analyzed this protein in the presence and absence of Zn(II) by NMR. We showed that not only loops carrying the zinc ligands undergo a significant change in their dynamic behavior but also other regions far from the active site. In addition, we identified three flavonols: morin, quercetin, and myricetin as specific inhibitors of NDM-1 activity. Flavonols are naturally occurring polyphenolic compounds that are ubiquitous in a wide range of vascular plants.<sup>53</sup> They are a class of flavonoids that are recognized to have a variety of biological activities and important therapeutic applications.<sup>54–62</sup> We used NMR spectroscopy to map the site of interaction on NDM-1 during complexation to the three flavonols. Our results show that the NDM-1 loops, ASL1, ASL2, and ASL4 are perturbed by flavonol binding and that Zn(II) ions are involved in their binding. Our NMR data provide support for the NDM-1/flavonol complex models, generated using the HADDOCK program, which will be useful for the rational design of ligands with increased activity.

## RESULTS AND DISCUSSION

**NDM-1 Is Stabilized in the Presence of Zn(II).** We verified by NMR spectroscopy and thermal shift experiments that NDM-1 was produced without Zn(II). The addition of EDTA did not induce any chemical shift variation in the heteronuclear single quantum correlation (HSQC) spectra and did not modify the thermostability profiles of NDM-1 (data not shown). The addition of increasing amounts of Zn(II) to the metal-free NDM-1, followed by thermal shift assay resulted in an increase in the denaturation temperature of the protein (Figure 1 and Supporting Information Table S1), indicating that Zn(II) strongly stabilizes NDM-1. However, at a high concentration of Zn(II), we observed a notable increase in fluorescence background prior to denaturation of NDM-1, suggesting the appearance of an exposed hydrophobic region or the formation of oligomers. This effect occurred at a Zn(II) concentration greater than 2 molar equiv relative to the protein concentration and increased sharply with increasing Zn(II) concentration. It could be explained by intermolecular

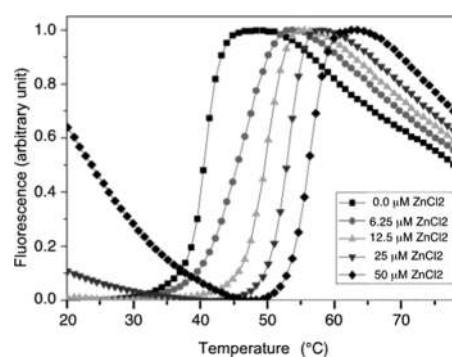


**Figure 1.** Effect of Zn(II) ions on the denaturation of NDM-1 followed by thermal shift assay. Thermal denaturation profiles of NDM-1 were studied in the presence of various concentrations of ZnCl<sub>2</sub> (0–50  $\mu$ M) and 9  $\mu$ M of NDM-1.

interactions between several NDM-1 proteins, mediated by His-tag/Zn(II) complexes.

The effect of Zn(II) binding on the structural and dynamic properties of NDM-1 was investigated by NMR. The <sup>1</sup>H–<sup>15</sup>N HSQC spectra of <sup>15</sup>N-labeled NDM-1, recorded in the absence and presence of 2 molar equiv of Zn(II), showed well-dispersed cross-peaks characteristic of a well-folded protein (Figure 2a).

In the presence of 1 Zn(II) equivalent, we observed a slow exchange, on the NMR chemical shift timescale, between the metal-free and the di-Zn(II) states of NDM-1 (Figure 2b), in agreement with the high affinity of NDM-1 for Zn(II).<sup>23,24</sup> Upon the addition of 2 molar equiv of Zn(II), we only

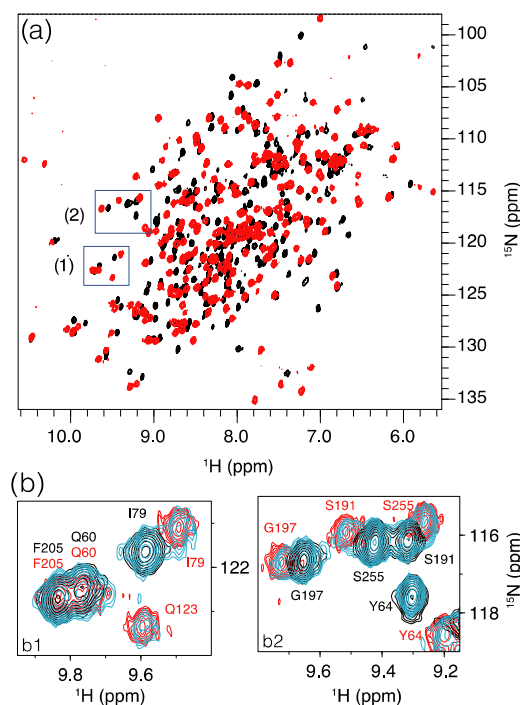


**Figure 2.** (a) Superimposition of the <sup>1</sup>H–<sup>15</sup>N HSQC spectra recorded in the absence of Zn(II) (black) and in the presence of 2 molar equiv of Zn(II) (red). (b) Superimposition of the <sup>1</sup>H–<sup>15</sup>N HSQC spectra recorded on NDM-1 in the absence of Zn(II) (dark blue) and in the presence of 1 (cyan) and 2 molar equiv of Zn(II) (red). Zoomed-in images corresponding to the boxes (1) and (2) highlighted in (a).

observed resonances of the NDM-1 bound state, demonstrating that NDM-1 binds two Zn(II) ions, in accordance with the crystal structures of NDM-1. The  $^1\text{H}$ - $^{15}\text{N}$  HSQC spectrum underwent a drastic change that affected the majority of cross-peaks (Figure 2a), as already mentioned by Zheng et al.<sup>63</sup> Above 2 Zn(II) equivalents, a dramatic decrease of all of the  $^1\text{H}$ - $^{15}\text{N}$  cross-peak intensities was observed (Supporting Information Figure S1) as well as heavy precipitation, suggesting the formation of insoluble NDM-1 oligomers. These NMR data are in agreement with thermal shift experiments (Figure 1), which show that a slight excess of Zn(II) induces NDM-1 oligomerization. Therefore, to limit protein self-association for the rest of this study, we decided to never exceed the 2 molar equiv of Zn(II).

**NMR Backbone Resonance Assignment of NDM-1.** To determine the NDM-1 residues most heavily influenced by Zn(II) binding, we assigned the backbone NMR resonances of NDM-1 alone and complexed with Zn(II), using the classical triple resonance and nuclear Overhauser effect spectroscopy (NOESY) correlation experiments. The optimal quality of the spectra, used for assignment, was observed at 20 °C in the absence of Zn(II) (Supporting Information Figures S2 and S3) and at 27 °C in the presence of 150 mM NaCl and 2 molar equiv of Zn(II) relative to the NDM-1 concentration (Supporting Information Figures S4 and S5). A total of 226 of the 253 metal-free NDM-1 backbone amide protons were assigned. Missing assignments are those of unstructured N-terminus residues (M28-E30) and residues in flexible loops (e.g., V118-D130, Q151-V155, G207, and C208) (Supporting Information Figure S6a). From the di-Zn(II) NDM-1 sample, 94% of the  $^1\text{H}$ - $^{15}\text{N}$  cross-peaks were assigned. Only backbone proton assignments of 14 residues (residues M28-E30, N57, K125, M126, G186, G207, K216, N220, L221, A257, L271, and E272) were missing, probably due to the conformational exchange or fast exchange with the solvent, which resulted in a significant broadening for these amino acids. Many of these residues play an important role in the enzymatic catalysis. Indeed, the residues N220 and L221 are located in the ASL4 loop, which plays a direct role in substrate recognition.<sup>64</sup> Additional 10% backbone resonances have been assigned over the available assignment of NDM-1 in the presence of Zn(II)<sup>65</sup> (Supporting Information Figure S6b).

Substantial differences were observed between the  $^1\text{H}$ - $^{15}\text{N}$  HSQC spectra recorded on metal-free NDM-1 and di-Zn(II) NDM-1 (Supporting Information Figures S2 and S4). Analysis of the  $^{15}\text{N}$ - $^1\text{H}$  chemical shift differences after the addition of increasing concentration of Zn(II) to NDM-1 suggests that the protein undergoes local structural changes upon binding to Zn(II) (Figure 3a). Since the resonances of the ASL2 and L9 loops and of the helix  $\alpha 2$  could not be observed in the absence of Zn(II), no information could be obtained on the chemical shift variations for these three domains in the presence of Zn(II). The largest observable variations are in the ASL3 and ASL5 loops, which include the H189, C208, and H250 residues involved in the coordination of the two Zn(II). It is interesting to note that domains remote from the Zn(II) binding site, such as the  $\beta$ -sheet, which flanks the ASL1 loop and the L5 and L9 loops (Figure 3b), are also affected by the Zn(II) binding. On the contrary, the ASL1 and ASL4 loops show only a minor chemical shift variation upon Zn(II) binding, with the exception of the first residues of the ASL4 loop (residues 206–209), probably due to the coordination of C208 with Zn(II).

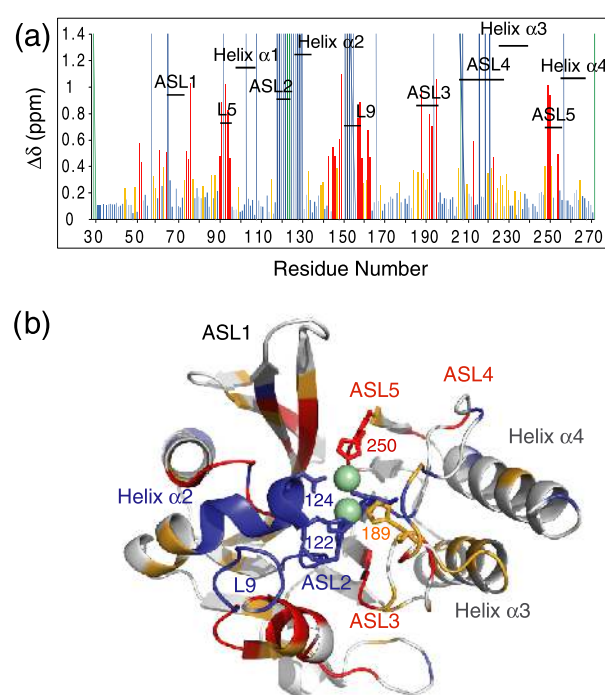


**Figure 3.** Specific interactions between NDM-1 and Zn(II). (a) Chemical shift variations of the nitrogen and amide proton nuclei between metal-free NDM-1 and di-Zn(II) NDM-1. The  $^1\text{H}$  and  $^{15}\text{N}$  chemical shifts were extracted from NDM-1 spectra recorded at 25 °C and 600 MHz  $^1\text{H}$  frequency in the absence of Zn(II), on a sample containing 50 mM phosphate buffer (pH 7.0 and 150 mM NaCl), in the presence of 2 molar equiv of Zn(II) on a solution sample containing 0.1 mM bis tris (pH 7.0, 150 mM NaCl) ( $\Delta\delta$  ( $^1\text{H}$ ,  $^{15}\text{N}$ ) =  $[(\Delta\delta\text{H})^2 + (\Delta\delta\text{N})^2 \times 0.14] \times 0.5$ )<sup>1/2</sup>). In red and orange are indicated the residues with  $\Delta\delta > 0.4$  ppm and  $0.2 > \Delta\delta > 0.4$  ppm, respectively. The unassigned residues of NDM-1 in the absence and presence of Zn(II) are represented by dark blue and green lines, respectively. (b) Location of the residues whose amide proton and nitrogen resonances are significantly disturbed during Zn(II) binding, mapped on the NDM-1 crystal structure (PDB: 3SPU) with the same color code. Zn(II) are represented by green spheres.

The location of the secondary structure elements in the metal-free NDM-1 and di-Zn(II) NDM-1 complex derived from TALOS-N software<sup>66</sup> was in very good agreement with that of the NDM-1 crystal structures in the absence and presence of Zn(II)<sup>13,67</sup> (Supporting Information Figure S6). The results also show that the binding of Zn(II) ions does not significantly modify the NDM-1 secondary structures.

**Analysis of NDM-1 Dynamics by NMR.** To better understand the impact of Zn(II) binding on the dynamics of NDM-1, we collected  $^{15}\text{N}$   $R_1$  and  $R_2$  relaxation rates and  $^1\text{H}$ - $^{15}\text{N}$  heteronuclear NOE (hetNOE) values that provide information on the local and global dynamics in the protein. The results show that the overall structure of NDM-1 is rigid in the presence or absence of Zn(II), with the exception of the N-terminal extremity, which has shorter transversal relaxation rates and lower hetNOE values, indicating greater flexibility in the 100 ps timescale (Supporting Information Figure S7). The  $^{15}\text{N}$  relaxation rates are homogeneous over the folded domains with mean values of  $R_1$  and  $R_2$  of  $0.73 \pm 0.08$  and  $24.22 \pm 1.69$  s<sup>-1</sup>, respectively, in the absence of Zn(II), and  $0.64 \pm 0.05$  and  $31.19 \pm 1.27$  s<sup>-1</sup>, respectively, in the presence of Zn(II) (Supporting Information Table S2). The lower mean value of  $R_1$  and the higher mean value of  $R_2$  calculated in the presence

of Zn(II) could be explained by the NDM-1 intermolecular interactions induced by a slight excess of Zn(II), as already seen in the thermal shift experiments. In addition, the relaxation data show that only the ASL1 loop (residues 65–74) is slightly more flexible than the rigid zones of the protein in both the absence and presence of Zn(II) (for additional information, see Table S2 and Figure S7).

The main effects of the binding of the two Zn(II) occurred at the loops ASL2 and L9, and at  $\alpha$ 2 helix. In the absence of zinc, the residues belonging to these domains showed disappearance of their signals, consistent with an intermediate exchange at the NMR chemical shift timescale, whereas in the presence of zinc, the signals of these residues are perfectly visible and the measured relaxation parameters for these three domains indicate their significant stiffening (Supporting Information Table S2). Indeed, in the absence of Zn(II), the three Zn(II) ligands (H120, H122, and D124) belonging to the ASL2 loop undergo fluctuations that propagate through the ASL2 loop and  $\alpha$ 2 helix. The ASL2 and L9 loops could influence each other due to their spatial proximities in the three-dimensional (3D) structure (Figure 4a). The same

effects of Zn(II) were observed by Chen et al. using molecular dynamics (MD) simulations.<sup>22</sup> In addition, the authors also showed that the di-Zn(II) coordination exerts stronger restrictions on the movements of ASL1 and ASL4 loops (denoted L3 and L10, respectively, in Chen et al.<sup>22</sup>). Our relaxation data did not indicate a decrease in the internal flexibility of ASL1 and ASL4 upon Zn(II) binding contrary to that observed in their MD simulations.<sup>22</sup>

Our results are consistent with crystallographic structures that show that in the absence of zinc, the variabilities in the orientation of ligands that can bind to Zn1 and Zn2 are higher for Zn1 (H120, H122, and H189) than for Zn2 (D124, C208, and H250) (Figure 4a). These observations are validated by comparing the B-factors of several NDM-1 structures crystallized in the absence and presence of Zn(II). B-factors can be used to identify and interpret the dynamic characteristics of proteins.<sup>68</sup> Furthermore, the flexibilities of ASL1 observed by NMR for di-Zn(II) NDM-1 (Figure 4b) are in agreement with that observed by comparison of several X-ray crystal structures of di-Zn(II) NDM-1, which show only significant differences in the orientations of the ASL1 loop (Figure 4b). These observations are also consistent with the results showing that the loop ASL1 is a key loop capable of correctly orienting the substrate in the active site and should therefore, due to its flexibility, be able to adapt to many types of ligands.<sup>13,14,67,69,70</sup>

**Flavonol Molecules Inhibit NDM-1 Activity.** NDM-1 uses two Zn(II) ions and a water molecule coordinated in between in its active site, for the hydrolysis of the antibiotics  $\beta$ -lactam ring.<sup>8</sup> Based on this mechanism, we sought to determine the inhibitory activity of simplified structures, providing an initial structure–activity relationship (SAR) that highlighted a common fragment, which was a phenol, substituted with a keto moiety in the position 2 (Figure 5a). The second ketone substituent may be aromatic, enolic, or aliphatic, the best inhibitory activities being obtained in the first two cases. On the basis of this minimal structure, a chemoinformatic analysis identified 222 molecules of this type available within the LabEx LERMIT chemical library (Figure 5). Biological screening of this library using the miniaturized automated assay allowed us to identify three flavonols (quercetin, myricetin, and morin) as the best inhibitors of NDM-1 (Figure 5b). Overall, the best results have been obtained for myricetin (85% of inhibition at 50  $\mu$ M). The IC<sub>50</sub> for myricetin was determined as 3.3  $\mu$ M (Figure 5c).

Due to solubility problems, IC<sub>50</sub> values for quercetin could only be estimated between 5 and 10  $\mu$ M. To solve this solubility problem, derivatives of quercetin were synthesized (Figure 5d, Supporting Information Figures S8–S10, and Supporting Information Experimental Section on the chemical synthesis of the compounds) that were expected to have improved solubility or bioavailability. Unfortunately, their inhibitory activities were not very different from that observed for quercetin (Figure 5d). Only the mixture of quercetin derivatives with the addition of isopropyl carbonate or methyl isopropyl carbonate to the 3' hydroxy group (MG195c) has a higher inhibitory activity than quercetin and also higher than that observed with myricetin (Figure 5d). On the other hand, oxime formation on the 4-carbonyl group of naringenin (MG219F3) induced a slight decrease in the inhibitory activity of this compound (Figure 5b,d). On the basis of these results, it appears that: the 4-carbonyl group is important for the activities of the molecules; the possible steric gene induced by OMe in position 3', 5, or 3 has little effect on their activities;

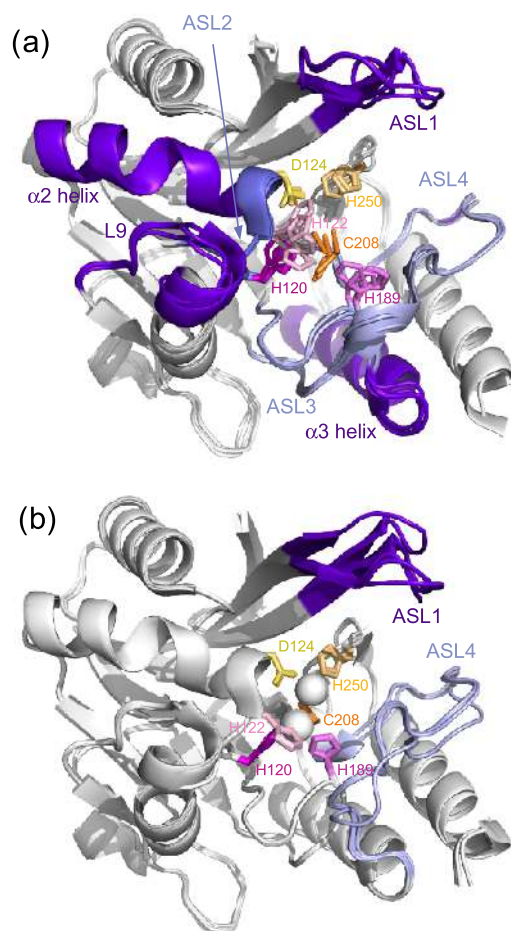


**Figure 4.** (a) Superimposition on the backbone atoms for the domain 45–270 of four metal-free apo-NDM-1 (PDB: 3RKK, 3SBL, 3RKJ, 3PG4) and (b) four apo-NDM-1 (PDB: 3SPU, 4TYF, 4TZE, 4TZF) crystallographic structures. Highly flexible domains, far from the active site, are colored purple, and flexible domains bearing Zn(II) ligands are colored light blue and dark blue. The residues interacting directly with Zn(II) are represented by stick, and the residues interacting with Zn1 and in Zn2 are in pink and orange, respectively. Both Zn(II) are represented by white spheres.

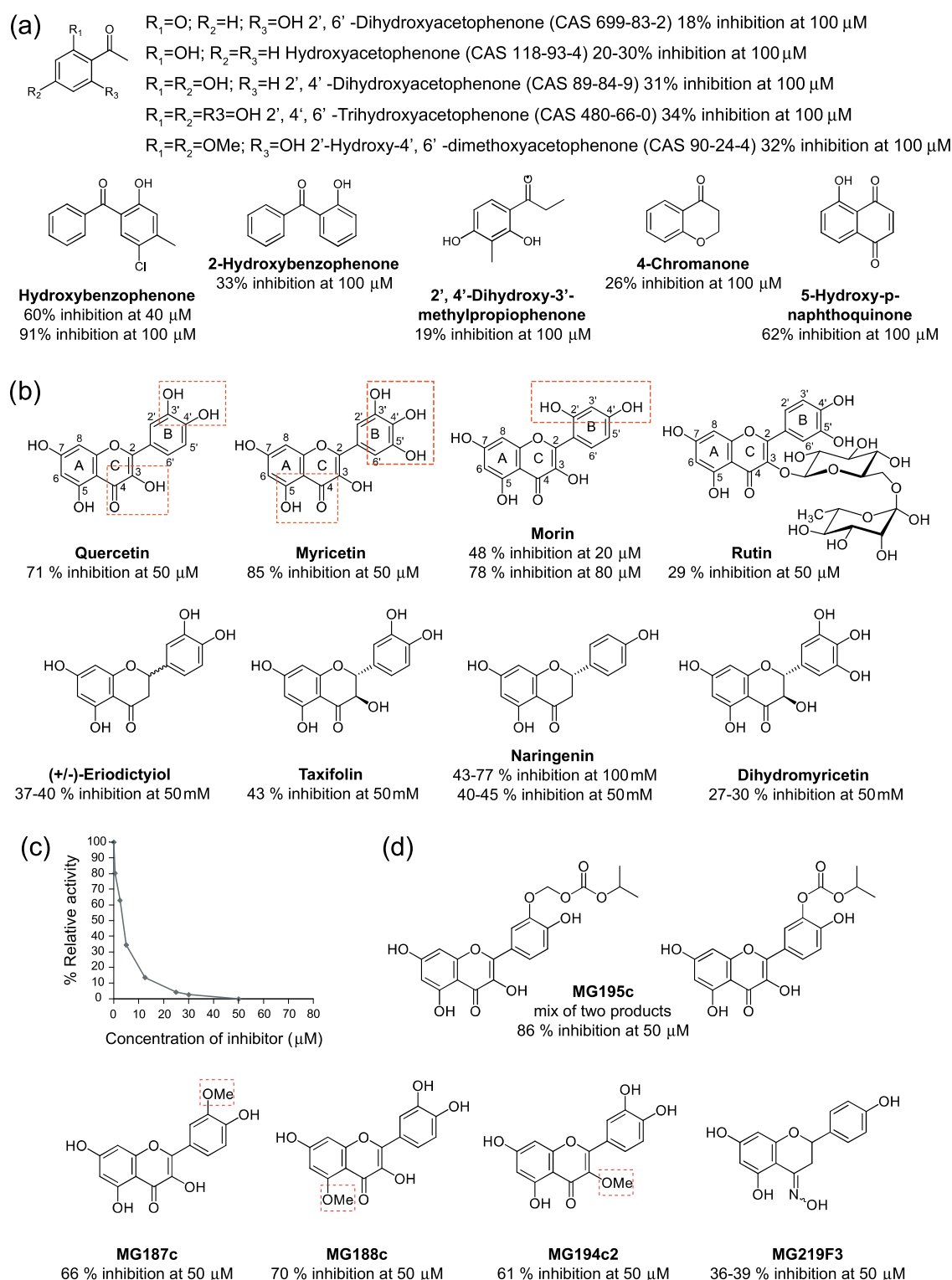


**Figure 5.** (a) Summary of the inhibitory activity of commercially available hydroxyketone derivatives. (b) All of these molecules have the general structure of the flavonoids, a 15-carbon skeleton, which consists of the two phenyl rings A and B and the heterocyclic ring C. Quercetin, myricetin, morin, and rutin differ from each other in the number and position of the hydroxy groups: quercetin, myricetin, and morin. In rutin, the hydroxy group at position C-3 is substituted by glucose and rhamnose sugar groups. The potential chelation sites of Zn(II) are surrounded by red rectangles. Eriodictyol, taxifolin, naringenin, and dihydromyricetin have two stereocenters on the C-ring, unlike the previous ones which have none. They also differ from each other in the number and position of hydroxy groups. (c)  $\text{IC}_{50}$  determination for myricetin on purified NDM-1. Representation of the  $\text{IC}_{50}$  curve for myricetin with the residual activity of NDM-1 monitored by hydrolysis of different concentrations of inhibitor with a constant concentration of imipenem (100  $\mu\text{M}$ ). (d) Quercetin derivatives have been synthesized and tested as inhibitors of NDM-1, with methylation on the 3' (MG187c), 3 (MG194c2), or 5 (MG188c) hydroxy group, oxime formation on the 4-carbonyl group of naringenin (MG219F3), and the addition of isopropyl carbonate or methyl isopropyl carbonate on the 3' hydroxy group (MG195c).

and the addition of polar compounds such as isopropyl carbonate or methyl isopropyl carbonate to hydroxy group 3 increases the activity of the quercetin derivative. None of the quercetin derivatives produced better result than myricetin. Myricetin was also tested at a concentration of 50  $\mu\text{M}$  against other carbapenemases: OXA-48 and KPC-2, with inhibitions of 90 and 78%, respectively.

**In Vivo Activities of Flavonol Molecules on Clinical NDM-1 Producing *Escherichia coli* and *Klebsiella pneumoniae* Isolates.** Minimum inhibitory concentrations (MICs) of imipenem for *K. pneumoniae* CAG and *E. coli* GUE expressing NDM-1 were determined in the presence of increasing amounts of myricetin (Table 1) to assess in vivo

**Table 1. Minimum Inhibitory Concentrations of Imipenem in the Presence of Myricetin and Quercetin for *E. coli* GUE NDM-1 and *K. pneumoniae* CAG NDM-1**

concentration ( $\mu\text{M}$ )	myricetin			quercetin		
	0	50	100	0	100	200
	MICs ( $\mu\text{g/mL}$ )					
<i>E. coli</i> NDM-1 GUE	128	32	8	128	32	16
<i>K. pneumoniae</i> NDM-1 CAG	128	64	16	128	128	128

activity on bacteria. Height-fold drop in MICs was observed with 500  $\mu\text{M}$  myricetin (decreasing from 128 to 16  $\mu\text{g/mL}$ ) for *K. pneumoniae* CAG, and a 16-fold drop in MICs for *E. coli* GUE with 500  $\mu\text{M}$  myricetin (from 128 to 8  $\mu\text{g/mL}$ ), illustrating that these molecules have an in vivo activity. A concentration of 500  $\mu\text{M}$  myricetin has no effect on the growth of the bacteria in the absence of imipenem. The values for quercetin could not be determined accurately, due to solubility problems. Nevertheless, at 100 and 200  $\mu\text{M}$ , two and three dilution drops of MICs were observed with the *E. coli* GUE NDM-1 strain, respectively. No effect was observed with the strain *K. pneumoniae* CAG (Table 1). From our inhibitor activity assay data, we identified the flavonols as candidate inhibitors of the NDM-1 activity. The flavonols are abundant in various fruits and vegetables and are known to interact with proteins involved in cancer, as well as cardiovascular and brain diseases.<sup>54–62,71,72</sup>

**NMR Characterization of the Binding Interface between NDM-1 and the Three Flavonols: Morin, Myricetin, and Quercetin.** The NDM-1/flavonol interactions were investigated by NMR in the presence of Zn(II) (Figure 6). As the ligands (morin, myricetin, and quercetin) were poorly soluble in aqueous solution (these molecules are hydrophobic, and the LogP estimate indicated that myricetin had the best solubility in aqueous buffer (Supporting Information Table S3)), they were introduced into the NDM-1 samples from a concentrated stock of a deuterated dimethyl sulfoxide (DMSO). The addition of small amounts of DMSO did not cause precipitation of the protein or chemical shift variations (Figure 6a). The interaction of NDM-1 with the three flavonols resulted in significant chemical shift perturbations (CSPs) of many backbone amide protons and nitrogens. Representative extracts of  $^1\text{H}$ – $^{15}\text{N}$  HSQC spectra along the titration are shown in Figure 6b, and the  $^1\text{H}$ – $^{15}\text{N}$  chemical shift perturbations after the addition of 2 molar equiv of inhibitors are shown in Figure 7. The analysis highlighted a specific site for interaction of the three flavonols with NDM-1. The NDM-1 residues involved in the interaction with the three flavonols belong mainly to the flexible loops ASL1, ASL2, and

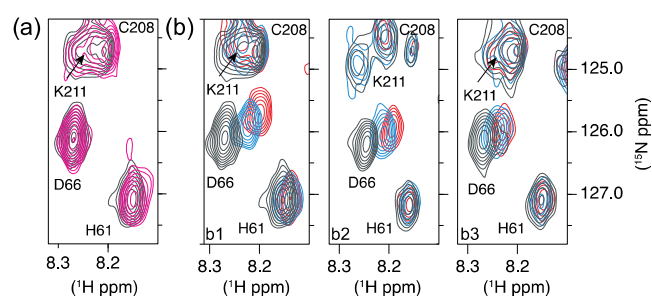


**Figure 6.** Specific interaction between NDM-1 and flavonols. Selected regions of the  $^1\text{H}$ – $^{15}\text{N}$  HSQC spectra probing the NDM-1–flavonol interactions. (a) Addition of DMSO (black in the absence of DMSO and pink in the presence of the amount of DMSO corresponding to that added to have 2 molar equiv of flavonol relative to the concentration of NDM-1: 5.36  $\mu\text{L}$  of DMSO) does not induce significant chemical shift variations of the NDM-1 resonances. (b) Titrations of NDM-1 (black in the absence of flavonol) by 1 molar equiv (in blue) and 2 molar equiv (in red) of morin (b1), quercetin (b2), and myricetin (b3) showing the influence of flavonols on several NDM-1 resonances. The spectra were recorded in the presence of 2 molar equiv of Zn(II).

ASL4, and to a lesser extent to ASL3 and L5 (Figure 7) with subtle differences between the three flavonols. The residues in the ASL1 and ASL4 loops have the highest CSPs in the presence of morin, and W93 and H250 have much higher CSP in the presence of morin (Figure 7a3) than in the presence of quercetin (Figure 7a1) or myricetin (Figure 7a2).

On the contrary, the highest CSPs were observed in the ASL2 loop in the presence of quercetin compared to those observed after the addition of morin. Although specific, the flavonol binding induced CSPs over relatively large regions of the flexible domains such as 62–80, 208–223, and 250–254 (Figure 7a). CSPs were used to estimate the dissociation constant,  $K_d$ , of morin and myricetin despite the uncertainty in the actual concentration of the ligands available in solution due to their precipitation. As the exchange is rapid on the chemical shift timescale, an estimated  $K_d$  value of around 300  $\mu\text{M}$  for the two ligands (Supporting Information Table S4 and Figure S11) could be calculated using the residues with the highest CSPs (L65 and D66). To determine the influence of Zn(II) on flavonol interactions, the CSPs of the NDM-1 backbone resonances were followed using the  $^1\text{H}$ – $^{15}\text{N}$  HSQC spectra recorded at each flavonol increment in the absence of Zn(II) (Figure 7b and Supporting Information Figure S12). As for the flavonol titrations performed in the presence of Zn(II) (Figure 6a), we verified that the addition of DMSO did not induce significant variations in the chemical shift of the NDM-1 resonances in the absence of zinc (Supporting Information Figure S12).

The analysis shows that flavonols also interact with NDM-1, but the CSPs are lower at equal ligand concentration and more dispersed along the protein sequence compared to what happens in the presence of 2 molar equiv of Zn(II). In the absence of Zn(II) and in the presence of 2 (Figure 7b1) and 4 molar equiv (Figure 7b2) of morin, for example, the ASL1 and ASL4 loops are the domains of NDM-1 that undergo the major CSPs. However, in the absence of Zn(II), several other regions are also targeted by the flavonols, including residues 100–111, 135–138, and 156–177, compared to that happened in the presence of Zn(II) (Figure 7a3). It is interesting to note that the two tryptophan residues (W104 and W168) and the many

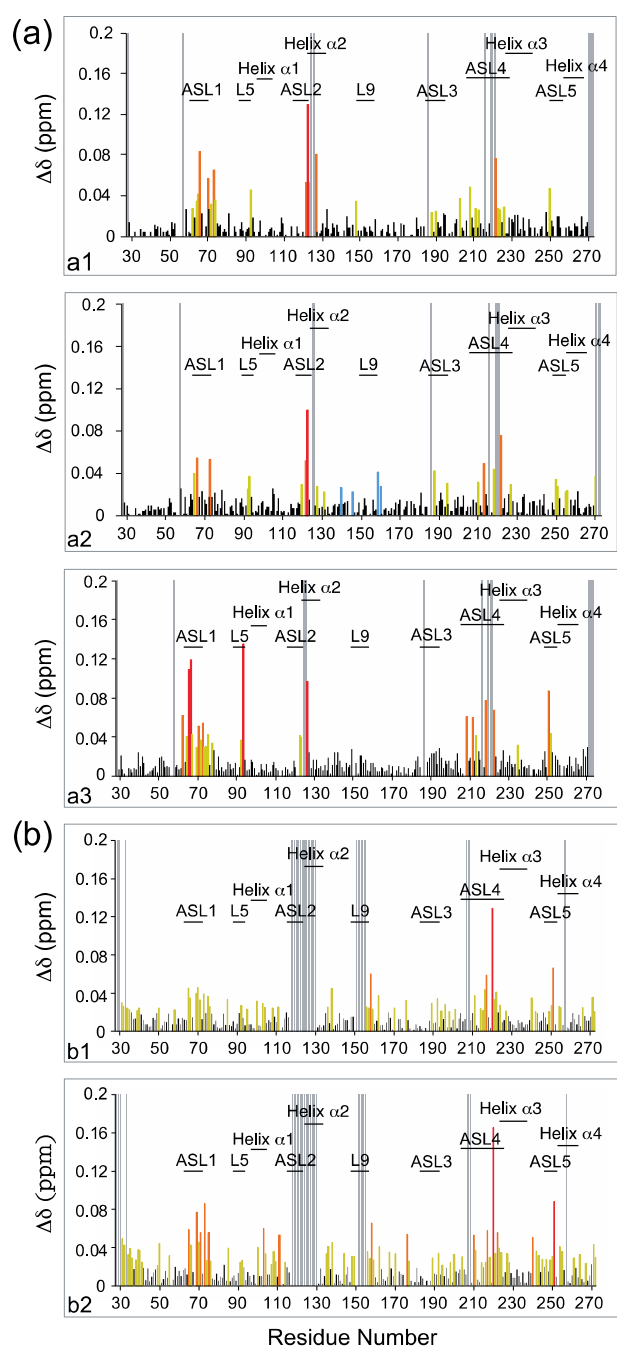


**Figure 7.** (a) Plots of the measured chemical shift perturbations of the amide protons and nitrogens of NDM-1, in the presence of 2 molar equiv of Zn(II), after addition of 2 molar equiv of flavonols: (a1) quercetin, (a2) myricetin, and (a3) morin. (b) Plots of the measured chemical shift perturbations of the amide protons and nitrogens of NDM-1, in the absence of Zn(II) and 2 molar equiv of morin (b1) and 4 molar equiv of morin (b2). In red, orange, and yellow are represented the residues with  $\Delta\delta > 0.09$  ppm,  $0.09 > \Delta\delta > 0.05$  ppm, and  $\Delta\delta > 0.02$  ppm, respectively. The unassigned residues of NDM-1 are represented by gray lines.

localized hydrophobic residues in these domains could interact with the highly hydrophobic flavonols. Thus, the two Zn(II) ions contributed to increase the selectivity of the interaction of NDM-1 for flavonols.

Our results indicate that morin, quercetin, and myricetin interact with NDM-1 residues at the active site, without

ejection of Zn(II). Despite some chemical shift variations upon ligand binding, the  $^1\text{H}$ – $^{15}\text{N}$  HSQC spectra retain their initial appearance, namely, the appearance of the NDM-1 spectrum in the presence of 2 molar equiv of Zn(II), and not the NDM-1 spectrum recorded in the absence of Zn(II). In addition, the hydrophobic residues around the active site L65, F70, and W93 also appear to play an important role in substrate recognition.

Altogether, the residues L65, M67, F70, W93, H122, Q123, D124, N220, and H250 and the two Zn(II) are involved in the binding of flavonols. Our NMR data demonstrated the specific interaction of morin, quercetin, and myricetin at the NDM-1 active site.

These results are in agreement with the previous *in silico* modeling and docking with the generated NDM-1 models, from an alignment with two templates VIM-2 and VIM-4 by Ganugapati et al.<sup>73</sup> and the crystal structure of NDM-1 (PDB: 3SPU) by Padmavathi et al.<sup>74</sup> The results of these two studies indicated that quercetin may be the best inhibitor among the flavonoids present in green tea (flavan-3-ols, flavones, and flavonols) tested during dockings, in terms of energy values for the first study,<sup>73</sup> and calculated binding affinity after docking for the second study.<sup>74</sup>

#### Reconstruction of the NDM-1/Flavonol Binding Interfaces by Molecular Docking Simulations.

As no intermolecular NOE was observed in the  $^{15}\text{N}$ – $^{13}\text{C}$  filtered  $^1\text{H}$ – $^1\text{H}$  NOESYs recorded on  $^{13}\text{C}$ – $^{15}\text{N}$ -labeled NDM-1/flavonol complexes, the structural models of the NDM-1/morin, NDM-1/quercetin, and NDM-1/myricetin complexes were constructed using molecular docking simulations in the NMR data-driven program HADDOCK (High Ambiguity Driven biomolecular DOCKing)<sup>75</sup> on the basis of experimental CSPs. To propose relevant models, several series of calculation were undertaken using 19 crystallographic structures of NDM-1 as the docking results may be influenced by the starting protein structure,<sup>76</sup> whether obtained in the presence or absence of ligand. Ten of them were complexed with a ligand and were used after removal of the complexed ligand, and we called them “artificial” NDM-1 crystal structures (art-apo NDM-1). Five structures were apo NDM-1 crystal structures (crystallized in the absence of ligand), and four were metal-free apo forms of NDM-1 (crystallized in the absence of ligand and in the absence of Zn(II)). The superimposition on the backbone atoms (domain 45–270) of the 10 art-apo NDM-1 structures with each other and with the five apo NDM-1 structures highlights that the main structural differences between all of these structures are located in the loops ASL1 and ASL4 (Supporting Information Figure S13). Furthermore, the distances between the two Zn(II) (Zn1 and Zn2) fluctuate from one structure to the other depending on the presence or absence of a ligand and also of the type of ligand, with the Zn1–Zn2 distances varying from 3.1 to 3.8 Å in the five apo NDM-1 crystal structures, and from 3.6 to 4.6 Å in the 10 art-apo NDM-1 structures used for our docking. In fact, it has been shown by Zhang et al.<sup>77</sup> that Zn1–Zn2 distance in the active site of the native protein is affected by crystal packing, pH, and buffer components. Although the Zn1–Zn2 distances in the enzyme/product complexes are mostly at 4.6 Å,<sup>77</sup> this distance is smaller in several other NDM-1 complexes (Supporting Information Table S5).

Based on our experimental NMR CSP values, the residues L65, M67, F70, W93, H122, Q123, D124, N220, and H250 (Supporting Information Figure S13d,e) were determined to

belong to the interface and used as ambiguous interaction restraints in docking calculation with morin, which induced the largest CSPs (Figure 7) in the NDM-1 spectra. As the NDM-1 CSPs could be the result of direct interactions with flavonol or/and the result of conformation changes of the flexible loops, NDM-1 L65, M67, F70, W93, H122, Q123, D124, N220, and H250 residues were defined as “passive” residues and flavonol as an “active” residue (as defined in the HADDOCK software) in a first step. The best generated models, selected on the basis of the HADDOCK score (Supporting Information Table S6), using the four metal-free apo (Supporting Information Figure S14 and Table S6), the five apo (Supporting Information Figure S15 and Table S6), or the 10 art-apo NDM-1 structures (Supporting Information Figure S16 and Table S6), show that the morin is located in the substrate-binding pocket and is able to contact the Zn(II) ions via polar contacts.

The flavonols are recognized as metal-ion chelators;<sup>78–82</sup> they bind to Zn(II) ions<sup>82</sup> with a lower affinity than NDM-1 does.<sup>23,24</sup> A binding association constant of  $3.57 \pm 0.1 \times 10^4 \text{ M}^{-1}$  was found between quercetin and Zn(II) in protein-free solution by Bhuiya et al.<sup>82</sup> A flavonol molecule has three potential sites for cation chelation: (i) the 3',4' or 2',4'-dihydroxy group or 3',4',5'-trihydroxy group located on the B-ring (depending on the type of flavonol); (ii) between the 3-hydroxy and the 4-carbonyl groups in the C-ring; (iii) and via the 5-hydroxy and the 4-carbonyl group (Figure 5b). In addition, we determined by NMR that the Zn(II) ions direct flavonols binding to the active site of NDM-1 (Figure 7). All of these data showed that both Zn(II) ions probably play a role in the coordination of flavonols at the NDM-1 binding site. Therefore, in the second step of docking simulations, both Zn(II) were defined as active residues in addition to the L65, M67, F70, W93, H122, Q123, D124, N220, H250, and NDM-1 residues defined as passive residues and morin as an active residue using again the five apo (Supporting Information Figure S17 and Table S7) and the 10 art-apo NDM-1 crystallographic structures (Supporting Information Figure S18 and Table S7).

Analysis of the four best structures of each top clusters shows that, as expected, the morin targets the Zn(II) ions through polar contacts. The orientation of the morin in the active site of NDM-1 was strongly dependent on the crystallographic structure used for docking (Supporting Information Figures S17–S18). Either the morin adopts only a single orientation in the NDM-1 active site for the four structures in each top cluster or the orientations are very different from each other. In the first case, the rmsd values calculated on the morin atoms after superimposition on the (45–271) backbone atoms of the NDM-1 structures (art-apo PDB: 4EY2, 4EYB, 4HL2, 4RL0, 4EYF) are between 0.68 and 1.43 Å, and in the second case, (art-apo PDB: 4EXS, 4EYL, 4RAM, 4RBS, 4RL2) between 2.58 and 5.40 Å (Supporting Information Table S8). It is interesting to note that this difference in behavior seems to be related to the Zn1–Zn2 distances in the starting structures of NDM-1 used for the docking since they vary from 4.5 to 4.6 Å in the first case and from 3.1 to 4.1 Å in the second case (Supporting Information Table S5) and also to the orientation of the ASL1 loop toward the active site (Supporting Information Figure S13c). A 62.5% of the structures analyzed adopt orientation 1 (Figure 8a,c) with an average rmsd of  $0.91 \pm 0.32 \text{ Å}$  for 52.5% of them and  $3.24 \pm 0.59 \text{ Å}$  for the remaining. A 17.5% of the structures are in orientation 2 (Figure 8b,d) with a main rmsd value of 3.35

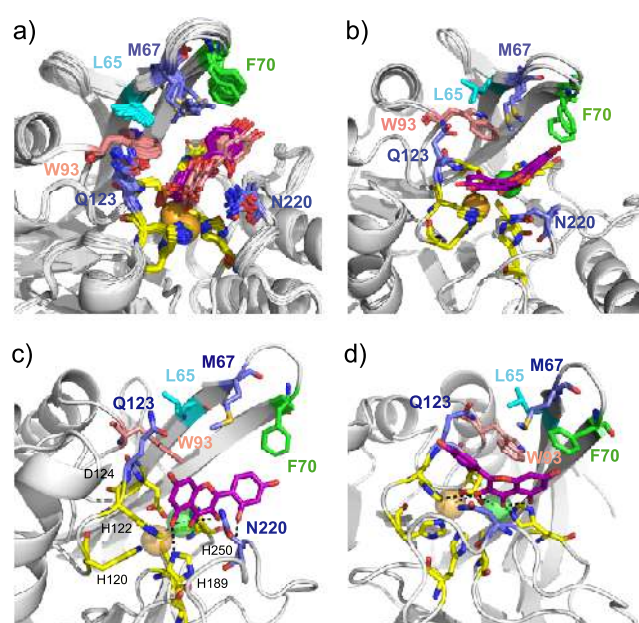


**Figure 8.** Models of the NDM-1/morin complexes generated using HADDOCK. (a) Superimposition of 21 structures over the 40 structures clustered in the top clusters, generated using the 10 art-apo NDM-1 crystallographic structures (PDB: 4EXS, 4EY2, 4EYB, 4EYF, 4EYL, 4HL2, 4RAM, 4RBS, 4RL2, 4RL0) showing the predominant orientation of morin at the active site of NDM-1 (orientation 1). These 21 structures adopt two slightly different orientations in the active site, 11 are in dark pink, and 10 in light pink. (b). A minority orientation is also observed in the docking generated structures (orientation 2). Orientation 2 differs from orientation 1 by a rotation of about 180°. (c) Zoom on one of the 21 structures in which morin adopts orientation 1 showing the polar contacts between the ligand and Zn(II) ions (PDB: 4HL2) (cluster 1: structure 2). (d) Zoom on one of the structures in which morin adopts orientation 2 showing the polar contacts between the ligand and Zn(II) ions (PDB: 4RBS (cluster 1: structure 1)). The Zn(II) ligands are represented by stick and colored yellow, Zn1 is orange, and Zn2 is green and represented by spheres. L65, M67, F70, W93, Q123, and N220, defined as active residues (in addition to H122, D124, and H250 in yellow) upon docking are represented by stick and colored differently for better identification.

$\pm 1.09 \text{ Å}$  between them. We observed a loss of Zn2 coordination in the remaining structures (20%), so we did not associate them to any group. It is interesting to note that the loss of Zn2 coordination is only observed for the NDM-1 starting structures with the shortest Zn1–Zn2 distances. More precisely, the Zn1–Zn2 distance is the factor that most strongly affected the positioning of the ligand in the active site during molecular docking simulations. As already described by Zhang et al.,<sup>77</sup> although the Zn1–Zn2 distances observed in different structures of NDM-1 complexed with hydrolyzed antibiotics are longer than those observed for NDM-1 in the native form, they fluctuate after all between 3.8 and 4.6 Å and are also highly dependent on the type of ligand. Therefore, the choice of NDM-1 starting structures for docking with ligands capable of binding Zn(II) strongly influences the final results. Our docking results show that the PDB crystal structures 4EY2, 4EYB, 4HL2, and 4EYF are the most suitable for docking calculations with the morin structure. Indeed, the smallest deviations of Zn1 and Zn2 after docking from their positions in the original crystal structures were observed with these four crystal structures (Supporting Information Figure

S19). These structures have the largest distances between Zn1 and Zn2, 4.6 Å (Supporting Information Table S5). In addition, the rmsd values calculated on the morin atoms are also the lowest (Supporting Information Figure S18 and Table S8).

In orientation 1 and orientation 2, electrostatic interactions are observed between Zn2 and O-3 (cycle C), O-4 (cycle C), and O-5 (cycle A). Zn1 is either targeted by 5-O (cycle A) in orientation 1 or by O-3 (cycle C) in orientation 2 (Figure 8c,d). In addition, hydrogen-bond interactions are also observed between O-7 (cycle A) and the amide proton of Q123 and between O-2' (cycle B) and the amide proton of N220 in orientation 1 in several complexes (Figure 8c). Morin also showed a H-bonding with H189 in orientation 1 (Figure 8c). In addition, the three-ring system forms extensive nonpolar interactions with L65, M67, F70, and W93 (Figure 8). Moreover, the CSPs observed for several Zn(II) ligands such as H122, D124, and H250, and to a lesser extent C208, could be explained by a slight movement of Zn1 and Zn2 and their ligands during the interaction between NDM-1 and flavonols, as well as a direct interaction with flavonols (Figure 8).

To investigate whether the number and position of hydroxy groups on the B-ring could influence the orientations of flavonol in the active site of NDM-1, docking simulations were also undertaken using quercetin (Supporting Information Table S9) and myricetin (Supporting Information Table S10) using the protocol already described in the previous paragraph. The molecular docking results show that morin, quercetin, and myricetin are located in the same binding site (Supporting Information Figure S20). The variability of ligand orientations in the active site of NDM-1 is greater for quercetin and myricetin than for morin and the number of structures rejected (usually due to loss of Zn2 coordination (Supporting Information Figure S18)) is also greater for quercetin and myricetin than for morin. Quercetin and myricetin also predominantly adopt orientation 1. In orientation 1 and orientation 2, the Zn(II) ions/morin, Zn(II) ions/quercetin, and Zn(II) ions/myricetin interactions are quite similar regardless of flavonol.

It is interesting to note that the addition of methoxy groups at the 3', 5, or 3 positions slightly decrease the inhibition of native quercetin (Figure 5d). We verified using molecular docking simulation that the three quercetin derivatives are still able to interact with Zn(II) (Supporting Information Figure S21) with approximately the same structural statistics (Table S11) as quercetin wild type. As for quercetin, orientation 1 is mainly adopted by quercetin derivatives. In all cases, their C4 carbonyl group interacts with Zn2 in the active site of NDM-1. Moreover, despite the possible steric hindrance generated by the replacement of the hydroxyl group by a methoxy at positions 3 (MG194c2) or 5 (MG188c) (Figure 5d), the structures resulting from docking show that these two quercetin derivatives are still capable of complexing Zn1 by their 5-O (cycle A). This is also true for the derivative in which the hydroxyl group has been replaced by a methoxy at the 3' position (MG187c). The slight decreases in inhibition are explained by the steric hindrance generated by the methoxy groups.

There are very few flavonol structures that interact with metal ions within a protein. Interestingly, quercetin has been shown to have strong inhibitory activities against yeast alcohol dehydrogenase, which has been explained on the basis of the

formation of a complex between quercetin and the Zn(II) ion that maintains the tertiary structure of the metallo-enzyme.<sup>7,82</sup>

In addition, the crystal structures of quercetin 2,3-dioxygenase, a mononuclear copper-dependent dioxygenase (PDB: 1H1I, 1H1M),<sup>83</sup> and quercetin 2,4-dioxygenases, which uses nickel as an active site cofactor to catalyze oxidative cleavage, complexed with the quercetin substrate (PDB: 5FLI),<sup>84</sup> show that the coordination of the metal ions involved in both cases, the 3-hydroxy and the 4-carbonyl groups in the C-ring of quercetin with distances around 2.3 and 3.5 Å, respectively. We also observed in orientation 1 and orientation 2 of our NDM-1/flavonol models the electrostatic interactions between Zn2 and the 3-hydroxy and the 4-carbonyl groups of quercetin.

NDM-1 hydrolyzed antibiotics such as methicillin (PDB: 4EY2), oxacillin (PDB: 4EYB), meropenems (PDB: 4RBS, 4EYL), benzylpenicillin (PDB: 4EYF), cephalosporins (PDB: 4RL2, 4RL0), penicillin G (PDB: 4RAM), and ampicillin (PDB: 4HL2) bind the two Zn(II) through polar interaction with the carbapenem C3 and C6 carboxylate oxygens (Supporting Information Figure S22). Most of MBL inhibitors belong to one of two categories: either they act by sequestration of Zn(II), such as EDTA<sup>17,47,85,86</sup> and aspergillomarasmine A,<sup>87</sup> resulting in inactivation of the enzyme, or they have several electron donor groups, such as carboxylate, carboxyl, thiol, and/or nitrogen, which are capable of binding one or both Zn(II) in the active site<sup>17,27–31,35–44,50,88–91</sup> to act as competitive inhibitors. We show that flavonols belong here to the second category and that they are able to bind to both Zn(II) in the active site of NDM-1, without expelling the Zn(II) ions from the protein.

## CONCLUSIONS

Our analysis of NDM-1 by NMR in the absence and presence of Zn(II) shows that specific regions (ASL2, ASL3, ASL5, and L9 loops and Helix  $\alpha 2$ ) of the protein were affected by the binding of two Zn(II). Ion binding led to the rigidification of the protein with respect to the metal-free NDM-1, but the ASL1 loop retained its slight flexibility even after Zn(II) binding. Our assay of inhibitor activities and structural characterization of NDM-1/flavonols complexes in the presence of Zn(II) show that morin, myricetin, and quercetin interact in the same binding site as antibiotics and that these interactions are largely driven by the interaction with both Zn(II) as is the case for substrate recognition in MBLs, which is largely determined by the interaction with metal ions.<sup>92,93</sup>

## EXPERIMENTAL SECTION

**Protein Production and Purification.** The gene sequence encoding the NDM-1 mature enzyme from G29 to R270 was subcloned into a pET41b vector with a C-terminal His6 tag to facilitate protein purification. For the overexpression of the double <sup>15</sup>N/<sup>13</sup>C-labeled NDM-1 sample, the fusion protein was expressed in BL21 *E. coli* cells. A 100 mL Lysogeny broth (LB) culture supplemented with 40  $\mu$ g/mL kanamycin was inoculated with 10 mL of a fresh overnight LB preculture and grown at 37 °C until OD<sub>600</sub> = 1.5. After a 10 min centrifugation at 5000 rpm, the bacterial pellet was resuspended in 1 L of M9 minimal medium (Na<sub>2</sub>HPO<sub>4</sub>, 6 g/L; KH<sub>2</sub>PO<sub>4</sub>, 3 g/L; NaCl, 0.5 g/L; MgSO<sub>4</sub>, 1 mM; CaCl<sub>2</sub>, 1.10<sup>-4</sup> M) containing 2.0 g/L [<sup>13</sup>C]glucose, 1 g/L [<sup>15</sup>N]NH<sub>4</sub>Cl, and 40  $\mu$ g/mL kanamycin preincubated at 37 °C. The culture was maintained in this medium at 37 °C until OD<sub>600</sub> ~ 0.6.

Subsequently, induction with 0.4 mM isopropyl- $\beta$ -D-thiogalactopyranoside took place for 20 h at 28 °C.

The bacteria were spun down at 5000 rpm for 10 min, and the pellet (3.5 g) was washed in phosphate-buffered saline (PBS); sonicated 15 times with 10 s pulses at 4 °C in 30 mL of buffer A (20 mM sodium phosphate pH 7.5, 0.5 M NaCl, 10 mM imidazole, 1 mM  $\beta$ -ME) containing 0.5 mg/mL lysosyme, 100  $\mu$ g/mL DNase, and one tablet of complete mini EDTA-free protease inhibitor cocktail (Roche Diagnostics); and centrifuged (100 000g for 30 min). The supernatant was applied two times on a 1 mL His GraviTrap affinity column (GE Healthcare) equilibrated with buffer A, and the column was washed with 20 mL of buffer A containing 20 mM imidazole. Then, elution of the protein was carried out in buffer A containing 0.3 M imidazole. The eluted fraction containing pure NDM-1 (about 50 mg) was brought to a concentration of 500  $\mu$ M by ultrafiltration and dialysis against 0.1 M Bis-Tris-HCl pH 7.0.

**Thermal Shift Assay.** The thermal shift assay was performed using the ABI7900HT Real-Time PCR system (Applied Biosystems). The assay quantifies the binding of the Sypro Orange probe to exposed hydrophobic regions of proteins challenged to a temperature gradient.<sup>94</sup> The dye becomes highly fluorescent when bound to protein hydrophobic sites. NDM-1 samples (9  $\mu$ M) were incubated in buffer 100 mM Bis-Tris pH 7 containing different ZnCl<sub>2</sub> concentrations and Sypro Orange (650-fold diluted from stock solution; Invitrogen). Reactions were carried out in duplicate in a 96-well fast PCR plate at a final volume of 20  $\mu$ L. The samples were submitted to denaturation from 15 to 95 °C at a rate of 3 °C/min, and fluorescence of Sypro Orange dye was recorded in real time (excitation spectra, 488 nm; emission spectra, 500–650 nm). The protein denaturation temperature was calculated using the software SDS2.4.1 as the maximum of the derivative of the resulting fluorescence curves.

**Enzyme Activity Assay Screening Library.** All of the compounds tested as potential inhibitors of NDM-1 were either purchased from Sigma-Aldrich Corporation or available from LabEx LERMIT. The CAS numbers are as follows: hydroxybenzophenone (CAS 68751-90-6), 2-hydroxybenzophenone (CAS 117-99-7), 2',4'-dihydroxy-3'-methylpropionophenone (CAS 63876-46-0), 5-hydroxy-*p*-naphthoquinone (CAS 481-39-0), 4-chromanone (CAS 491-37-2), quercetin (CAS 117-39-5), myricetin (CAS 529-44-2) and morin (CAS 654055-01-3), rutin (CAS 207671-50-9), eriodictyol (CAS 4049-38-1), taxifolin (CAS 480-18-2), naringenin (CAS 67604-48-2), and dihydromyricetin (CAS 27200-12-0). They were dissolved in 100% DMSO as 5 or 10 mM stock solutions. The imipenem antibiotic was purchased from Ranbaxy and dissolved in Milli-Q water as a 10 mM stock solution. To determine the percentage of inhibition, a miniaturized automated assay was set up based on a 96-well plate format with a concentration of 0.5  $\mu$ g/mL NDM-1. The screening assay conditions were as follows: 100 mM phosphate buffer, pH 7.0 (Na<sub>2</sub>HPO<sub>4</sub>/NaH<sub>2</sub>PO<sub>4</sub>) added with 50  $\mu$ M ZnSO<sub>4</sub>; 100  $\mu$ M imipenem, and 50  $\mu$ M of compound (dissolved in DMSO) monitored by a Varian Cary 300 Bio UV–Visible spectrophotometer at 297 nm; time course, 600 s; 25 °C. Imipenem was added into the reaction after 5 min of incubation. In parallel, two controls were performed: positive control was performed with DMSO instead of compound and the negative control with 1 mM EDTA. The equation for the calculation of the percentage of inhibition is: Percentage inhibition =  $(1 - (I_0 -$

$I_{\text{EDTA}})/(I_{\text{DMSO}} - I_{\text{EDTA}})) \times 100\%$ , where  $I_0$  is the intensity of the product signal in each well,  $I_{\text{EDTA}}$  is the intensity in the presence of EDTA, and  $I_{\text{DMSO}}$  is the intensity in the presence of DMSO.

**IC<sub>50</sub> Determination.** IC<sub>50</sub> of the inhibitors was determined in 100 mM phosphate buffer, pH 7.0 (Na<sub>2</sub>HPO<sub>4</sub>/NaH<sub>2</sub>PO<sub>4</sub>), added with 50  $\mu$ M ZnSO<sub>4</sub> and 100  $\mu$ M imipenem, and the mixture was incubated for 3 min. The assay was performed with an ULTROSPEC 2000 UV spectrophotometer and SWIFT II software (GE Healthcare, Velizy-Villacoublay, France). IC<sub>50</sub> values were obtained using the equation  $\text{IC}_{50} = ((1/0.5 \times v_0) - m)/q$ , where  $v_0$  is the rate of hydrolysis of the reporter substrate ( $v_0$  being the rate measured in the absence of inhibitor),  $q$  is the  $y$  axis intercept, and  $m$  is the slope of the resulting linear regression.

**Minimum Inhibitory Concentration (MIC) Determination.** MIC values were determined by broth microdilution, in triplicate, in cation-adjusted Mueller Hinton broth according to the Clinical Laboratory Standards Institute (CLSI) guidelines. Two enterobacterial clinical strains expressing the carbapenemase NDM-1 were used: *E. coli* NDM-1 GUE and *K. pneumoniae* NDM-1 CAG. Experiments were performed in microtiter plates containing the medium with imipenem and inhibitors (myricetin and quercetin) dissolved (DMSO) at different concentrations (0.5, 5, 50, 500, and 1000  $\mu$ M). Plates were incubated overnight at 37 °C for 18–24 h.

**NMR Backbone Resonance Assignment.** Samples for NMR spectroscopy are composed either of 0.1 M Bis-Tris-HCl pH 7.0 buffer, supplemented by 150 mM NaCl or 50 mM phosphate sodium pH 6.5 depending, respectively, on the presence or absence of ZnCl<sub>2</sub> in the solutions, and 95%/5% H<sub>2</sub>O/D<sub>2</sub>O. Protein concentration was set from 100 to 996  $\mu$ M. The NMR spectra were recorded on 600 and 800 MHz Bruker Avance III spectrometers at different temperatures ranging from 20 to 35 °C depending on the presence or absence of ZnCl<sub>2</sub>. The two spectrometers are equipped with a 5 mm z-gradient TCI (H/C/N) cryoprobe.

The backbone resonance assignments were performed in the absence or presence of ZnCl<sub>2</sub> using the standard triple resonance experiments: HNCA, HN(CO)CA, HNCO, HN(CA)CO, HNCACB, and HN(CO)CACB. 3D NOESY-<sup>15</sup>N edited spectra (mixing times 100 and 200 ms) were also collected to help the assignment. NMR data were processed using TOPSPIN 3.5 software (Bruker) and analyzed using CcpNmr 2.4.2 software (<http://www.ccpn.ac.uk>).<sup>95</sup> NDM-1 resonance assignments in the absence and presence of 2 molar equiv of Zn(II) were deposited in BMRB accession numbers 26950 and 26952, respectively.

**<sup>15</sup>N Relaxation Measurements.** The <sup>15</sup>N  $R_1$  and  $R_2$  relaxation rates and  $\{^1\text{H}\}-^{15}\text{N}$  heteronuclear NOE were measured at 25 °C and 600 MHz <sup>1</sup>H frequency on the metal-free NDM-1 and di-Zn(II) NDM-1 complex. The experiments were based on the TROSY-based relaxation experiments<sup>96</sup> and recorded in an interleaved pseudo-3D method. For the determination of  $R_1$  relaxation constants, 13 total data sets were collected at relaxation delay times of 20 (duplicated), 100, 200, 300, 500, 600, 750, 900, 1000, 1200, 1400, and 1700 ms. For the determination of  $R_2$  relaxation constants, 13 data sets were collected at delay times of 16.96 (duplicated), 33.92, 50.88, 67.84, 101.76, 118.72, 152.64, 169.60, 203.52, 237.44, 271.36, and 305.28 ms.

Two two-dimensional (2D) <sup>1</sup>H–<sup>15</sup>N planes were collected in the presence or absence of a 3 s <sup>1</sup>H saturation sequence

(120° <sup>1</sup>H pulses train) during relaxation delay to extract the {<sup>1</sup>H}–<sup>15</sup>N heteronuclear NOE. Spectral widths were 1.630 and 4.208 kHz along the <sup>15</sup>N and <sup>1</sup>H dimensions, respectively, and the interscan delay was set to 5 s. The acquisition times were 121.65 and 41.5 ms in the <sup>1</sup>H and <sup>15</sup>N dimensions, respectively, with 16 scans per increment for the determination of *R*<sub>1</sub> and *R*<sub>2</sub> relaxation constants. The duration of the experiments was around 2 days each. For {<sup>1</sup>H}–<sup>15</sup>N heteronuclear NOE experiments, the acquisition times were 121.65 and 62.3 ms in the <sup>1</sup>H and <sup>15</sup>N dimensions, respectively, with 32 scans per increment and a duration of experience of 14 h.

**NMR HSQC Titration Experiments.** The NDM-1–Zn(II) interaction was characterized by means of chemical shift perturbations (CSPs), using a series of <sup>1</sup>H–<sup>15</sup>N HSQC experiments recorded upon the addition of increasing concentration of ZnCl<sub>2</sub>. The protein, concentrated to 320 μM, was solubilized in 0.1 mM Bis-Tris solution, pH 7, supplemented by 150 mM NaCl. ZnCl<sub>2</sub> was dissolved in 0.1 mM Bis-tris buffer, pH 7, to a concentration of 20 mM in the stock solution.

The flavonols (morin, quercetin, and myricetin) interaction surfaces on NDM-1 were characterized in the presence of 2 molar equiv of Zn(II). The flavonols were dissolved in 100% DMSO at a concentration of 20 mM. We titrated 320 μM of NDM-1 with the flavonols (0–4 molar equiv for morin, 0–3 molar equiv for myricetin, and 0–2 molar equiv for quercetin). Approximately 2.7 μL of DMSO was added by an equivalent of flavonol (the final concentration of DMSO-*d*<sub>6</sub> did not exceed 5% in the NMR tube), and at each stage of the titration, one-dimensional (1D) <sup>1</sup>H and 2D <sup>1</sup>H–<sup>15</sup>N HSQC spectra were recorded. In all cases, we observed a slight precipitation of the ligands probably due to their hydrophobic properties. Each HSQC spectrum was collected with eight scans per increment with spectral widths of 9.6 and 3.2 kHz for <sup>1</sup>H and <sup>15</sup>N, respectively, as well as 256 data points in the indirect dimension. The experiments used the 3-9-19 watergate sequence<sup>97</sup> for water suppression. The weighted chemical shift change of each NH signal was calculated according to:

$\Delta\delta (^1\text{H}, ^{15}\text{N}) = [((\Delta\delta_{\text{H}})^2 + (\Delta\delta_{\text{N}})^2 \times 0.14) \times 0.5]^{1/2}$ , where  $\delta_{\text{H}}$  and  $\delta_{\text{N}}$  are the modifications of the chemical shift in the <sup>1</sup>H and <sup>15</sup>N dimensions, respectively.<sup>98</sup>

**NDM-1/Flavonol Dockings Using HADDOCK.** Ambiguous distance restraints based on chemical shift perturbations were used to drive the docking between NDM-1 and the three flavonols: morin, quercetin, and myricetin. Nineteen crystallographic structures of NDM-1 were used: (i) 10 of them were in complex with a ligand: hydrolyzed methicillin (PDB: 4EY2), hydrolyzed oxacillin (PDB: 4EYB), L-captopril (PDB: 4EXS); hydrolyzed meropenems (PDB: 4EYL, 4RBS); hydrolyzed benzylpenicillin (PDB: 4EYF); hydrolyzed cephalosporins (PDB: 4RL0, 4RL2), hydrolyzed penicillin G (PDB: 4RAM), hydrolyzed ampicillin (PDB: 4HL2), these structures were used after removing of the ligand localized in the active site of the NDM-1 crystallographic structures, and named “artificial apo” (art-apo) NDM-1 structures; (ii) five of them were apo NDM-1 crystal structures (PDB: 4TYF, 3S0Z, 4TZF, 4TZE, 3SPU); (iii) four were metal-free apo form of NDM-1 (PDB: 3RKJ, 3RKK, 3SBL, 3PG4). The three flavonol structures were extracted from crystal structures: morin PDB: 6AE3, 5AUJ; quercetin PDB: 2UXH; myricetin PDB: 2O63 where they were in complex with proteins. The L65, M67, F70, W93, H122, Q123, D124, N220, and H250 residues were defined as

belonging to the NDM-1 interaction surface with the flavonols. In a first series of calculations, the two Zn(II) were defined as passive residues and in a second series as active residues. In addition, a restraint file (unambiguous restraints) that imposed the distances between Zn1 and Zn2, on the one hand, and between Zn1 and Zn2, and their respective ligands His120, His122, His189 and Asp124, Cys208, His250, was supplied to HADDOCK<sup>75</sup> to maintain the geometry around each Zn(II). For the two series of calculations, L65, M67, F70, W93, Q123, N220, D124, and H250 were defined as passive residues. In all of the steps, the residues belonging to the segments 65, 92–94, 123, and 218–222 were defined as fully flexible segments, and those belonging to 66–73 as semiflexible segments. During the rigid-body docking, 2000 structures were calculated, and 400 or 200 (depending on the calculation) during both simulated annealing and water refinement. All 400 or 200 water-refined structures were analyzed, and the cutoff for clustering was 7.5, or 0.6 Å for interface RMSD or Fraction of Common Contacts (FCC) respectively, with four structures per cluster. The ranking of the clusters is based on the average score of the top four members of each cluster. The HADDOCK score is calculated as a function of the intermolecular van der Waals energy, intermolecular electrostatic energy, empirical desolvation energy term, and ambiguous interaction restraints (AIRs) energy. The cluster numbering reflects the size of the cluster, with cluster 1 being the most populated cluster. After successful docking, the best complex models were selected on the basis of the HADDOCK score (Tables S6, S7, S9, and S10). The same protocol was used for the docking of NDM-1 (PDB: 4EY2) and three quercetin conjugates: quercetin-CH3A (quercetin with OMe in position 5); quercetin-CH3B (quercetin with OMe in position 3'); and quercetin-CH3C (quercetin with OMe in position 3) (Table S11).

## ■ ASSOCIATED CONTENT

### Supporting Information

The Supporting Information is available free of charge at <https://pubs.acs.org/doi/10.1021/acsomega.0c00590>.

Influence of zinc on the NDM-1 <sup>1</sup>H–<sup>15</sup>N HSQC spectra (Figures S1–S5); comparison of the NDM-1 secondary structures derived from NMR chemical shifts by TALOS + with those observed in the X-ray structures and the Yao et al. results (Figure S6); schemes of the synthetic route of compounds MG188c, MG187c, MG195c, MG194c2, and MG219F3 (Figures S7–S9); experimental NMR titration curves (Figure S10); selected regions of the <sup>1</sup>H–<sup>15</sup>N HSQC recorded in the absence of Zn(II) and in the presence of morin (Figure S11); superimposition of the 10 art-apo NDM-1 and apo-NDM-1 crystallographic structures (Figure S12); models of the NDM-1/morin complexes generated using the HADDOCK webserver using the conditions described in the Experimental Section (Figures S13–S17); relative deviations of Zn1 and Zn2 during docking (Figure S18); models of the NDM-1/quercetin and NDM-1/myricetin complexes (Figure S19); models of the NDM-1/quercetin conjugate complexes (Figure S20); comparison of the NDM-1/morin model structure and the PDB structures of NDM-1 in complex with hydrolyzed antibiotics (Figure S21); effect of Zn(II) on NDM-1 thermal stability (Table S1); average of the relaxation parameters of the flexible and rigid domains of NDM-1

(Table S2); log *P* of the flavonols (Table S3); estimated  $K_d$  values of morin and myricetin in complex with NDM-1 (Table S4); Zn1–Zn2 distances in PDB structures of NDM-1 (Table S5); NDM-1/morin docking results using HADDOCK (Tables S6 and S7); Rmsd calculated on the morin atoms in complex with NDM-1 (Table S8); NDM-1/quercetin docking results using HADDOCK (Table S9); NDM-1/myricetin docking results using HADDOCK (Table S10); NDM-1/quercetin derivatives docking results using HADDOCK (Table S11); Experimental Section: chemical synthesis of the compounds: MG188c, MG187c, MG195c, MG194c2, and MG219F3 (PDF)

### Accession Codes

Atomic coordinates of the HADDOCK models of NDM-1/morin, NDM-1/quercetin, and NDM-1/myricetin have been deposited to the PDB under accession code PDB ID: 6TT8, 6TTA, and 6TTC, respectively. NDM-1 resonance assignments in the absence and presence of 2 molar equiv of Zn(II) were deposited in BMRB accession numbers 26950 and 26952, respectively.

## AUTHOR INFORMATION

### Corresponding Authors

**Thierry Naas** – EA7361 “Structure, Dynamic, Function and Expression of Broad Spectrum  $\beta$ -Lactamases”, Faculty of Medicine, Université Paris-Sud, Université Paris-Saclay, Le Kremlin-Bicêtre, France; Phone: (33)145212019 or (33)145213030; Email: [thierry.naas@aphp.fr](mailto:thierry.naas@aphp.fr); Fax: (33)145216340

**Nelly Morellet** – Institut de Chimie des Substances Naturelles, CNRS UPR 2301, Université Paris-Sud, Université Paris-Saclay, 91190 Gif-sur-Yvette, France; [orcid.org/0000-0001-5076-8884](https://orcid.org/0000-0001-5076-8884); Phone: (33)169823762; Email: [nelly.morellet@cnrs.fr](mailto:nelly.morellet@cnrs.fr); Fax: (33)169823784

### Authors

**Gwladys Rivière** – Institut de Chimie des Substances Naturelles, CNRS UPR 2301, Université Paris-Sud, Université Paris-Saclay, 91190 Gif-sur-Yvette, France

**Saoussen Oueslati** – EA7361 “Structure, Dynamic, Function and Expression of Broad Spectrum  $\beta$ -Lactamases”, Faculty of Medicine, Université Paris-Sud, Université Paris-Saclay, Le Kremlin-Bicêtre, France

**Maud Gayral** – Institut de Chimie Moléculaire et des Matériaux d’Orsay (ICMMO), CNRS, Université Paris Sud, Université Paris-Saclay, 91405 Orsay Cedex, France

**Jean-Bernard Créchet** – Ecole Polytechnique, Route de Saclay, F-91120 Palaiseau, France

**Naïma Nhiri** – Institut de Chimie des Substances Naturelles, CNRS UPR 2301, Université Paris-Sud, Université Paris-Saclay, 91190 Gif-sur-Yvette, France

**Eric Jacquet** – Institut de Chimie des Substances Naturelles, CNRS UPR 2301, Université Paris-Sud, Université Paris-Saclay, 91190 Gif-sur-Yvette, France

**Jean-Christophe Cintrat** – Service de Chimie Bio-organique et Marquage (SCBM), CEA, Université Paris-Saclay, 91191 Gif-sur-Yvette, France; [orcid.org/0000-0001-5758-8077](https://orcid.org/0000-0001-5758-8077)

**François Giraud** – Institut de Chimie des Substances Naturelles, CNRS UPR 2301, Université Paris-Sud, Université Paris-Saclay, 91190 Gif-sur-Yvette, France

**Carine van Heijenoort** – Institut de Chimie des Substances Naturelles, CNRS UPR 2301, Université Paris-Sud, Université

Paris-Saclay, 91190 Gif-sur-Yvette, France; [orcid.org/0000-0002-2839-1037](https://orcid.org/0000-0002-2839-1037)

**Ewen Lescop** – Institut de Chimie des Substances Naturelles, CNRS UPR 2301, Université Paris-Sud, Université Paris-Saclay, 91190 Gif-sur-Yvette, France; [orcid.org/0000-0002-2623-9365](https://orcid.org/0000-0002-2623-9365)

**Stéphanie Pethe** – EA7361 “Structure, Dynamic, Function and Expression of Broad Spectrum  $\beta$ -Lactamases”, Faculty of Medicine, Université Paris-Sud, Université Paris-Saclay, Le Kremlin-Bicêtre, France

**Bogdan I. Iorga** – Institut de Chimie des Substances Naturelles, CNRS UPR 2301, Université Paris-Sud, Université Paris-Saclay, 91190 Gif-sur-Yvette, France; [orcid.org/0000-0003-0392-1350](https://orcid.org/0000-0003-0392-1350)

**Eric Guittet** – Institut de Chimie des Substances Naturelles, CNRS UPR 2301, Université Paris-Sud, Université Paris-Saclay, 91190 Gif-sur-Yvette, France

Complete contact information is available at:

<https://pubs.acs.org/10.1021/acsomega.0c00590>

### Author Contributions

The manuscript was written through contributions of all authors. All authors have given approval to the final version of the manuscript.

### Funding

This work was supported by the Assistance Publique—Les Hôpitaux de Paris (AP-HP), the University Paris-Sud, the Laboratory of Excellence in Research on Medication and Innovative Therapeutics (LERMIT) supported by a grant from the French National Research Agency [ANR-10-LABX-33] and by the Joint Programming Initiative on Antimicrobial Resistance (JPIAMR) DesInMBL [ANR-14-JAMR-002], and the French National Centre for Scientific Research-CNRS. Financial support from the IR-RMN-THC Fr3050 CNRS for conducting the research is gratefully acknowledged.

### Notes

The authors declare no competing financial interest.

### ABBREVIATIONS

GNB, Gram-negative bacteria; MBLs, metallo- $\beta$ -lactamases; MDR, multidrug resistance; NDM-1, New Delhi metallo- $\beta$ -lactamase-1; MICs, minimum inhibitory concentrations; CSPs, chemical shift perturbations; ASL, active site loop; PDB, Protein Data Bank; HADDOCK, High Ambiguity Driven biomolecular DOCKing; art-apo, artificial apo

### REFERENCES

- (1) Oliveira, J.; Reygaert, W. C. Gram Negative Bacteria. *StatPearls*; Treasure Island: FL, 2019.
- (2) Ruppé, E.; Woerther, P. L.; Barbier, F. Mechanisms of antimicrobial resistance in Gram-negative bacilli. *Ann. Intensive Care* **2015**, *5*, No. 61.
- (3) Vasoo, S.; Barreto, J. N.; Tosh, P. K. Emerging issues in gram-negative bacterial resistance: an update for the practicing clinician. *Mayo Clin. Proc.* **2015**, *90*, 395–403.
- (4) Ambler, R. P. The structure of beta-lactamases. *Philos. Trans. R. Soc., B* **1980**, *289*, 321–331.
- (5) Naas, T.; Oueslati, S.; Bonnin, R. A.; Dabos, M. L.; Zavala, A.; Dortet, L.; Retailleau, P.; Iorga, B. I. Beta-lactamase database (BLDB) - structure and function. *J. Enzyme Inhib. Med. Chem.* **2017**, *32*, 917–919.

- (6) Nordmann, P.; Naas, T.; Poirel, L. Global spread of Carbapenemase-producing Enterobacteriaceae. *Emerging Infect. Dis.* **2011**, *17*, 1791–1798.
- (7) Page, M. I. The reactivity of beta-lactams, the mechanism of catalysis and the inhibition of beta-lactamases. *Curr. Pharm. Des.* **1999**, *5*, 895–913.
- (8) Bebrone, C. Metallo-beta-lactamases (classification, activity, genetic organization, structure, zinc coordination) and their super-family. *Biochem. Pharmacol.* **2007**, *74*, 1686–1701.
- (9) Bonomo, R. A. New Delhi Metallo-beta-Lactamase and Multidrug Resistance: A Global SOS? *Clin. Infect. Dis.* **2011**, *52*, 485–487.
- (10) Kumarasamy, K. K.; Toleman, M. A.; Walsh, T. R.; Bagaria, J.; Butt, F.; Balakrishnan, R.; Chaudhary, U.; Doumith, M.; Giske, C. G.; Irfan, S.; Krishnan, P.; Kumar, A. V.; Maharjan, S.; Mushtaq, S.; Noorie, T.; Paterson, D. L.; Pearson, A.; Perry, C.; Pike, R.; Rao, B.; Ray, U.; Sarma, J. B.; Sharma, M.; Sheridan, E.; Thirunarayan, M. A.; Turton, J.; Upadhyay, S.; Warner, M.; Welfare, W.; Livermore, D. M.; Woodford, N. Emergence of a new antibiotic resistance mechanism in India, Pakistan, and the UK: a molecular, biological, and epidemiological study. *Lancet Infect. Dis.* **2010**, *10*, 597–602.
- (11) Koh, T. H.; Khoo, C. T.; Wijaya, L.; Leong, H. N.; Lo, Y. L.; Lim, L. C.; Koh, T. Y. Global spread of New Delhi metallo-beta-lactamase I. *Lancet Infect. Dis.* **2010**, *10*, 828.
- (12) Nordmann, P.; Poirel, L.; Walsh, T. R.; Livermore, D. M. The emerging NDM carbapenemases. *Trends Microbiol.* **2011**, *19*, 588–595.
- (13) Kim, Y.; Tesar, C.; Mire, J.; Jedrzejczak, R.; Binkowski, A.; Babnigg, G.; Sacchetti, J.; Joachimiak, A. Structure of apo- and monometalated forms of NDM-1—a highly potent carbapenem-hydrolyzing metallo-beta-lactamase. *PLoS One* **2011**, *6*, No. e24621.
- (14) Zhang, H.; Hao, Q. Crystal structure of NDM-1 reveals a common beta-lactam hydrolysis mechanism. *FASEB J.* **2011**, *25*, 2574–2582.
- (15) King, D.; Strynadka, N. Crystal structure of New Delhi metallo-beta-lactamase reveals molecular basis for antibiotic resistance. *Protein Sci.* **2011**, *20*, 1484–1491.
- (16) King, D. T.; Worrall, L. J.; Gruninger, R.; Strynadka, N. C. New Delhi metallo-beta-lactamase: structural insights into beta-lactam recognition and inhibition. *J. Am. Chem. Soc.* **2012**, *134*, 11362–11365.
- (17) Guo, Y.; Wang, J.; Niu, G.; Shui, W.; Sun, Y.; Zhou, H.; Zhang, Y.; Yang, C.; Lou, Z.; Rao, Z. A structural view of the antibiotic degradation enzyme NDM-1 from a superbug. *Protein Cell* **2011**, *2*, 384–394.
- (18) Kim, Y.; Cunningham, M. A.; Mire, J.; Tesar, C.; Sacchetti, J.; Joachimiak, A. NDM-1, the ultimate promiscuous enzyme: substrate recognition and catalytic mechanism. *FASEB J.* **2013**, *27*, 1917–1927.
- (19) Liang, Z.; Li, L.; Wang, Y.; Chen, L.; Kong, X.; Hong, Y.; Lan, L.; Zheng, M.; Guang-Yang, C.; Liu, H.; Shen, X.; Luo, C.; Li, K. K.; Chen, K.; Jiang, H. Molecular basis of NDM-1, a new antibiotic resistance determinant. *PLoS One* **2011**, *6*, No. e23606.
- (20) Feng, H.; Ding, J.; Zhu, D.; Liu, X.; Xu, X.; Zhang, Y.; Zang, S.; Wang, D. C.; Liu, W. Structural and mechanistic insights into NDM-1 catalyzed hydrolysis of cephalosporins. *J. Am. Chem. Soc.* **2014**, *136*, 14694–14697.
- (21) Zhu, K.; Lu, J.; Ye, F.; Jin, L.; Kong, X.; Liang, Z.; Chen, Y.; Yu, K.; Jiang, H.; Li, J. Q.; Luo, C. Structure-based computational study of the hydrolysis of New Delhi metallo-beta-lactamase-1. *Biochem. Biophys. Res. Commun.* **2013**, *431*, 2–7.
- (22) Chen, J.; Wang, J.; Zhu, W. Zinc ion-induced conformational changes in new Delhi metallo-beta-lactamase I probed by molecular dynamics simulations and umbrella sampling. *Phys. Chem. Chem. Phys.* **2017**, *19*, 3067–3075.
- (23) Thomas, P. W.; Zheng, M.; Wu, S.; Guo, H.; Liu, D.; Xu, D.; Fast, W. Characterization of purified New Delhi metallo-beta-lactamase-1. *Biochemistry* **2011**, *50*, 10102–10113.
- (24) Cheng, Z.; Thomas, P. W.; Ju, L.; Bergstrom, A.; Mason, K.; Clayton, D.; Miller, C.; Bethel, C. R.; VanPelt, J.; Tierney, D. L.; Page, R. C.; Bonomo, R. A.; Fast, W.; Crowder, M. W. Evolution of New Delhi metallo-beta-lactamase (NDM) in the clinic: Effects of NDM mutations on stability, zinc affinity, and mono-zinc activity. *J. Biol. Chem.* **2018**, *293*, 12606–12618.
- (25) Tooke, C. L.; Hinchliffe, P.; Bragginton, E. C.; Colenso, C. K.; Hirvonen, V. H. A.; Takebayashi, Y.; Spencer, J. beta-Lactamases and beta-Lactamase Inhibitors in the 21st Century. *J. Mol. Biol.* **2019**, *431*, 3472–3500.
- (26) Linciano, P.; Cendron, L.; Gianquinto, E.; Spyraakis, F.; Tondi, D. Ten Years with New Delhi Metallo-beta-lactamase-1 (NDM-1): From Structural Insights to Inhibitor Design. *ACS Infect. Dis.* **2019**, *5*, 9–34.
- (27) Li, N.; Xu, Y.; Xia, Q.; Bai, C.; Wang, T.; Wang, L.; He, D.; Xie, N.; Li, L.; Wang, J.; Zhou, H. G.; Xu, F.; Yang, C.; Zhang, Q.; Yin, Z.; Guo, Y.; Chen, Y. Simplified captopril analogues as NDM-1 inhibitors. *Bioorg. Med. Chem. Lett.* **2014**, *24*, 386–389.
- (28) Liu, S.; Jing, L.; Yu, Z. J.; Wu, C.; Zheng, Y.; Zhang, E.; Chen, Q.; Yu, Y.; Guo, L.; Wu, Y.; Li, G. B. ((S)-3-Mercapto-2-methylpropanamido)acetic acid derivatives as metallo-beta-lactamase inhibitors: Synthesis, kinetic and crystallographic studies. *Eur. J. Med. Chem.* **2018**, *145*, 649–660.
- (29) Klingler, F. M.; Wichelhaus, T. A.; Frank, D.; Cuesta-Bernal, J.; El-Delik, J.; Muller, H. F.; Sjuts, H.; Gottig, S.; Koenigs, A.; Pos, K. M.; Pogoryelov, D.; Proschak, E. Approved Drugs Containing Thiols as Inhibitors of Metallo-beta-lactamases: Strategy To Combat Multidrug-Resistant Bacteria. *J. Med. Chem.* **2015**, *58*, 3626–3630.
- (30) Zhang, Y. L.; Yang, K. W.; Zhou, Y. J.; LaCuran, A. E.; Oelschlaeger, P.; Crowder, M. W. Diaryl-substituted azolythioacetamides: Inhibitor discovery of New Delhi metallo-beta-lactamase-1 (NDM-1). *ChemMedChem* **2014**, *9*, 2445–2448.
- (31) Zhai, L.; Zhang, Y. L.; Kang, J. S.; Oelschlaeger, P.; Xiao, L.; Nie, S. S.; Yang, K. W. Triazolylthioacetamide: A Valid Scaffold for the Development of New Delhi Metallo-beta-Lactamase-1 (NDM-1) Inhibitors. *ACS Med. Chem. Lett.* **2016**, *7*, 413–417.
- (32) Livermore, D. M.; Mushtaq, S.; Morinaka, A.; Ida, T.; Maebashi, K.; Hope, R. Activity of carbapenems with ME1071 (disodium 2,3-diethylmaleate) against Enterobacteriaceae and Acinetobacter spp. with carbapenemases, including NDM enzymes. *J. Antimicrob. Chemother.* **2013**, *68*, 153–158.
- (33) Brem, J.; van Berkel, S. S.; Aik, W.; Rydzik, A. M.; Avison, M. B.; Pettinati, I.; Umland, K. D.; Kawamura, A.; Spencer, J.; Claridge, T. D.; McDonough, M. A.; Schofield, C. J. Rhodanine hydrolysis leads to potent thioenolate mediated metallo-beta-lactamase inhibition. *Nat. Chem.* **2014**, *6*, 1084–1090.
- (34) González, M. M.; Kosmopoulou, M.; Mojica, M. F.; Castillo, V.; Hinchliffe, P.; Pettinati, I.; Brem, J.; Schofield, C. J.; Mahler, G.; Bonomo, R. A.; Llarrull, L. I.; Spencer, J.; Vila, A. J. Bisthiazolidines: A Substrate-Mimicking Scaffold as an Inhibitor of the NDM-1 Carbapenemase. *ACS Infect. Dis.* **2015**, *1*, 544–554.
- (35) Klingler, F. M.; Moser, D.; Buttner, D.; Wichelhaus, T. A.; Lohr, F.; Dotsch, V.; Proschak, E. Probing metallo-beta-lactamases with molecular fragments identified by consensus docking. *Bioorg. Med. Chem. Lett.* **2015**, *25*, 5243–5246.
- (36) Christopheit, T.; Leiros, H. K. Fragment-based discovery of inhibitor scaffolds targeting the metallo-beta-lactamases NDM-1 and VIM-2. *Bioorg. Med. Chem. Lett.* **2016**, *26*, 1973–1977.
- (37) Wang, X.; Lu, M.; Shi, Y.; Ou, Y.; Cheng, X. Discovery of novel new Delhi metallo-beta-lactamases-1 inhibitors by multistep virtual screening. *PLoS One* **2015**, *10*, No. e0118290.
- (38) Sun, N.; Du, R. L.; Zheng, Y. Y.; Guo, Q.; Cai, S. Y.; Liu, Z. H.; Fang, Z. Y.; Yuan, W. C.; Liu, T.; Li, X. M.; Lu, Y. J.; Wong, K. Y. Antibacterial activity of 3-methylbenzo[d]thiazol-methylquinolinium derivatives and study of their action mechanism. *J. Enzyme Inhib. Med. Chem.* **2018**, *33*, 879–889.
- (39) Liu, Y.; Hu, X.; Wu, Y.; Zhang, W.; Chen, X.; You, X.; Hu, L. Synthesis and structure-activity relationship of novel bisindole amidines active against MDR Gram-positive and Gram-negative bacteria. *Eur. J. Med. Chem.* **2018**, *150*, 771–782.

- (40) Yu, Z. J.; Liu, S.; Zhou, S.; Li, H.; Yang, F.; Yang, L. L.; Wu, Y.; Guo, L.; Li, G. B. Virtual target screening reveals rosmarinic acid and salvianolic acid A inhibiting metallo- and serine-beta-lactamases. *Bioorg. Med. Chem. Lett.* **2018**, *28*, 1037–1042.
- (41) Zhang, E.; Wang, M. M.; Huang, S. C.; Xu, S. M.; Cui, D. Y.; Bo, Y. L.; Bai, P. Y.; Hua, Y. G.; Xiao, C. L.; Qin, S. NOTA analogue: A first dithiocarbamate inhibitor of metallo-beta-lactamases. *Bioorg. Med. Chem. Lett.* **2018**, *28*, 214–221.
- (42) Chu, W. C.; Bai, P. Y.; Yang, Z. Q.; Cui, D. Y.; Hua, Y. G.; Yang, Y.; Yang, Q. Q.; Zhang, E.; Qin, S. Synthesis and antibacterial evaluation of novel cationic chalcone derivatives possessing broad spectrum antibacterial activity. *Eur. J. Med. Chem.* **2018**, *143*, 905–921.
- (43) Xiang, Y.; Chang, Y. N.; Ge, Y.; Kang, J. S.; Zhang, Y. L.; Liu, X. L.; Oelschlaeger, P.; Yang, K. W. Azolythioacetamides as a potent scaffold for the development of metallo-beta-lactamase inhibitors. *Bioorg. Med. Chem. Lett.* **2017**, *27*, 5225–5229.
- (44) Chen, A. Y.; Thomas, P. W.; Stewart, A. C.; Bergstrom, A.; Cheng, Z.; Miller, C.; Bethel, C. R.; Marshall, S. H.; Credille, C. V.; Riley, C. L.; Page, R. C.; Bonomo, R. A.; Crowder, M. W.; Tierney, D. L.; Fast, W.; Cohen, S. M. Dipicolinic Acid Derivatives as Inhibitors of New Delhi Metallo-beta-lactamase-1. *J. Med. Chem.* **2017**, *60*, 7267–7283.
- (45) Bush, K.; Bradford, P. A. Interplay between beta-lactamases and new beta-lactamase inhibitors. *Nat. Rev. Microbiol.* **2019**, *17*, 295–306.
- (46) Everett, M.; Sprynski, N.; Coelho, A.; Castandet, J.; Bayet, M.; Bougnon, J.; Lozano, C.; Davies, D. T.; Leiris, S.; Zalacain, M.; Morrissey, I.; Magnet, S.; Holden, K.; Warn, P.; De Luca, F.; Docquier, J. D.; Lemonnier, M. Discovery of a Novel Metallo-beta-Lactamase Inhibitor That Potentiates Meropenem Activity against Carbapenem-Resistant Enterobacteriaceae. *Antimicrob. Agents Chemother.* **2018**, *62*, No. e00074-18.
- (47) Li, T.; Wang, Q.; Chen, F.; Li, X.; Luo, S.; Fang, H.; Wang, D.; Li, Z.; Hou, X.; Wang, H. Biochemical characteristics of New Delhi metallo-beta-lactamase-1 show unexpected difference to other MBLs. *PLoS One* **2013**, *8*, No. e61914.
- (48) King, A. M.; Reid-Yu, S. A.; Wang, W.; King, D. T.; De Pascale, G.; Strynadka, N. C.; Walsh, T. R.; Coombes, B. K.; Wright, G. D. Aspergillomarasmine A overcomes metallo-beta-lactamase antibiotic resistance. *Nature* **2014**, *510*, 503–506.
- (49) Zhang, J.; Wang, S.; Wei, Q.; Guo, Q.; Bai, Y.; Yang, S.; Song, F.; Zhang, L.; Lei, X. Synthesis and biological evaluation of Aspergillomarasmine A derivatives as novel NDM-1 inhibitor to overcome antibiotics resistance. *Bioorg. Med. Chem.* **2017**, *25*, 5133–5141.
- (50) Shi, C.; Bao, J.; Sun, Y.; Kang, X.; Lao, X.; Zheng, H. Discovery of Baicalin as NDM-1 inhibitor: Virtual screening, biological evaluation and molecular simulation. *Bioorg. Chem.* **2019**, *88*, No. 102953.
- (51) Liu, S.; Zhou, Y.; Niu, X.; Wang, T.; Li, J.; Liu, Z.; Wang, J.; Tang, S.; Wang, Y.; Deng, X. Magnolol restores the activity of meropenem against NDM-1-producing *Escherichia coli* by inhibiting the activity of metallo-beta-lactamase. *Cell Death Discovery* **2018**, *4*, No. 28.
- (52) Shi, C.; Chen, J.; Xiao, B.; Kang, X.; Lao, X.; Zheng, H. Discovery of NDM-1 inhibitors from natural products. *J. Global Antimicrob. Resist.* **2019**, *18*, 80–87.
- (53) Cody, V.; Middleton, E.; Harbone, J. B. In *Biochemical, Pharmacological, and Structure-Activity Relationships*, Proceedings on the Plant Flavonoids in Biology and Medicine, Buffalo, Vol. 1. Alan. R. Liss, Ed.; Academic Press: New York, 1986.
- (54) Cao, S.; Jiang, X.; Chen, J. Effect of Zinc (II) on the interactions of bovine serum albumin with flavonols bearing different number of hydroxyl substituent on B-ring. *J. Inorg. Biochem.* **2010**, *104*, 146–152.
- (55) Guerrero, L.; Castillo, J.; Quinones, M.; Garcia-Vallve, S.; Arola, L.; Pujadas, G.; Muguerza, B. Inhibition of Angiotensin-Converting Enzyme Activity by Flavonoids: Structure-Activity Relationship Studies. *PLoS One* **2012**, *7*, No. e49493.
- (56) Tolomeo, M.; Grimaudo, S.; Di Cristina, A.; Pipitone, R. M.; Dusonchet, L.; Meli, M.; Crosta, L.; Gebbia, N.; Invidiata, F. P.; Titone, L.; Simoni, D. Galangin increases the cytotoxic activity of imatinib mesylate in imatinib-sensitive and imatinib-resistant Bcr-Abl expressing leukemia cells. *Cancer Lett.* **2008**, *265*, 289–297.
- (57) Grundmann, O.; Nakajima, J.-I.; Kamata, K.; Seo, S.; Butterweck, V. Kaempferol from the leaves of *Apocynum venetum* possesses anxiolytic activities in the elevated plus maze test in mice. *Phytomedicine* **2009**, *16*, 295–302.
- (58) Chimenti, F.; Cottiglia, F.; Bonsignore, L.; Casu, L.; Casu, M.; Floris, C.; Secci, D.; Bolasco, A.; Chimenti, P.; Granese, A.; Befani, O.; Turini, P.; Alcaro, S.; Ortuso, F.; Trombetta, G.; Loizzo, A.; Guarino, I. Quercetin as the active principle of *Hypericum hircinum* exerts a selective inhibitory activity against MAO-A: Extraction, biological analysis, and computational study. *J. Nat. Prod.* **2006**, *69*, 945–949.
- (59) Fahlman, B. M.; Krol, E. S. Inhibition of UVA and UVB Radiation-Induced Lipid Oxidation by Quercetin. *J. Agric. Food Chem.* **2009**, *57*, 5301–5305.
- (60) Lu, J.; Papp, L. V.; Fang, J. G.; Rodriguez-Nieto, S.; Zhivotovsky, B.; Holmgren, A. Inhibition of mammalian thioredoxin reductase by some flavonoids: Implications for myricetin and quercetin anticancer activity. *Cancer Res.* **2006**, *66*, 4410–4418.
- (61) Hsu, Y.-L.; Chang, J.-K.; Tsai, C.-H.; Chien, T.-T. C.; Kuo, P.-L. Myricetin induces human osteoblast differentiation through bone morphogenetic protein-2/p38 mitogen-activated protein kinase pathway. *Biochem. Pharmacol.* **2007**, *73*, 504–514.
- (62) Kwon, O.; Eck, P.; Chen, S.; Corpe, C. P.; Lee, J.-H.; Kruhlak, M.; Levine, M. Inhibition of the intestinal glucose transporter GLUT2 by flavonoids. *FASEB J.* **2007**, *21*, 366–377.
- (63) Zheng, B.; Tan, S.; Gao, J.; Han, H.; Liu, J.; Lu, G.; Liu, D.; Yi, Y.; Zhu, B.; Gao, G. F. An unexpected similarity between antibiotic-resistant NDM-1 and beta-lactamase II from *Erythrobacter litoralis*. *Protein Cell* **2011**, *2*, 250–258.
- (64) Materon, I. C.; Beharry, Z.; Huang, W. Z.; Perez, C.; Palzkill, T. Analysis of the context dependent sequence requirements of active site residues in the metallo-beta-lactamase IMP-1. *J. Mol. Biol.* **2004**, *344*, 653–663.
- (65) Yao, C.; Wu, Q.; Xu, G.; Li, C. NMR backbone resonance assignment of New Delhi metallo-beta-lactamase. *Biomol. NMR Assignments* **2017**, *11*, 239–242.
- (66) Shen, Y.; Bax, A. Protein backbone and sidechain torsion angles predicted from NMR chemical shifts using artificial neural networks. *J. Biomol. NMR* **2013**, *56*, 227–241.
- (67) King, D.; Strynadka, N. Crystal structure of New Delhi metallo-beta-lactamase reveals molecular basis for antibiotic resistance. *Protein Sci.* **2011**, *20*, 1484–1491.
- (68) Sun, Z.; Liu, Q.; Qu, G.; Feng, Y.; Reetz, M. T. Utility of B-Factors in Protein Science: Interpreting Rigidity, Flexibility, and Internal Motion and Engineering Thermostability. *Chem. Rev.* **2019**, *119*, 1626–1665.
- (69) Green, V. L.; Verma, A.; Owens, R. J.; Phillips, S. E.; Carr, S. B. Structure of New Delhi metallo-beta-lactamase 1 (NDM-1). *Acta Crystallogr., Sect. F: Struct. Biol. Cryst. Commun.* **2011**, *67*, 1160–1164.
- (70) Chen, J.; Chen, H.; Shi, Y.; Hu, F.; Lao, X.; Gao, X.; Zheng, H.; Yao, W. Probing the effect of the non-active-site mutation Y229W in New Delhi metallo-beta-lactamase-1 by site-directed mutagenesis, kinetic studies, and molecular dynamics simulations. *PLoS One* **2013**, *8*, No. e82080.
- (71) Dajas, F.; Andres Abin-Carriquiry, J.; Arredondo, F.; Blasina, F.; Echeverry, C.; Martinez, M.; Rivera, F.; Vaamonde, L. Quercetin in brain diseases: Potential and limits. *Neurochem. Int.* **2015**, *89*, 140–148.
- (72) Brito, A. F.; Ribeiro, M.; Abrantes, A. M.; Pires, A. S.; Teixo, R. J.; Tralhao, J. G.; Botelho, M. F. Quercetin in Cancer Treatment, Alone or in Combination with Conventional Therapeutics? *Curr. Med. Chem.* **2015**, *22*, 3025–3039.

- (73) Ganugapati, M.; Sirisha, V.; Mukkavalli, S.; Atimamula, S.; Sai, S. Insilico modeling and docking studies of new delhi metallo Beta lactamase-1 (super bug). *Int. J. Eng. Sci. Res. Technol.* **2011**, *3*, 2427–2434.
- (74) Padmavathi, M.; Prasanth Reddy, V.; Rao, R. Inhibition of NDM-1 in superbugs by flavonoids- an insilico approach. *J. Adv. Bioinf. Appl. Res.* **2012**, *3*, 328–332.
- (75) van Zundert, G. C. P.; Rodrigues, J.; Trellet, M.; Schmitz, C.; Kastiris, P. L.; Karaca, E.; Melquiond, A. S. J.; van Dijk, M.; de Vries, S. J.; Bonvin, A. The HADDOCK2.2 Web Server: User-Friendly Integrative Modeling of Biomolecular Complexes. *J. Mol. Biol.* **2016**, *428*, 720–725.
- (76) Erickson, J. A.; Jalaie, M.; Robertson, D. H.; Lewis, R. A.; Vieth, M. Lessons in molecular recognition: the effects of ligand and protein flexibility on molecular docking accuracy. *J. Med. Chem.* **2004**, *47*, 45–55.
- (77) Zhang, H.; Ma, G.; Zhu, Y.; Zeng, L.; Ahmad, A.; Wang, C.; Pang, B.; Fang, H.; Zhao, L.; Hao, Q. Active-Site Conformational Fluctuations Promote the Enzymatic Activity of NDM-1. *Antimicrob. Agents Chemother.* **2018**, *62*, No. e01579-18.
- (78) Mira, L.; Fernandez, M. T.; Santos, M.; Rocha, R.; Florencio, M. H.; Jennings, K. R. Interactions of flavonoids with iron and copper ions: A mechanism for their antioxidant activity. *Free Radical Res.* **2002**, *36*, 1199–1208.
- (79) Grazul, M.; Budzisz, E. Biological activity of metal ions complexes of chromones, coumarins and flavones. *Coord. Chem. Rev.* **2009**, *253*, 2588–2598.
- (80) Liu, Y.; Guo, M. Studies on transition metal-quercetin complexes using electrospray ionization tandem mass spectrometry. *Molecules* **2015**, *20*, 8583–8594.
- (81) Dolatabadi, J. E. Molecular aspects on the interaction of quercetin and its metal complexes with DNA. *Int. J. Biol. Macromol.* **2011**, *48*, 227–233.
- (82) Bhuiya, S.; Haque, L.; Pradhan, A. B.; Das, S. Inhibitory effects of the dietary flavonoid quercetin on the enzyme activity of zinc(II)-dependent yeast alcohol dehydrogenase: Spectroscopic and molecular docking studies. *Int. J. Biol. Macromol.* **2017**, *95*, 177–184.
- (83) Steiner, R. A.; Kalk, K. H.; Dijkstra, B. W. Anaerobic enzyme-substrate structures provide insight into the reaction mechanism of the copper-dependent quercetin 2,3-dioxygenase. *Proc. Natl. Acad. Sci. U.S.A.* **2002**, *99*, 16625–16630.
- (84) Jeoung, J. H.; Nianios, D.; Fetzner, S.; Dobbek, H. Quercetin 2,4-Dioxygenase Activates Dioxygen in a Side-On O<sub>2</sub>-Ni Complex. *Angew. Chem., Int. Ed.* **2016**, *55*, 3281–3284.
- (85) Aoki, N.; Ishii, Y.; Tateda, K.; Saga, T.; Kimura, S.; Kikuchi, Y.; Kobayashi, T.; Tanabe, Y.; Tsukada, H.; Gejyo, F.; Yamaguchi, K. Efficacy of calcium-EDTA as an inhibitor for metallo-beta-lactamase in a mouse model of *Pseudomonas aeruginosa* pneumonia. *Antimicrob. Agents Chemother.* **2010**, *54*, 4582–4588.
- (86) Ma, J.; McLeod, S.; MacCormack, K.; Sriram, S.; Gao, N.; Breeze, A. L.; Hu, J. Real-time monitoring of New Delhi metallo-beta-lactamase activity in living bacterial cells by <sup>1</sup>H NMR spectroscopy. *Angew. Chem., Int. Ed.* **2014**, *53*, 2130–2133.
- (87) Bergstrom, A.; Katko, A.; Adkins, Z.; Hill, J.; Cheng, Z.; Burnett, M.; Yang, H.; Aitha, M.; Mehaffey, M. R.; Brodbelt, J. S.; Tehrani, K.; Martin, N. I.; Bonomo, R. A.; Page, R. C.; Tierney, D. L.; Fast, W.; Wright, G. D.; Crowder, M. W. Probing the Interaction of Aspergillomarasmine A with Metallo-beta-lactamases NDM-1, VIM-2, and IMP-7. *ACS Infect. Dis.* **2018**, *4*, 135–145.
- (88) Hinchliffe, P.; Gonzalez, M. M.; Mojica, M. F.; Gonzalez, J. M.; Castillo, V.; Saiz, C.; Kosmopoulou, M.; Tooke, C. L.; Llarrull, L. I.; Mahler, G.; Bonomo, R. A.; Vila, A. J.; Spencer, J. Cross-class metallo-beta-lactamase inhibition by bisthiazolidines reveals multiple binding modes. *Proc. Natl. Acad. Sci. U.S.A.* **2016**, *113*, E3745–E3754.
- (89) Spyrikis, F.; Celenza, G.; Marcocchia, F.; Santucci, M.; Cross, S.; Bellio, P.; Cendron, L.; Perilli, M.; Tondi, D. Structure-Based Virtual Screening for the Discovery of Novel Inhibitors of New Delhi Metallo-beta-lactamase-1. *ACS Med. Chem. Lett.* **2018**, *9*, 45–50.
- (90) Khan, A. U.; Ali, A.; Danishuddin; Srivastava, G.; Sharma, A. Potential inhibitors designed against NDM-1 type metallo-beta-lactamases: an attempt to enhance efficacies of antibiotics against multi-drug-resistant bacteria. *Sci. Rep.* **2017**, *7*, No. 9207.
- (91) Chiou, J.; Wan, S.; Chan, K. F.; So, P. K.; He, D.; Chan, E. W.; Chan, T. H.; Wong, K. Y.; Tao, J.; Chen, S. Ebselen as a potent covalent inhibitor of New Delhi metallo-beta-lactamase (NDM-1). *Chem. Commun.* **2015**, *51*, 9543–9546.
- (92) Rasia, R. M.; Vila, A. J. Structural determinants of substrate binding to *Bacillus cereus* metallo-beta-lactamase. *J. Biol. Chem.* **2004**, *279*, 26046–26051.
- (93) Meini, M. R.; Gonzalez, L. J.; Vila, A. J. Antibiotic resistance in Zn(II)-deficient environments: metallo-beta-lactamase activation in the periplasm. *Future Microbiol.* **2013**, *8*, 947–979.
- (94) Lo, M. C.; Aulabaugh, A.; Jin, G.; Cowling, R.; Bard, J.; Malamas, M.; Ellestad, G. Evaluation of fluorescence-based thermal shift assays for hit identification in drug discovery. *Anal. Biochem.* **2004**, *332*, 153–159.
- (95) Vranken, W. F.; Boucher, W.; Stevens, T. J.; Fogh, R. H.; Pajon, A.; Llinas, M.; et al. The CCPN data model for NMR spectroscopy: development of a software pipeline. *Proteins* **2005**, *59*, 687–696.
- (96) Zhu, G.; Xia, Y. L.; Nicholson, L. K.; Sze, K. H. Protein dynamics measurements by TROSY-based NMR experiments. *J. Magn. Reson.* **2000**, *143*, 423–426.
- (97) Piotto, M.; Saudek, V.; Sklenar, V. Gradient-tailored excitation for single-quantum NMR spectroscopy of aqueous solutions. *J. Biomol. NMR* **1992**, *2*, 661–665.
- (98) Williamson, M. P. Using chemical shift perturbation to characterise ligand binding. *Prog. Nucl. Magn. Reson. Spectrosc.* **2013**, *73*, 1–16.

## Supporting Information

### Figures

#### **NMR characterization of the influence of zinc(II) ions on the structural and dynamic behavior of the New-Delhi Metallo- $\beta$ -lactamase-1 and on the binding with flavonols as inhibitors**

Gwladys Rivière,<sup>†</sup> Saoussen Oueslati,<sup>‡</sup> Maud Gayral,<sup>§</sup> Jean-Bernard Créchet,<sup>||</sup> Naïma Nhiri,<sup>†</sup> Eric Jacquet,<sup>†</sup> Jean-Christophe Cintrat,<sup>⊥</sup> François Giraud,<sup>†</sup> Carine van Heijenoort,<sup>†</sup> Ewen Lescop,<sup>†</sup> Stéphanie Pethe,<sup>‡</sup> Bogdan I. Iorga,<sup>†</sup> Thierry Naas,<sup>\*,‡</sup> Eric Guittet,<sup>†</sup> and Nelly Morellet<sup>\*,†</sup>

<sup>†</sup>Institut de Chimie des Substances Naturelles, CNRS UPR 2301, Université Paris-Sud, Université Paris-Saclay, LabEx LERMIT, 1 avenue de la Terrasse, 91190, Gif-sur-Yvette, France;

<sup>‡</sup>EA7361 'Structure, Dynamic, Function and Expression of Broad Spectrum  $\beta$ -Lactamases', Faculty of Medicine, Université Paris-Sud, LabEx LERMIT, Université Paris-Saclay, Le Kremlin-Bicêtre, France.

<sup>§</sup>Institut de Chimie Moléculaire et des Matériaux d'Orsay (ICMMO), CNRS, Univ Paris Sud, Université Paris-Saclay, 15 rue Georges Clemenceau, 91405 Orsay Cedex, France.

<sup>||</sup>Ecole Polytechnique, Route de Saclay, F-91120 Palaiseau, France;

<sup>⊥</sup>Service de Chimie Bio-organique et Marquage (SCBM), CEA, Université Paris-Saclay, LabEx LERMIT, 91191 Gif/Yvette, France.

#### **\*Corresponding Authors:**

Nelly Morellet : E-mail: nelly.morellet@cns.fr. phone :(33)169823762. Fax : (33)169823784

Thierry Naas: E-mail: thierry.naas@aphp.fr. phone :(33)145212019 or (33)145213030. Fax : (33)145216340

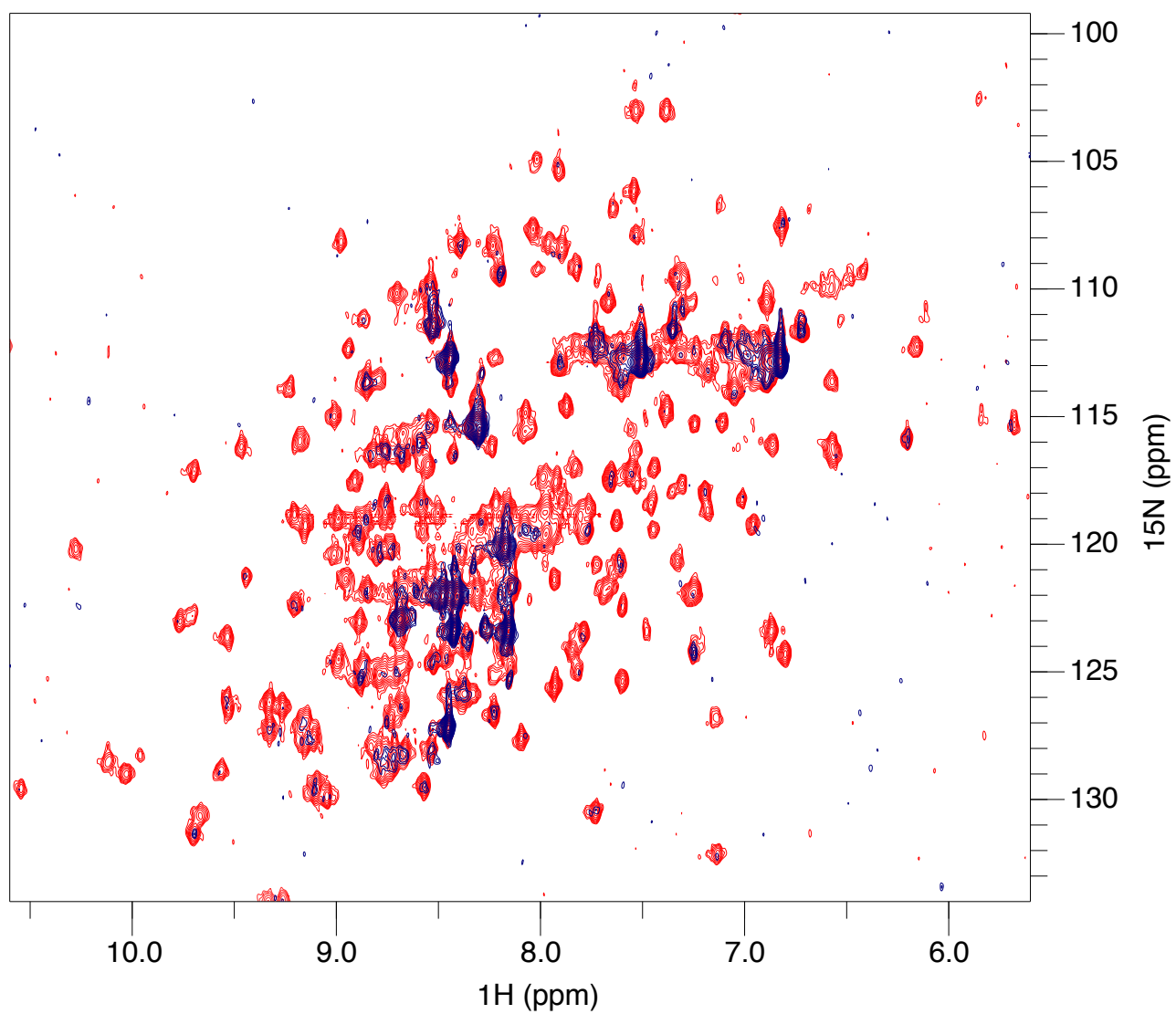


**Figure S1.** Superposition of the 800 MHz  $^1\text{H}$ - $^{15}\text{N}$  HSQC spectra recorded on NDM-1 (332  $\mu\text{M}$ ) in absence of Zn(II) (red) and in presence of 3 molar equivalent of Zn(II) (dark blue) at 20°C in solution in 0.1 mM bis tris pH 7.0, 150 mM NaCl.

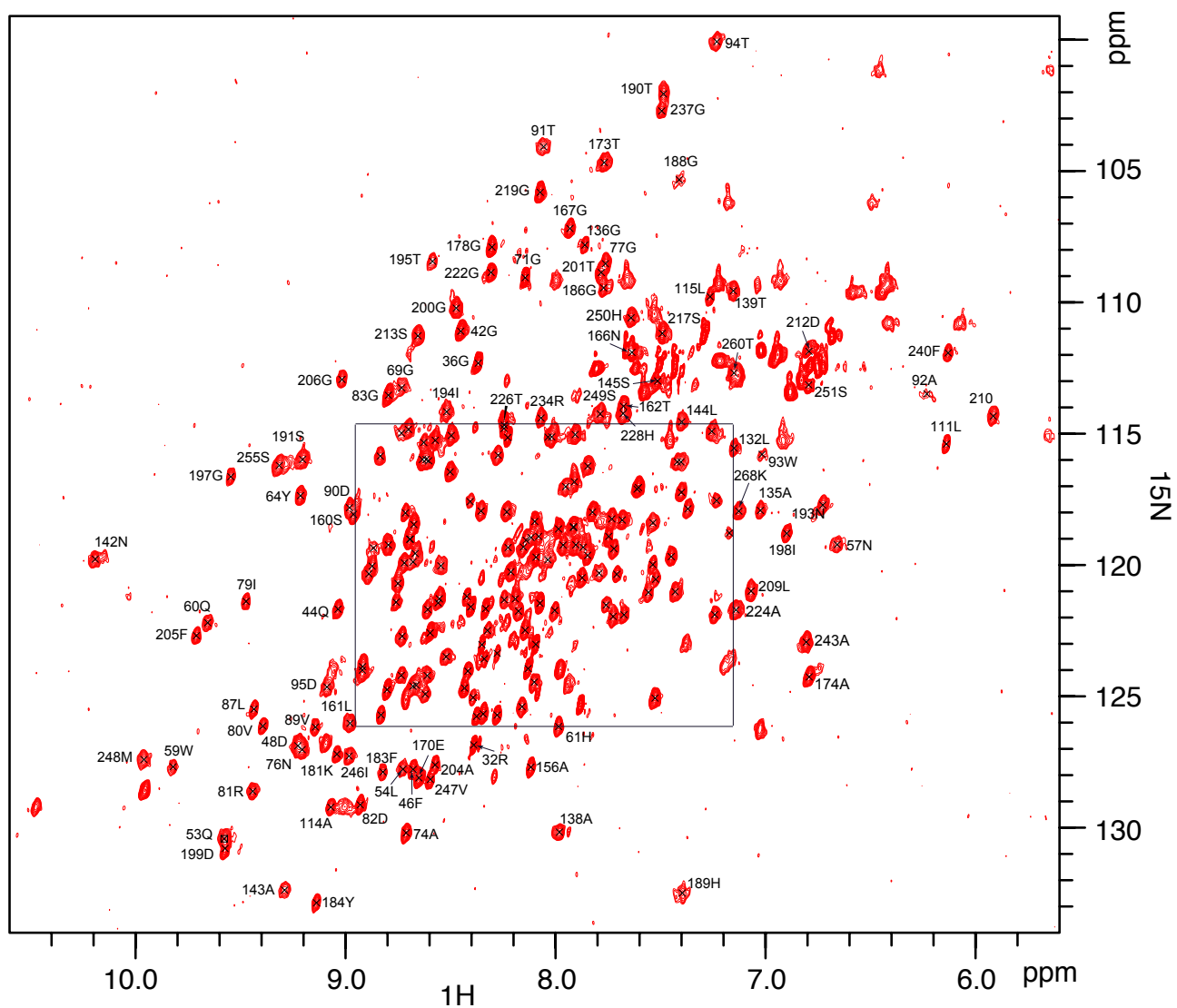


**Figure S2.** 800 MHz  $^1\text{H}$ - $^{15}\text{N}$  HSQC spectra recorded on NDM-1 (550  $\mu\text{M}$ ) in absence of Zn(II) at 20°C in solution in 50mM phosphate buffer pH 7.0.



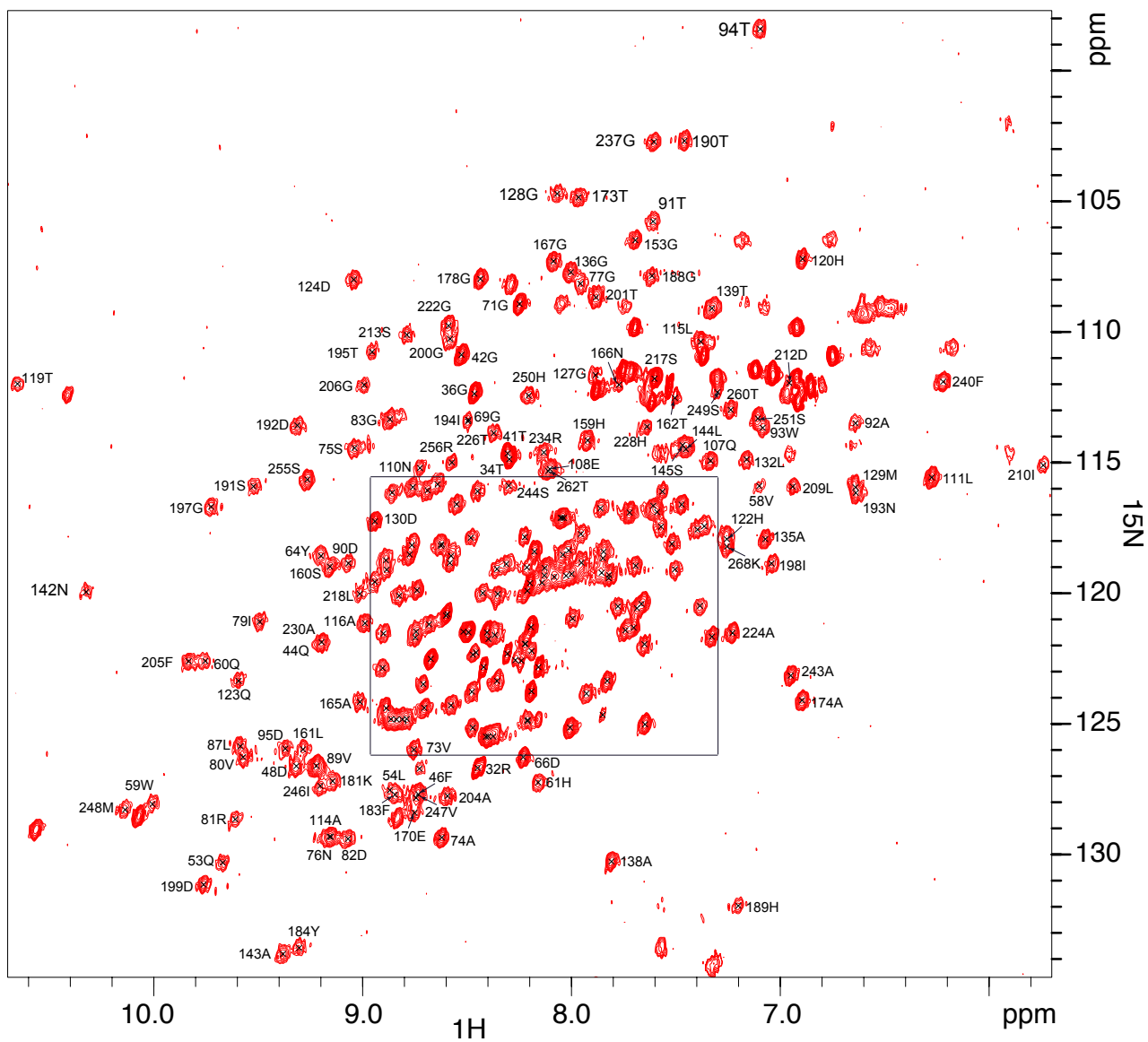


**Figure S4.** 600 MHz  $^1\text{H}$ - $^{15}\text{N}$  HSQC spectra recorded on NDM-1 (996  $\mu\text{M}$ ) in presence of 2 molar equivalents of Zn(II) at 27°C in solution in 0.1 M bis tris pH 7.0, 150 mM NaCl.

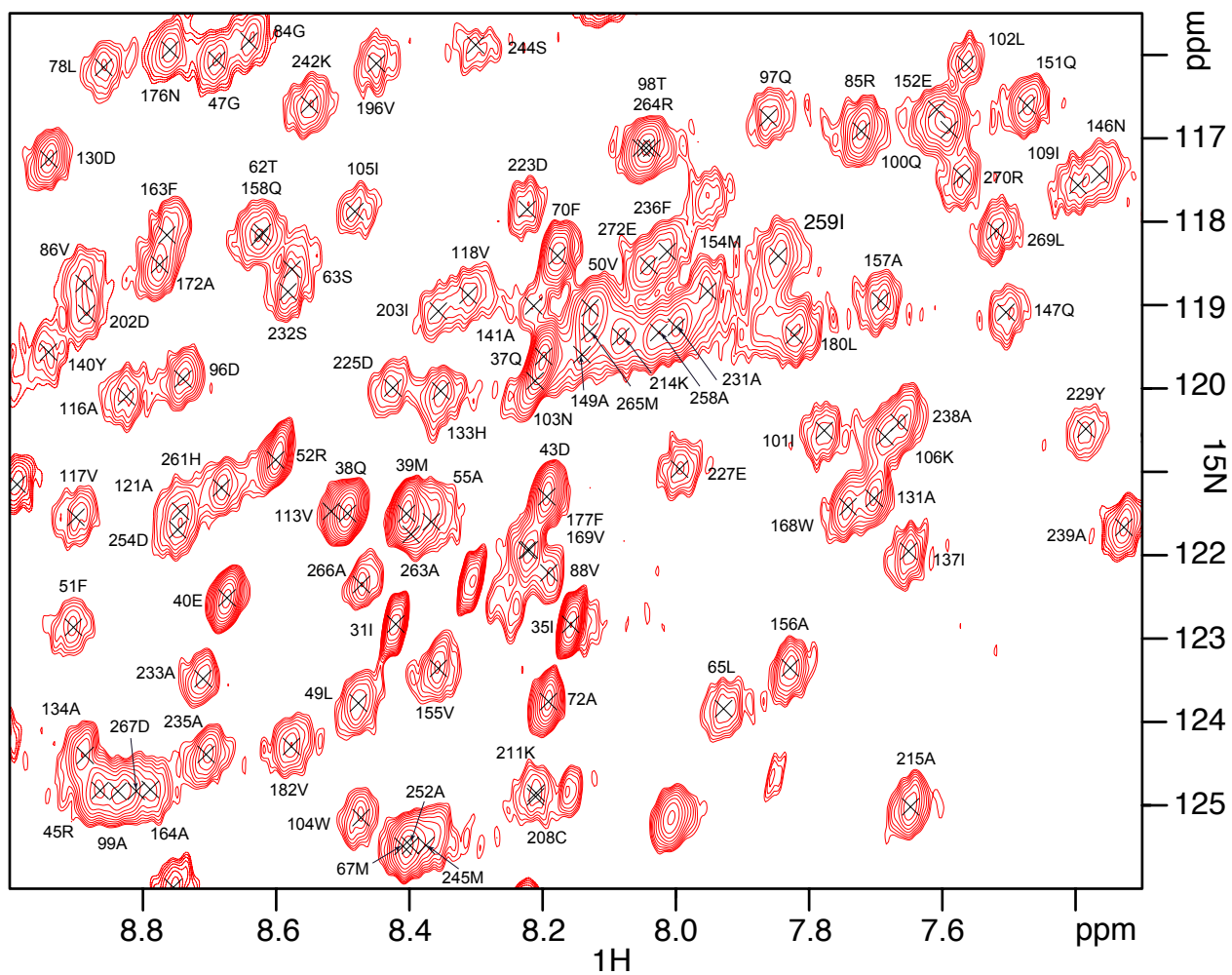


**Figure S5.** Zoom of the 600 MHz  $^1\text{H}$ - $^{15}\text{N}$  HSQC spectra recorded on NDM-1 (996  $\mu\text{M}$ ) in presence of 2 molar equivalents of Zn(II) at 27°C in solution in 0.1 M bis tris pH 7.0, 150 mM NaCl.

### a) NDM-1 in absence of zinc

	28	31	41	L1	51	L2	61	ASL1	71	81	L4
A1) X-ray	MGE	IRPTIGQQME	TGDQRFGDLV	FRQLAPNVWQ	HTSYLDMPGF	GAVASNGLIV	RDGGRVLVVD				
A2) DATA SEQUENCE	MGE	IRPTIGQQME	TGDQRFGDLV	FRQLAPNVWQ	HTSYLDMPGF	GAVASNGLIV	RDGGRVLVVD				
A2) DATA PREDICTED_SS	XXL	LLLLLLLLLL	LLLLLEELLEE	EEEEELLEE	EEEEELLLL	LLLLEEEEEE	EEEEEEEEEL				
A2) DATA CONFIDENCE	007	7998788789	9981763279	9884498189	9889837887	7212048999	9715399958				

	91	L5	101	L6	ASL2	131	L8	141
A1) X-ray	TAWTDDQTAQ	ILNWIKQEIN	LPVALAVVTH	AHQDKMGGMD	ALHAAGIATY	ANALSNQLAP		
A2) DATA SEQUENCE	TAWTDDQTAQ	ILNWIKQEIN	LPVALAVVTH	AHQDKMGGMD	ALHAAGIATY	ANALSNQLAP		
A2) DATA PREDICTED_SS	LLLLHHHHHH	HHHHHHHHHL	LLLLEEEXXX	XXXXXXXXXX	HHHHLLLLLE	ELHHHHHHHX		
A2) DATA CONFIDENC	7636799999	9999998616	8551598000	0000000000	9997287527	6299888510		

	151	L9	161	L10	171	L11	181	ASL3	191	L13
A1) X-ray	QEGMVAHQHS	LTFAANGWVE	PATAPNFGPL	KVFYPGPGHT	SDNITVIGIDG	TDIAFGGCLI				
A2) DATA SEQUENCE	QEGMVAHQHS	LTFAANGWVE	PATAPNFGPL	KVFYPGPGHT	SDNITVIGIDG	TDIAFGGCLI				
A2) DATA PREDICTED_SS	XXXLLLLLLE	EEELLLLLLL	HLLLLLLLLL	EEEEELLLL	LLLLEEELLL	LLLLEEEXLL				
A2) DATA CONFIDENCE	0000178836	7525168778	3429987987	3995698489	8786596388	7737960777				

	211	ASL4	221	231	L15	ASL5	261
A1) X-ray	KDSKAKSLGN	LGADATHEHYA	ASARAFGAAF	PKASMIIVMESH	SAPDSRAAIT	HTARMADKLR	
A2) DATA SEQUENCE	KDSKAKSLGN	LGADATHEHYA	ASARAFGAAF	PKASMIIVMESH	SAPDSRAAIT	HTARMADKLR	
A2) DATA PREDICTED_SS	LLLLLLLLLL	LLLLLHHHHH	HHHHHHHHHL	LLLLEEELLL	LLLLLHHHHH	HHHHHHHHHH	
A2) DATA CONFIDENCE	7832677788	5679858999	9999998618	9784699575	8884779999	9999999999	

	271
A1) X-ray	LEHHHHH
A2) DATA SEQUENCE	LEHHHHH
A2) DATA PREDICTED_SS	HXXXXXX
A2) DATA CONFIDENCE	6000000

### b) NDM-1 in presence of 2 molar equivalents of Zn<sup>2+</sup>

	28	31	41	51	61	71	81
B1) X-ray	MGE	IRPTIGQQME	TGDQRFGDLV	FRQLAPNVWQ	HTSYLDMPGF	GAVASNGLIV	RDGGRVLVVD
B2) Yao et al	MGE	IRPTIGQQME	TGDQRFGDLV	FRQLAPNVWQ	HTSYLDMPGF	GAVASNGLIV	RDGGRVLVVD
B3) DATA SEQUENCE	MGE	IRPTIGQQME	TGDQRFGDLV	FRQLAPNVWQ	HTSYLDMPGF	GAVASNGLIV	RDGGRVLVVD
B3) DATA PREDICTED_SS	XXX	LLLLLLLLLL	LLLLLEELLEE	EEELLXEEE	EEEEELLLL	LEEEEEEEEE	EEELLEEEL
B3) DATA CONFIDENCE	000	7999799889	9994660279	8861700689	8789845455	4325777999	9844089968

	91	101	111	121	131	141
B1) X-ray	TAWTDDQTAQ	ILNWIKQEIN	LPVALAVVTH	AHQDKMGGMD	ALHAAGIATY	ANALSNQLAP
B2) Yao et al	TAWTDDQTAQ	ILNWIKQEIN	LPVALAVVTH	AHQDKMGGMD	ALHAAGIATY	ANALSNQLAP
B3) DATA SEQUENCE	TAWTDDQTAQ	ILNWIKQEIN	LPVALAVVTH	AHQDKMGGMD	ALHAAGIATY	ANALSNQLAP
B3) DATA PREDICTED_SS	LLLLHHHHHH	HHHHHHHHHL	LLLLEEELLL	LLLLXXLLHH	HHHHLLLLLE	EEHHHHHHHH
B3) DATA CONFIDENCE	9998699999	9999996159	9861698275	8587009829	9984597357	6288889998

	151	161	171	181	191	201
B1) X-ray	QEGMVAHQHS	LTFAANGWVE	PATAPNFGPL	KVFYPGPGHT	SDNITVIGIDG	TDIAFGGCLI
B2) Yao et al	QEGMVAHQHS	LTFAANGWVE	PATAPNFGPL	KVFYPGPGHT	SDNITVIGIDG	TDIAFGGCLI
B3) DATA SEQUENCE	QEGMVAHQHS	LTFAANGWVE	PATAPNFGPL	KVFYPGPGHT	SDNITVIGIDG	TDIAFGGCLI
B3) DATA PREDICTED_SS	HLLEELLLL	EEELLLLLLL	LLLLLLLLLL	EEEEELLLL	LLLLLEELLL	LEEEEEELLL
B3) DATA CONFIDENCE	4681279947	8635799778	6379999987	4986509899	9996586288	7618884466

	211	221	231	241	251	261
B1) X-ray	KDSKAKSLGN	LGADATHEHYA	ASARAFGAAF	PKASMIIVMESH	SAPDSRAAIT	HTARMADKLR
B2) Yao et al	KDSKAKSLGN	LGADATHEHYA	ASARAFGAAF	PKASMIIVMESH	SAPDSRAAIT	HTARMADKLR
B3) DATA SEQUENCE	KDSKAKSLGN	LGADATHEHYA	ASARAFGAAF	PKASMIIVMESH	SAPDSRAAIT	HTARMADKLR
B3) DATA PREDICTED_SS	LLLLLLLLLL	LLLLLHHHHH	HHHHHHHHHL	LLLLEEELLL	LLLLLHHHHH	HHHHHHHHHH
B3) DATA CONFIDENCE	7988987670	5899951599	9999985228	9883799678	9996779999	9999999983

	271
B1) X-ray	LEHHHHH
B2) Yao et al	LEHHHHH
B3) DATA SEQUENCE	LEHHHHH:
B3) DATA PREDICTED_SS	XXXXXXX
B3) DATA CONFIDENCE	0000000

**Figure S6.** Comparison of the NDM-1 secondary structures predictions derived from its backbone NMR chemical shifts by TALOS+, with those observed in the X-ray structures and the Yao et al results (1) (a) in absence (PDB ID: 3RKK, 3SBL, 3RKJ and 3PG4) and (b) in presence of zinc (PDB ID: 4TZE, 4TZF, 3SPU and 4TYF). The red and yellow boxes highlight the helix and strand predictions, the purple boxes the residues that belong to  $\alpha$ -helices in several X-ray structures (PDB ID: 4TZE and 4TZF) and not in others (PDB ID: 3SPU and 4TYF) and the green boxes the residues that belong to  $\beta$ -strands in several X-ray structures (PDB ID: 3SPU) and not in others (PDB ID: 4TZE, 4TYF and 4TZF). DATA PREDICTED\_SS and DATA CONFIDENCE are our results from TALOS+. H, E and L are for Helix, Strand and Coil predictions. X indicate the amino acids for which no resonance has been assigned in our NMR spectra and grey boxes those for which the amide proton cannot be assigned, and the blue boxes the resonances that could not be assigned by Yao et al. (1). The loops are highlighted in (a) (L1 to L16 in red) with the residues underlined. L3 corresponds to ASL1, L7 to ASL2, L12 to ASL3, L14 to ASL4 and L16 to ASL5.

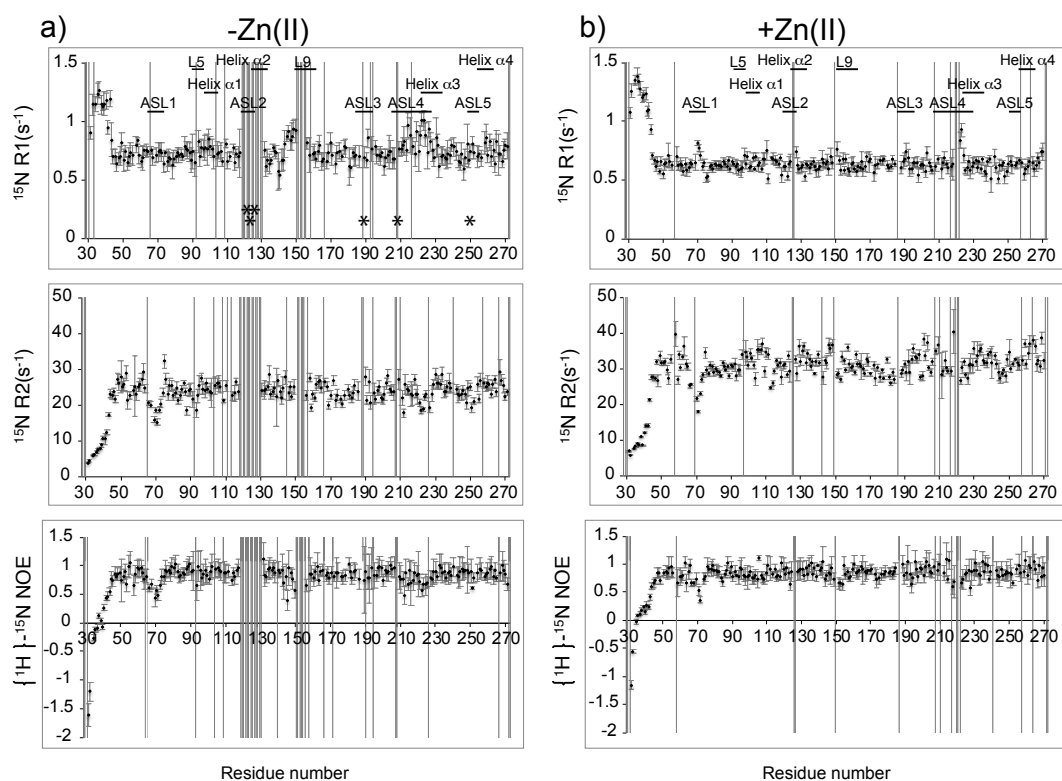


**Figure S7.** (a) NMR relaxation parameters of NDM-1.  $^{15}\text{N}$  R1, R2 relaxation and heteronuclear  $\{^1\text{H}\}$ - $^{15}\text{N}$  NOE parameters obtained for NDM-1 in the absence of Zn(II) (phosphate buffer 50 mM, pH 7.0 and 150 mM NaCl), (b) in the presence of 2 molar equivalents of Zn(II) (0.1 mM bis tris, pH 7.0, 150 mM NaCl), at 600 MHz  $^1\text{H}$  and 25°C. The light grey bars represent either the unassigned residues or the residues for which the R1, R2 and  $\{^1\text{H}\}$ - $^{15}\text{N}$  NOE values could not be obtained due to superimposition of several cross-peaks. \* indicate the residues implicated in the binding of Zn(II).

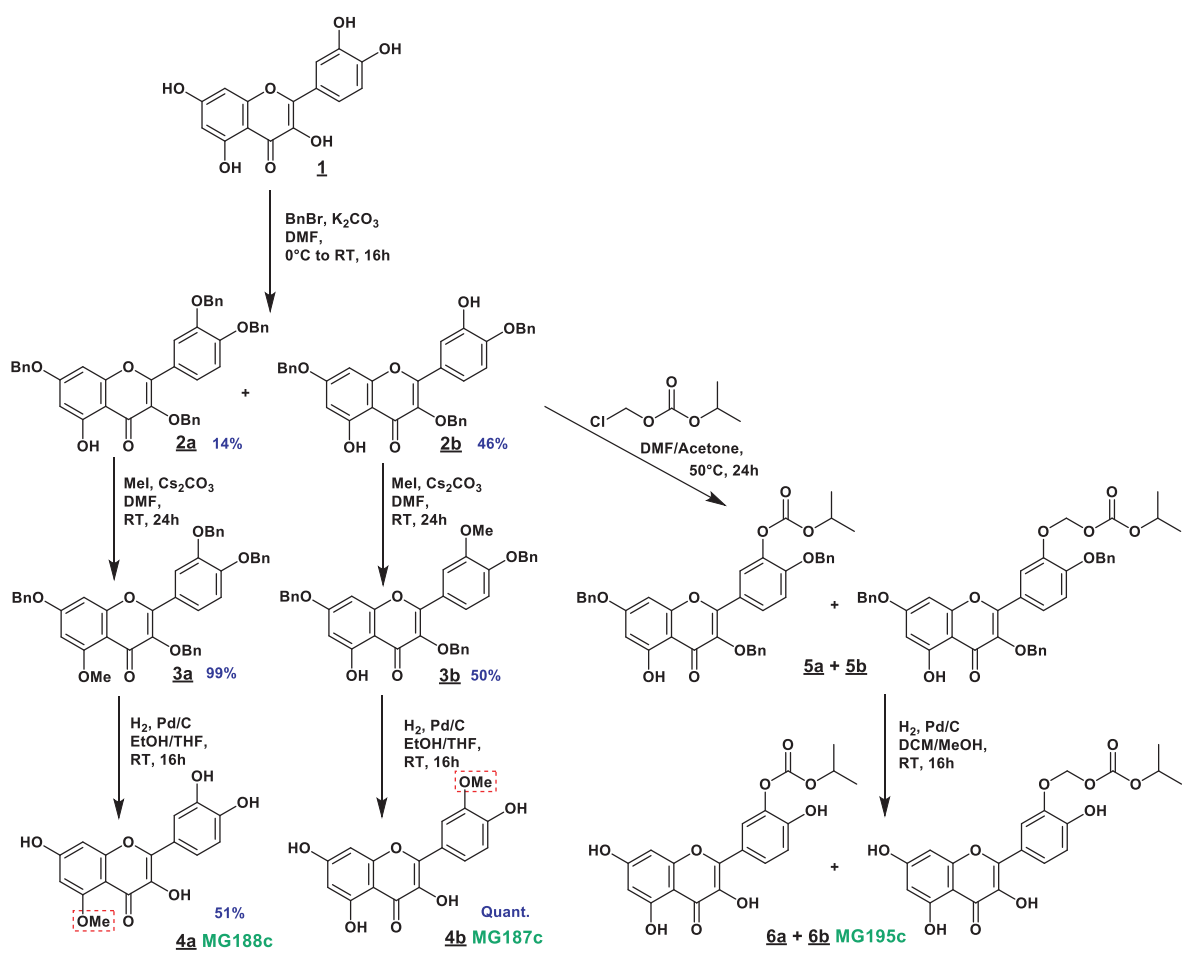


**Figure S8.** Synthetic route to compounds MG188c (**4a**), MG187c (**4b**) and MG195c (**6a + 6b**)

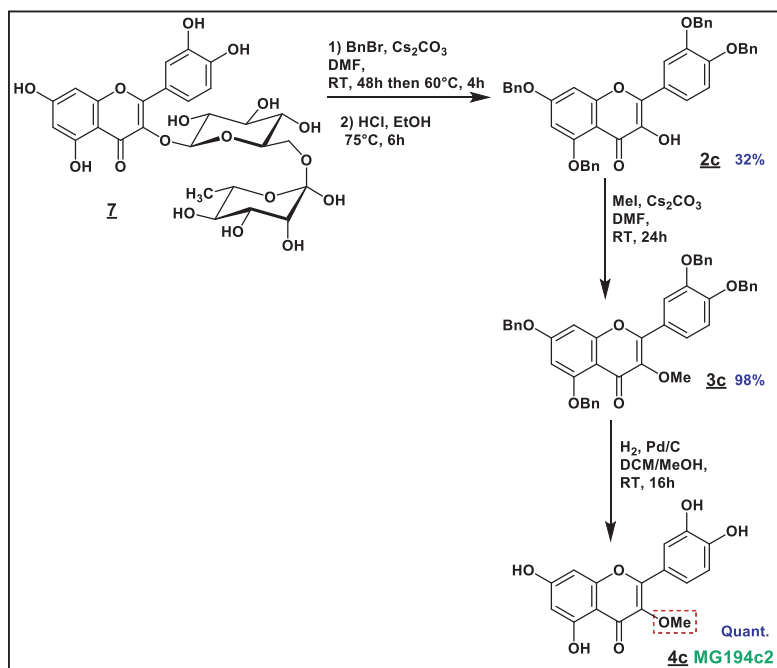


**Figure S9.** Synthetic route to compound MG194c2 (**4c**)

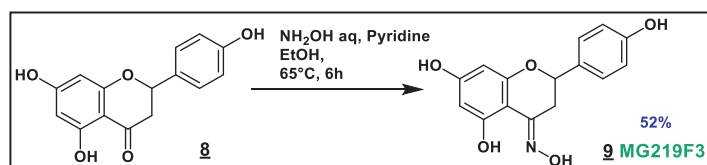


**Figure S10.** Synthetic route to compound MG219F3 (**9**)

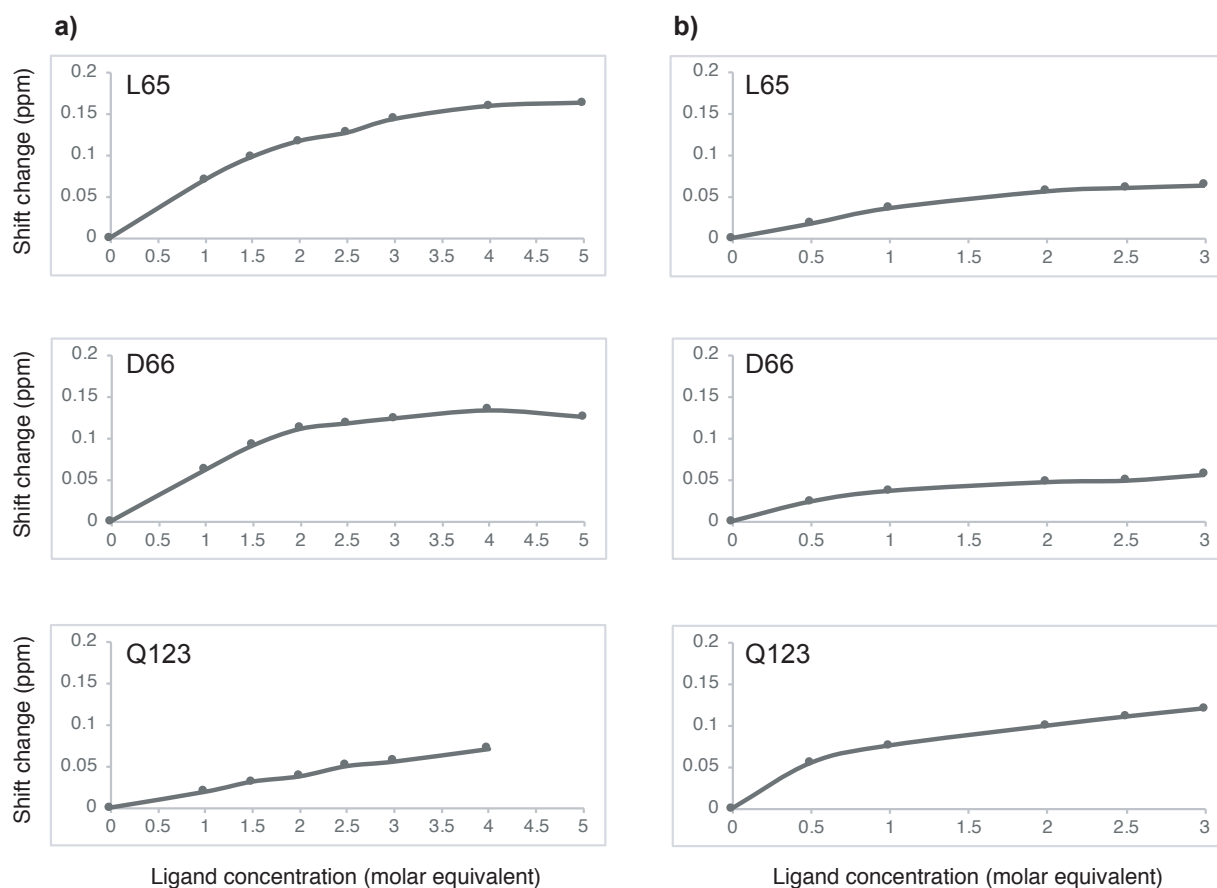


**Figure S11.** Experimental NMR titration curves, of amide proton and nitrogen for three residues of di-Zn(II) NDM-1 (L65, D66, Q123), by (a) morin and (b) myricetin. The protein, concentrated to 320  $\mu$ M, was solubilized in 0.1 mM Bis-Tris buffer pH 7, supplemented by 150 mM NaCl. The flavonols were dissolved in 100% DMSO at a concentration of 20 mM. We titrated 320  $\mu$ M of NDM-1 with the flavonols (0 to 4 molar equivalents for morin and 0 to 3 molar equivalents for myricetin). Each HSQC spectrum was collected with 8 scans per increment with spectral widths of 9.6 kHz for  $^1$ H and 3.2 kHz for  $^{15}$ N as well as 256 data points in the indirect dimension. The experiments used the 3-9-19 watergate sequence (2) for water suppression.

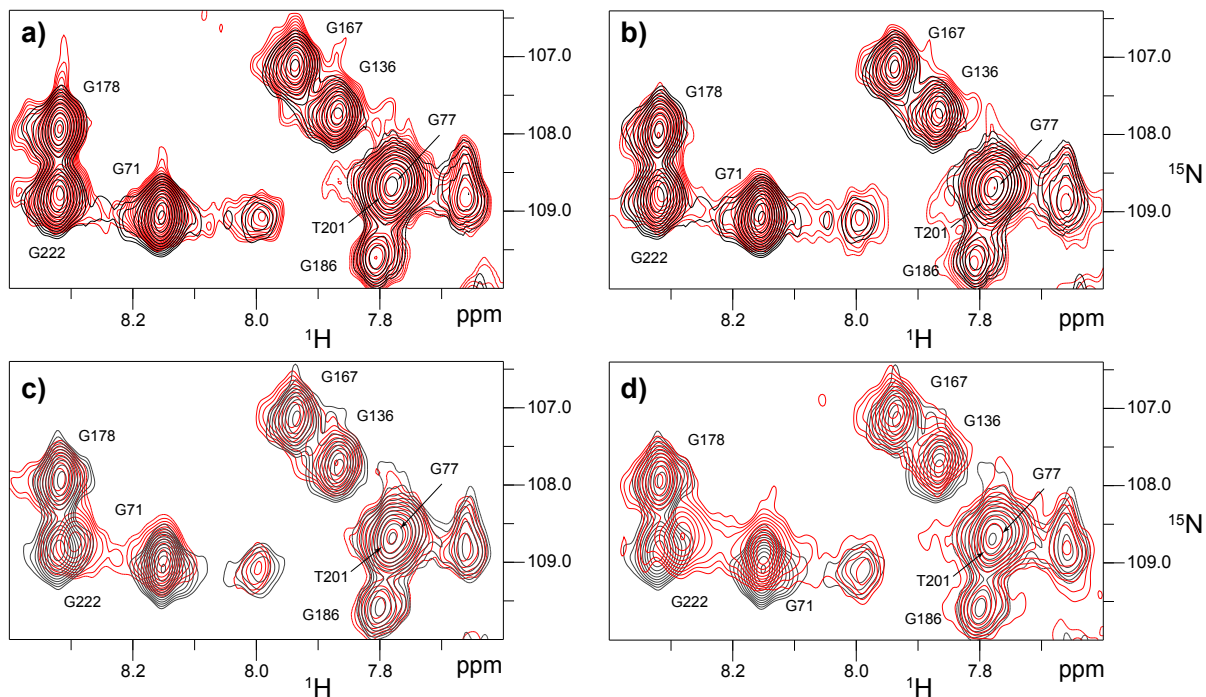


**Figure S12.** Selected regions of the  $^1\text{H}$ - $^{15}\text{N}$  HSQC spectra probing the NDM-1:flavonol interactions in absence of Zn(II). Panels a) and b) show that addition of DMSO (black in absence of DMSO and red in presence of the quantity of DMSO corresponding to that was added to have 2 and 4 molar equivalents of flavonol relative to the NDM-1 concentration: 5.72 and 11.44  $\mu\text{l}$  DMSO respectively) do not induce significant chemical shift variations of the NDM-1 resonances. Titrations of NDM-1 (in black in absence of flavonol) by 2 molar equivalent (c) and 4 molar equivalents (d) (in red) of morin showing the influence of the flavonols on several NDM-1 resonances. The spectra were recorded at 20  $^\circ\text{C}$  and 800 MHz  $^1\text{H}$  frequency on a sample buffer containing 0.1 mM bis tris (pH 7.0) and 150 mM NaCl with increasing concentrations of DMSO as the ligand is incremented. The concentration of NDM-1 is 357  $\mu\text{M}$ .

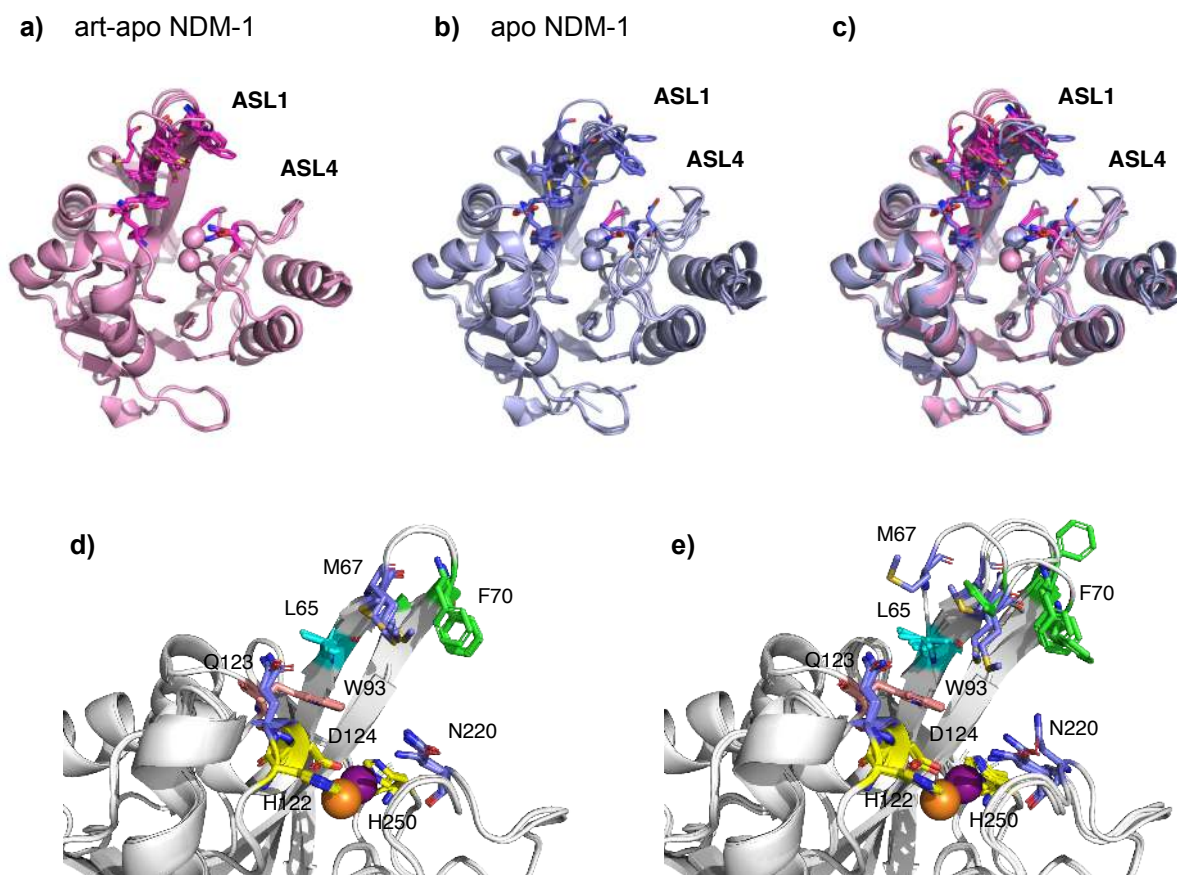
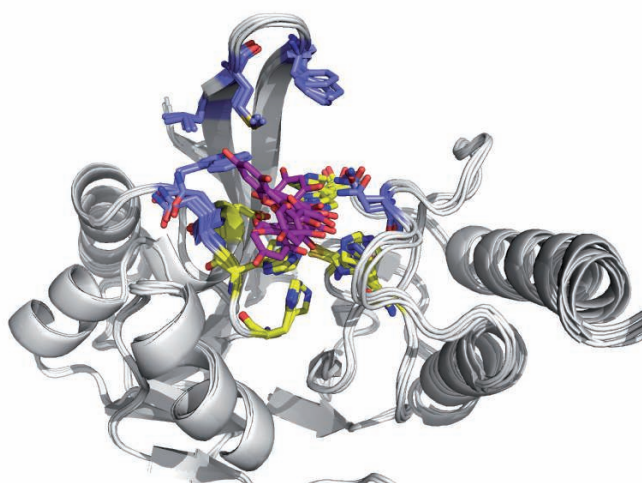
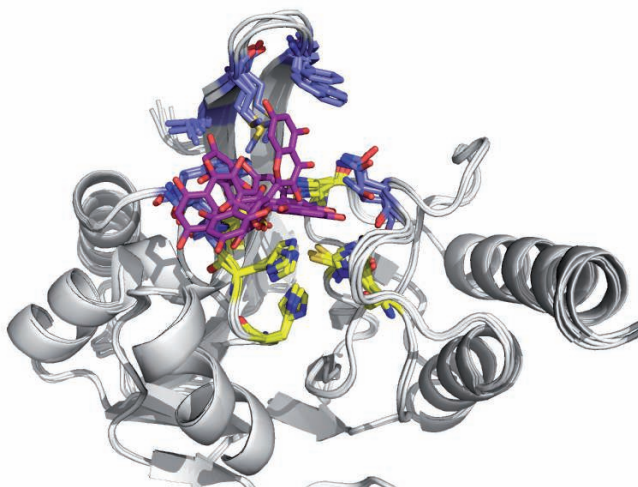


**Figure S13.** NDM-1 ASL1 and ASL4 loop flexibilities. (a) Superimposition of ten art-apo NDM-1 (PDB: 4EXS, 4EY2, 4EYL, 4RL0, 4RL2, 4EYB, 4EYF, 4RBS, 4RAM, 4HL2) in pink. (b) Superimposition of five apo-NDM-1 (PDB: 3S0Z, 3SPU, 4TYF, 4TZE, 4TZF) in blue. (c) Superimposition of the ten art-apo NDM-1 (PDB: 4EY2, 4EYL, 4RL0, 4RL2, 4EYB, 4EYF, 4RBS, 4RAM, 4HL2) in pink and the five apo-NDM-1 (PDB: 3S0Z, 3SPU, 4TYF, 4TZE, 4TZF) in blue used for molecular-docking simulations in the data-driven program HADDOCK, showing the flexibility of the ASL1 and ASL4 loops relative to the global structure of NDM-1. (d) Superimposition of the art-apo NDM-1 structures with the Zn1-Zn2 distances ranging from 4.5 to 4.6 Å (PDB: 4EY2, 4EYB, 4HL2, 4RL2, 4EYF) in the starting structures. (e) Superimposition of the art-apo NDM-1 structures with the Zn1-Zn2 distances ranging from 3.1 to 4.1 Å (PDB: 4EXS, 4EYL, 4RAM, 4RBS, 4RL0) in the starting structures. The superimposition were done on the 45-271 backbone atoms of the PDB:4EY2 structure. The residues implicated in the flavonol recognitions are highlighted by sticks.

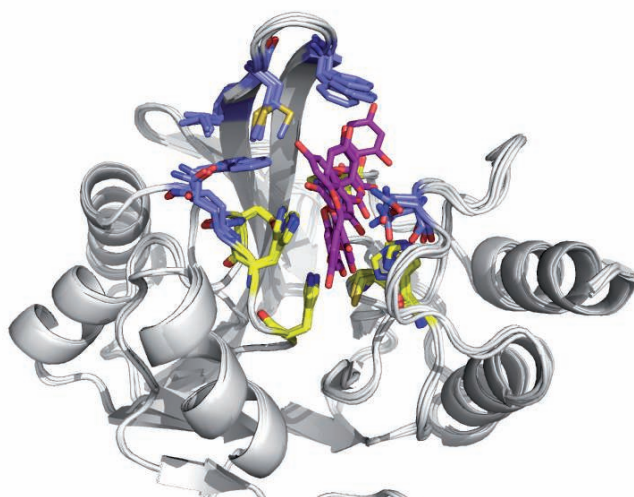
3PG4: cluster 4 (27/385 structures)



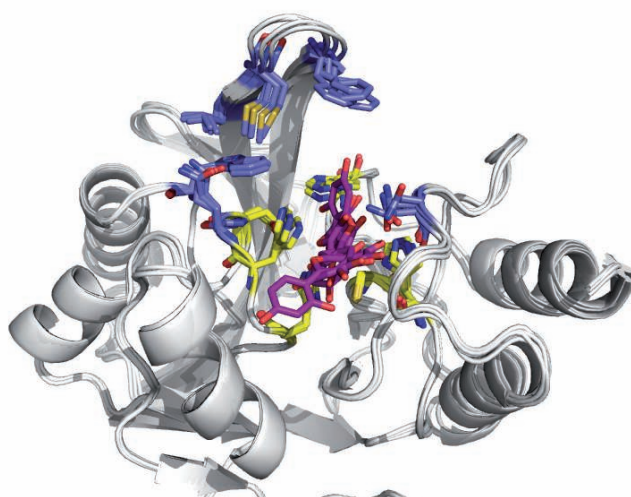
3PG4: cluster 2 (68/385 structures)



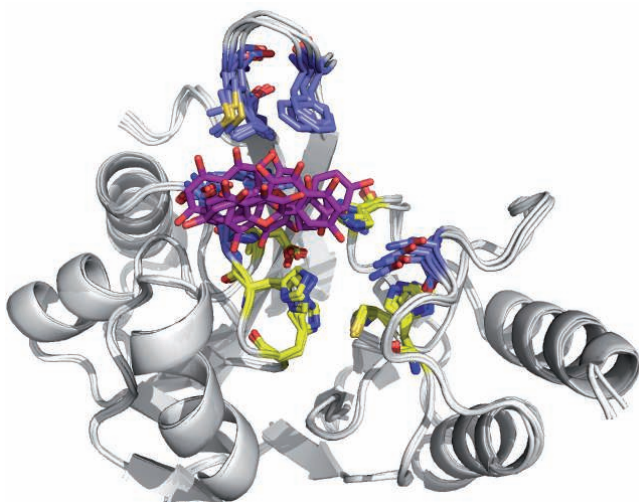
3SBL: cluster 2 (118/389 structures)



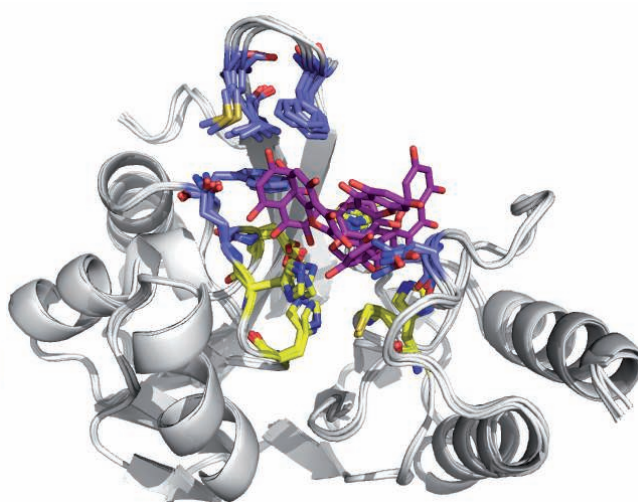
3SBL: cluster 5 (14/389 structures)



3RKJ: cluster 3 (36/392 structures)



3RKJ: cluster 2 (85/392 structures)



3RKK: cluster 2 (25/173 structures)

3RKK: cluster 1 (36/173 structures)

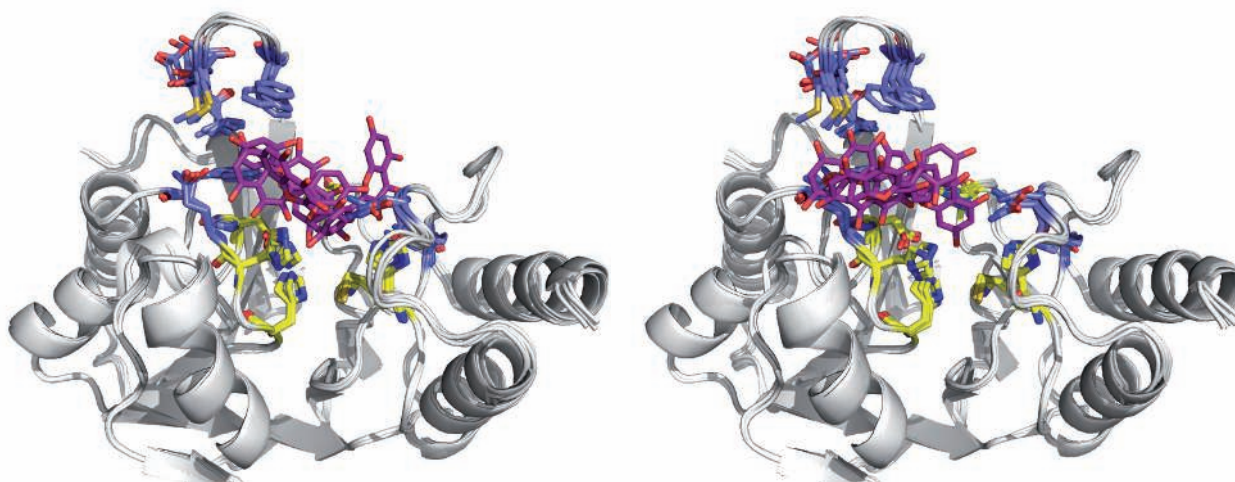
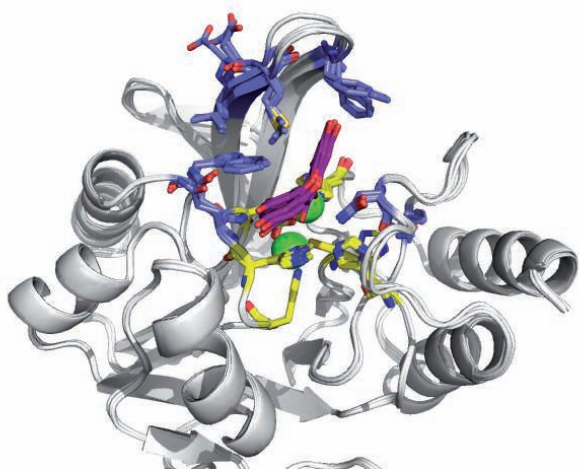


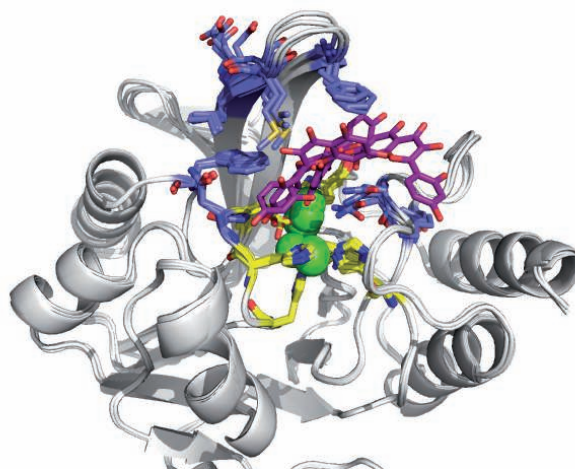
**Figure S14** Models of the NDM-1/morin complexes generated using the HADDOCK webserver with the four metal-free apo crystal structures of NDM-1 (PDB: 3PG4, 3SBL, 3RKJ, 3RKK ). Only the two top clusters are shown: clusters 4 and 2 for 4PG4, clusters 2 and 5 for 3SBL, clusters 3 and 2 for 3RKJ and clusters 2 and 1 for 3RKK. The top clusters are the most reliable according to HADDOCK. The statistics of the all clusters are shown in Table S4. The Fraction of native contacts (FCC) clustering were used to clustered the structures. The number of structures in each cluster over the HADDOCK clustered structures (which represent the number of the water-refined HADDOCK generated structures) is written in brackets.

The L65, M67, F70, W93, H122, Q123, D124, N220, H250 NDM-1 residues were defined as “passive” residues and the flavonol as “active” residue (as define in the HADDOCK software).

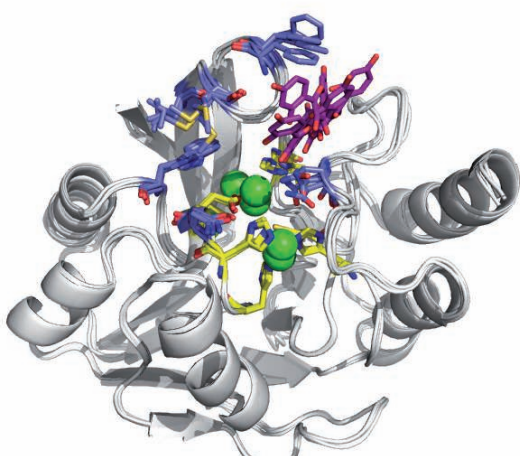
4TYF: cluster 3 (54/390 structures)



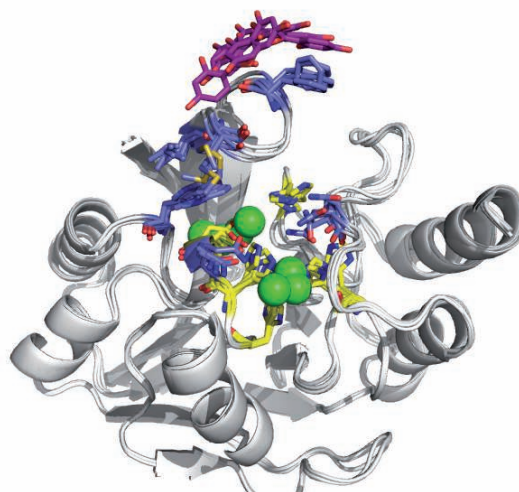
4TYF: cluster 1 (212/390 structures)



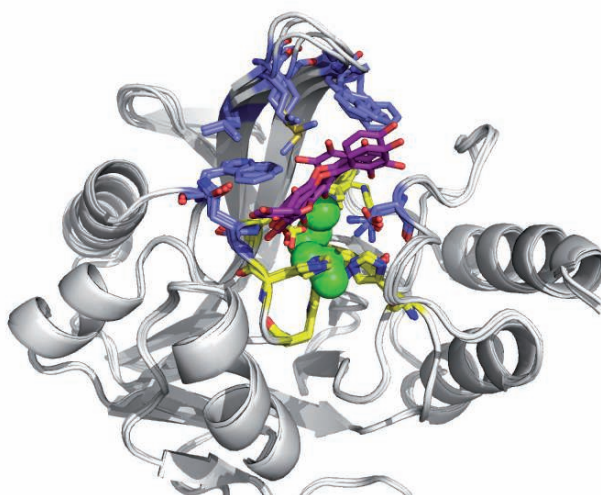
3S0Z: cluster 2 (50/393 structures)



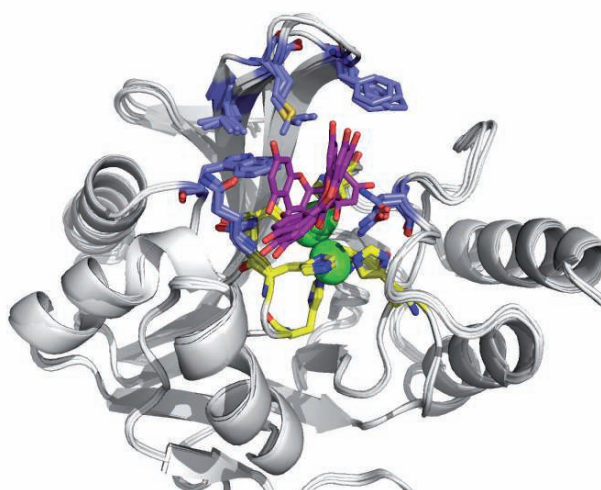
3S0Z: cluster 1 (336/393 structures)



4TZF: cluster 2 (65/398 structures)



4TZF: cluster 7 (9/398 structures)



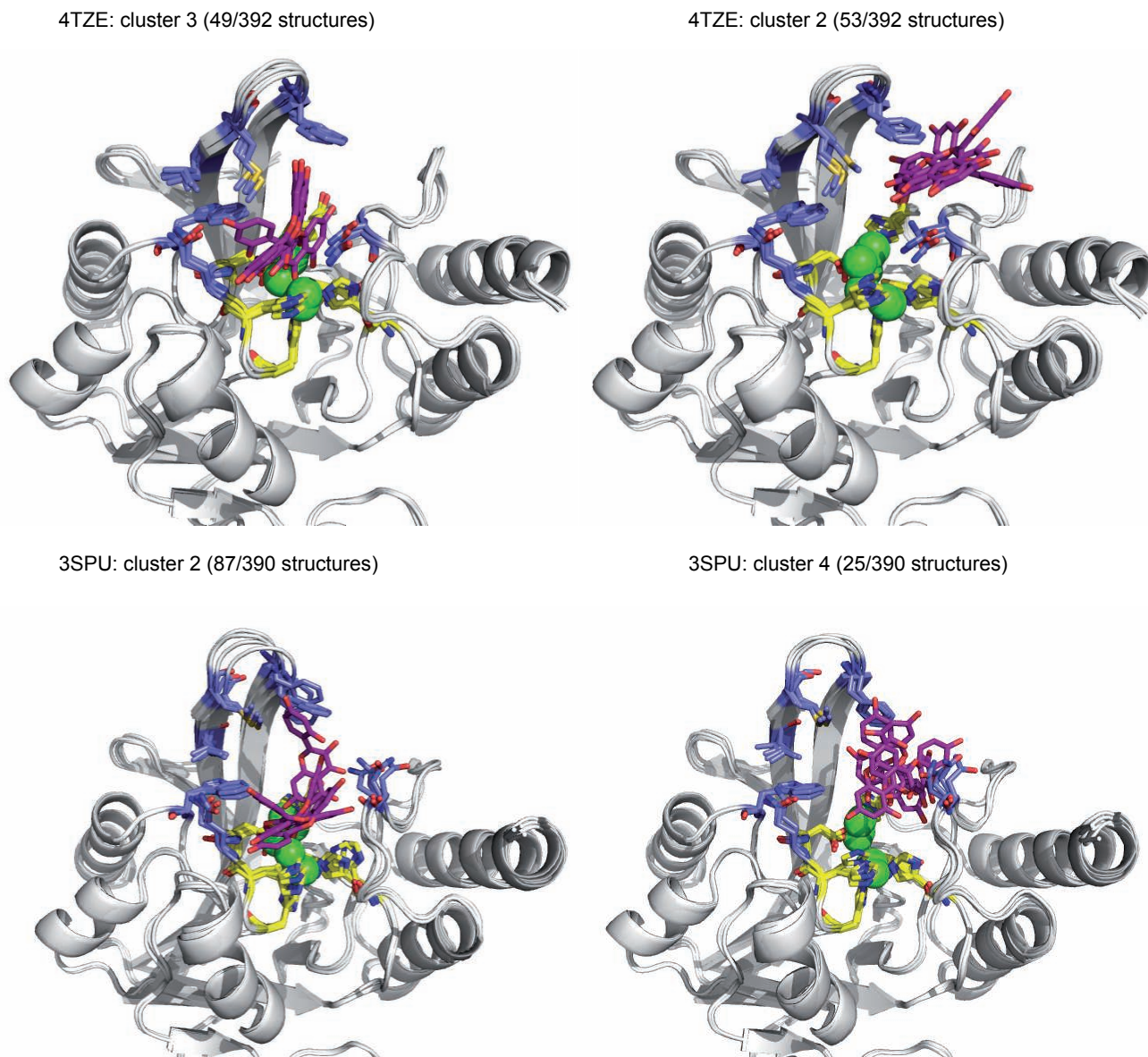
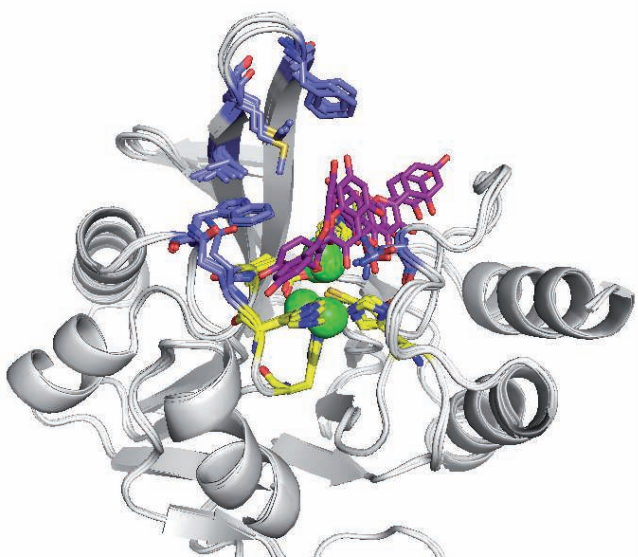


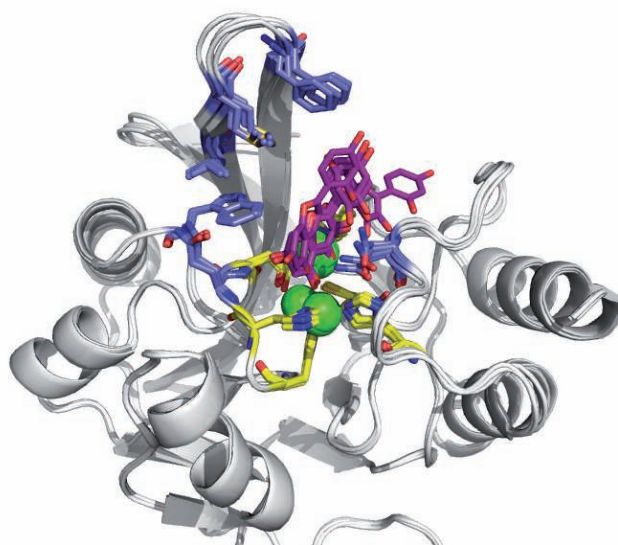
**Figure S15.** Models of the NDM-1/morin complexes generated using the HADDOCK webserver with five apo crystal structure of NDM-1 (PDB:4TYF, 3S0Z, 4TZF, 4TZE, 3SPU). The L65, M67, F70, W93, H122, Q123, D124, N220, H250 NDM-1 residues were defined as “passive” residues and the flavonol as “active” residue (as defined in the HADDOCK software).

Only the two top clusters are shown: clusters 3 and 1 for 4TYF, clusters 2 and 1 for 3S0Z, clusters 2 and 7 for 4TZF, clusters 3 and 2 for 4TZE and clusters 2 and 4 for 3SPU. The top clusters are the most reliable according to HADDOCK. The statistics of the all clusters are shown in Table S5. The Fraction of native contacts (FCC) clustering were used to clustered the structures. The number of structures in each cluster over the HADDOCK clustered structures (which represent the number of the water-refined HADDOCK generated structures) is written in brackets.

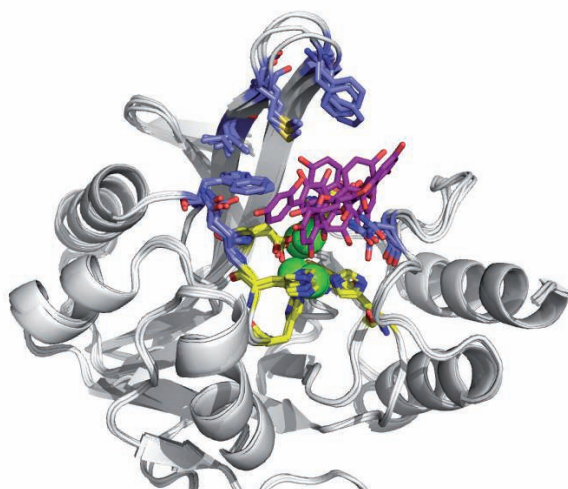
4EY2: cluster 2 (130/392 structures)



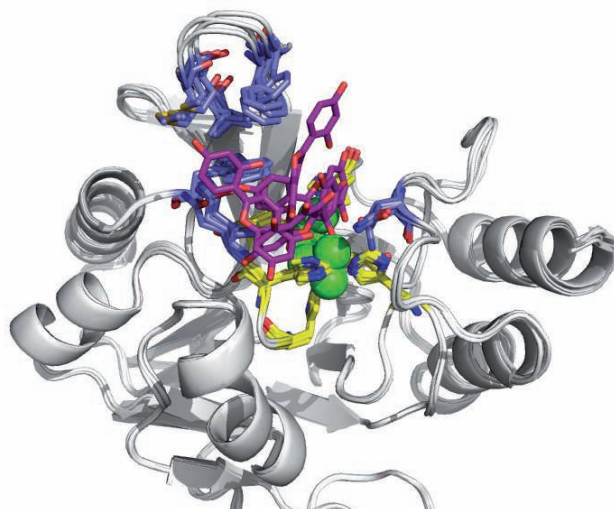
4EYB: cluster 2 (83/389 structures)



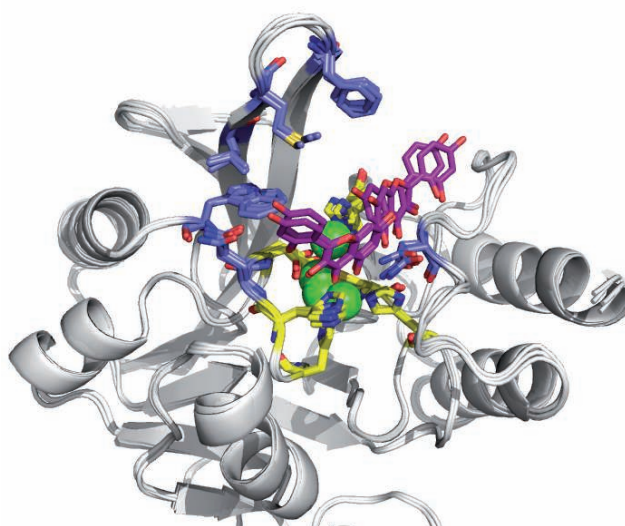
4EYF: cluster 2 (96/393 structures)



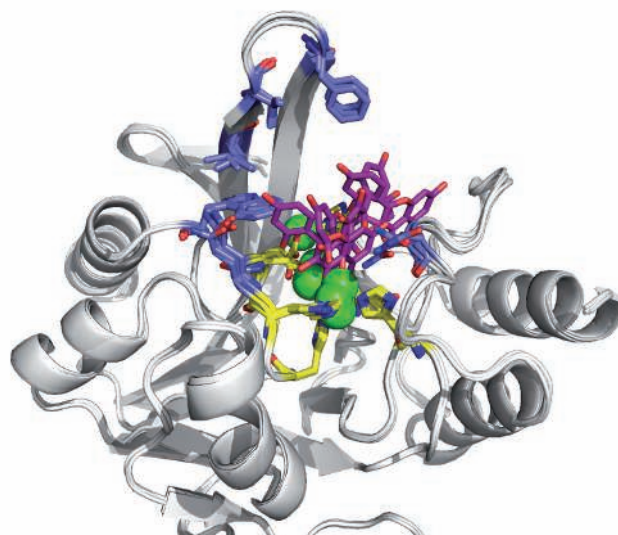
4EYL: cluster 2 (83/390 structures)



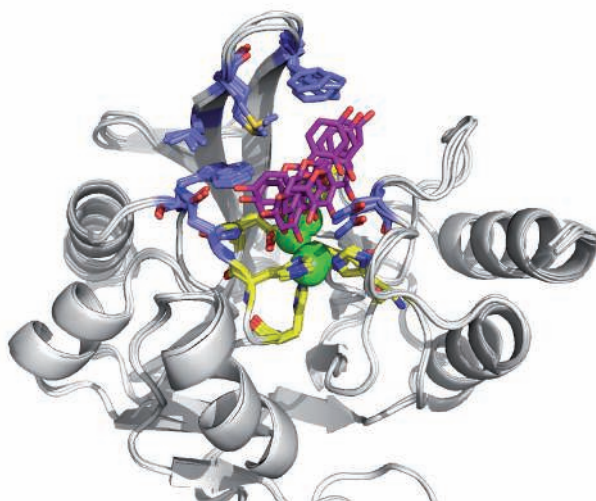
4HL2: cluster 2 (94/387 structures)



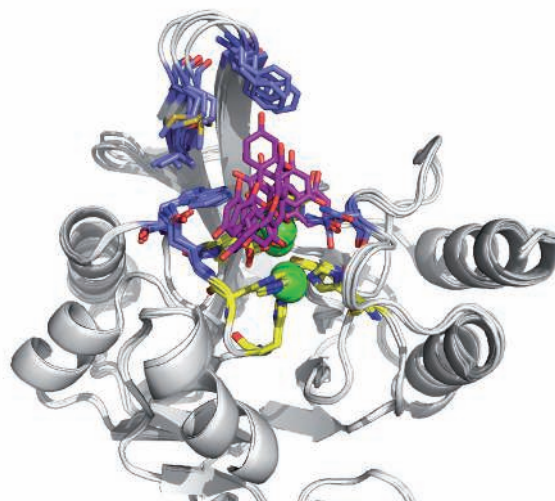
4RAM: cluster 2 (142/390 structures)



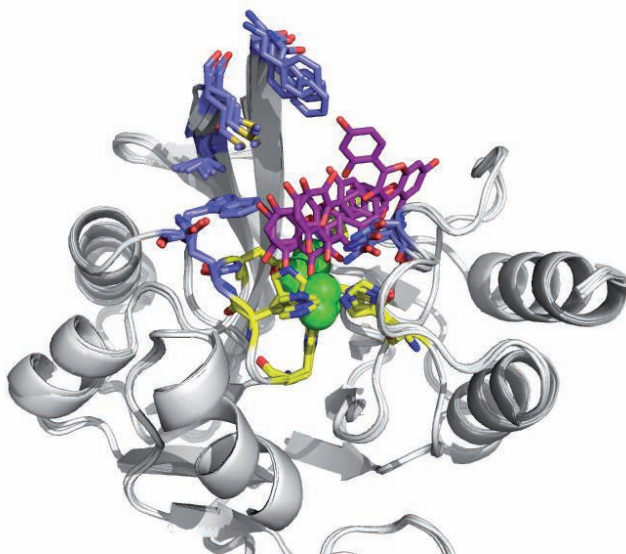
4RBS: cluster 1 (180/395 structures)



4RL2: cluster 2 (115/398 structures)

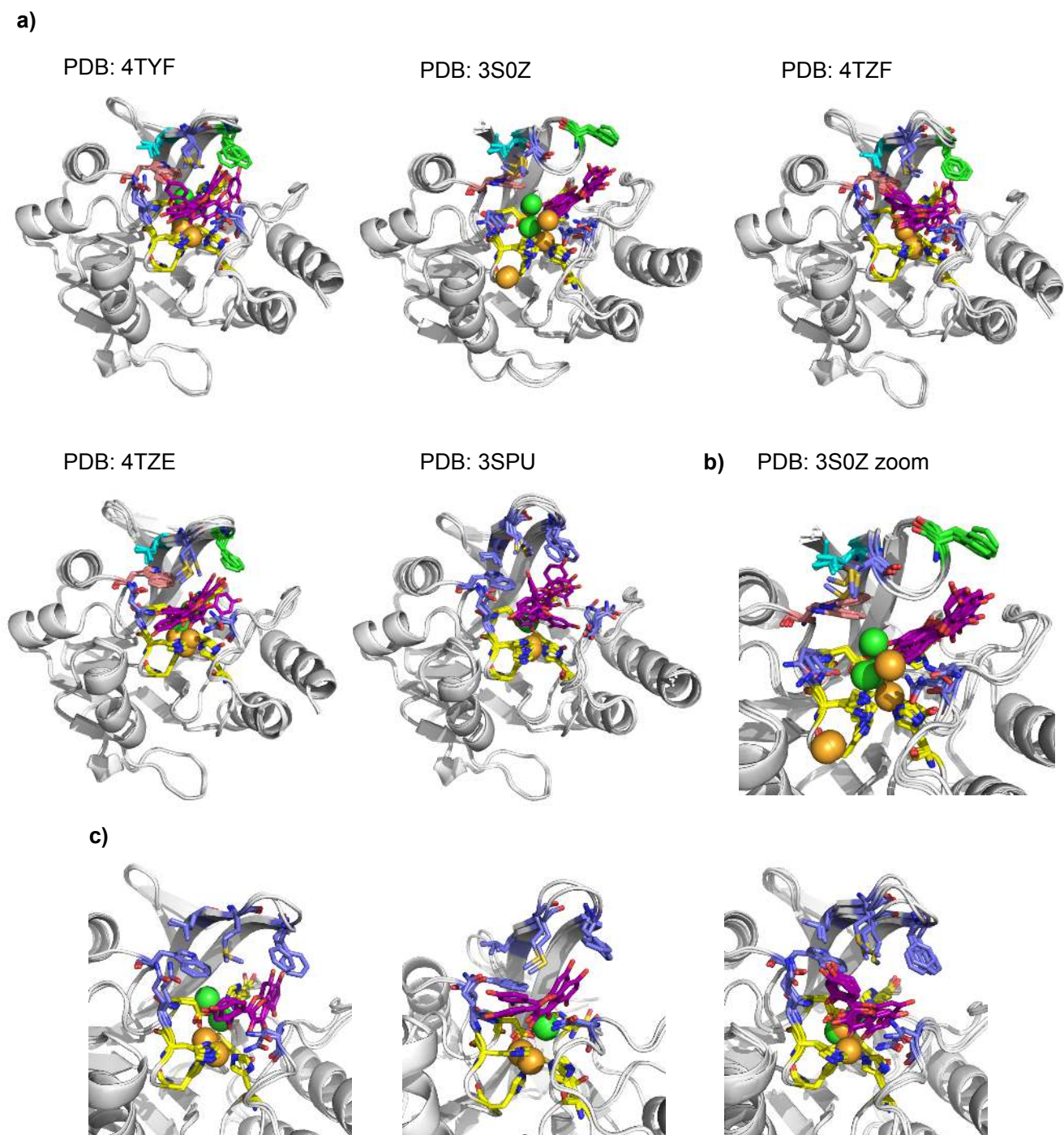


4RL0: cluster 2 (67/394 structures)

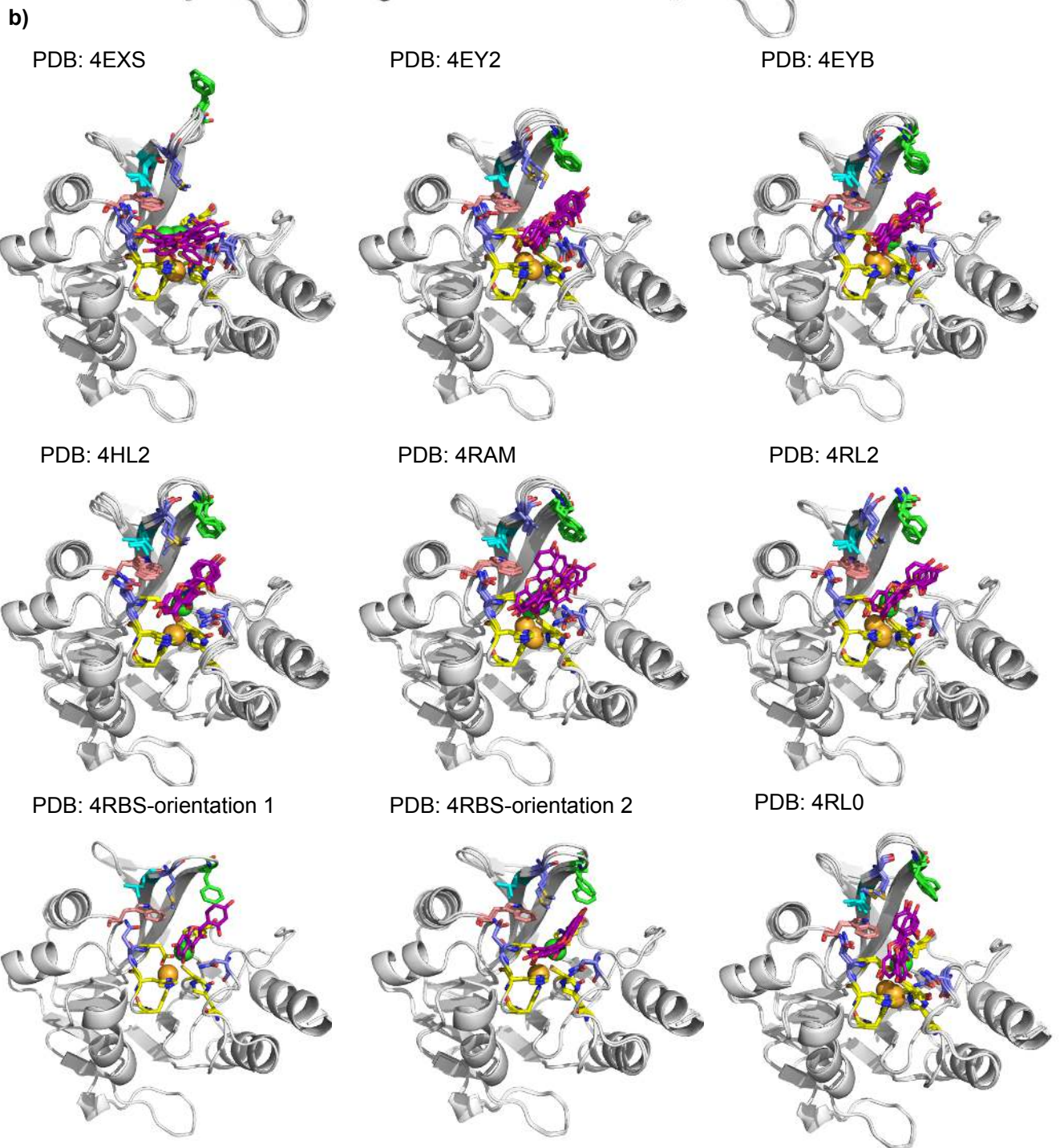
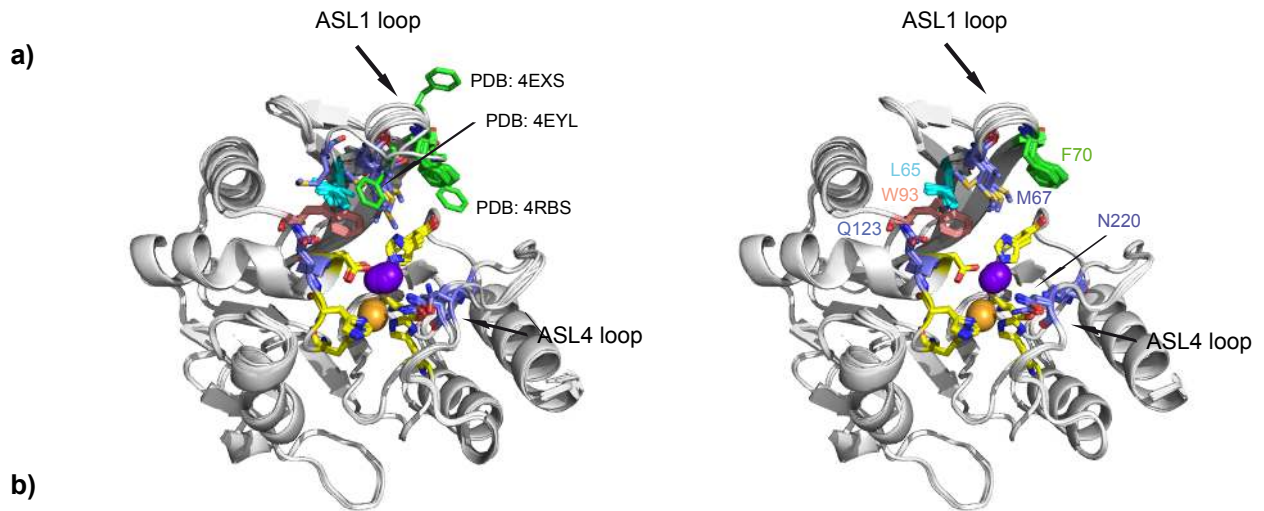


**Figure S16.** Models of the NDM-1/morin complexes generated using the HADDOCK webserver with ten crystal structure of NDM-1 in complex with a ligand. (PDB: 4EXS, 4EY2, 4EYB, 4EYF, 4EYL, 4HL2, 4RAM, 4RBS, 4RL2, 4RL0). These structures were used for docking after removing of the ligand localized in the active site of the NDM-1 crystallographic structures. They were named “artificial apo” (art-apo) NDM-1 structures. The L65, M67, F70, W93, H122, Q123, D124, N220, H250 NDM-1 residues were defined as “passive” residues and the flavonol as “active” residue (as defined in the HADDOCK software).

Only the top clusters are shown: clusters 2 for 4EY2, 4EYB, 4EYF, 4EYL, 4HL2, 4RAM, 4RL2, 4RL0 and cluster1 for 4RBS. The top clusters are the most reliable according to HADDOCK. The statistics of the all clusters are shown in Table S6. The Fraction of native contacts (FCC) clustering were used to clustered the structures. The number of structures in each cluster over the HADDOCK clustered structures (which represent the number of the water-refined HADDOCK generated structures) is written in brackets.



**Figure S17.** Models of the NDM-1/morin complexes generated using the HADDOCK webserver using five apo crystal structure of NDM-1 (PDB: 4TYF, 3S0Z, 4TZF, 4TZE, 3SPU). (a) Only the top clusters are shown: clusters 2 for 4TYF, 4TZF, clusters 1 for 3S0Z, 4TZE and cluster 3 for 3SPU. The top clusters are the most reliable according to HADDOCK. The ranking of the clusters is based on the average score of the top 4 members of each cluster. The «ligand interface RMSD» was used to clustered the structures. The statistics of the all clusters are shown in Table S7. The L65, M67, F70, W93, H122, Q123, D124, N220, H250 NDM-1 residues were defined as “passive” residues, the two Zn(II) ions and the flavonol as “active” residues (as define in the HADDOCK software). (b) The morin target the Zn(II) ions through polar contacts and is localized in the active site except for PDB: 3S0Z for which the morin is partially outside the active NDM-1 site. (c) Zoom on several other observed orientations of the morin in the active site of NDM-1.



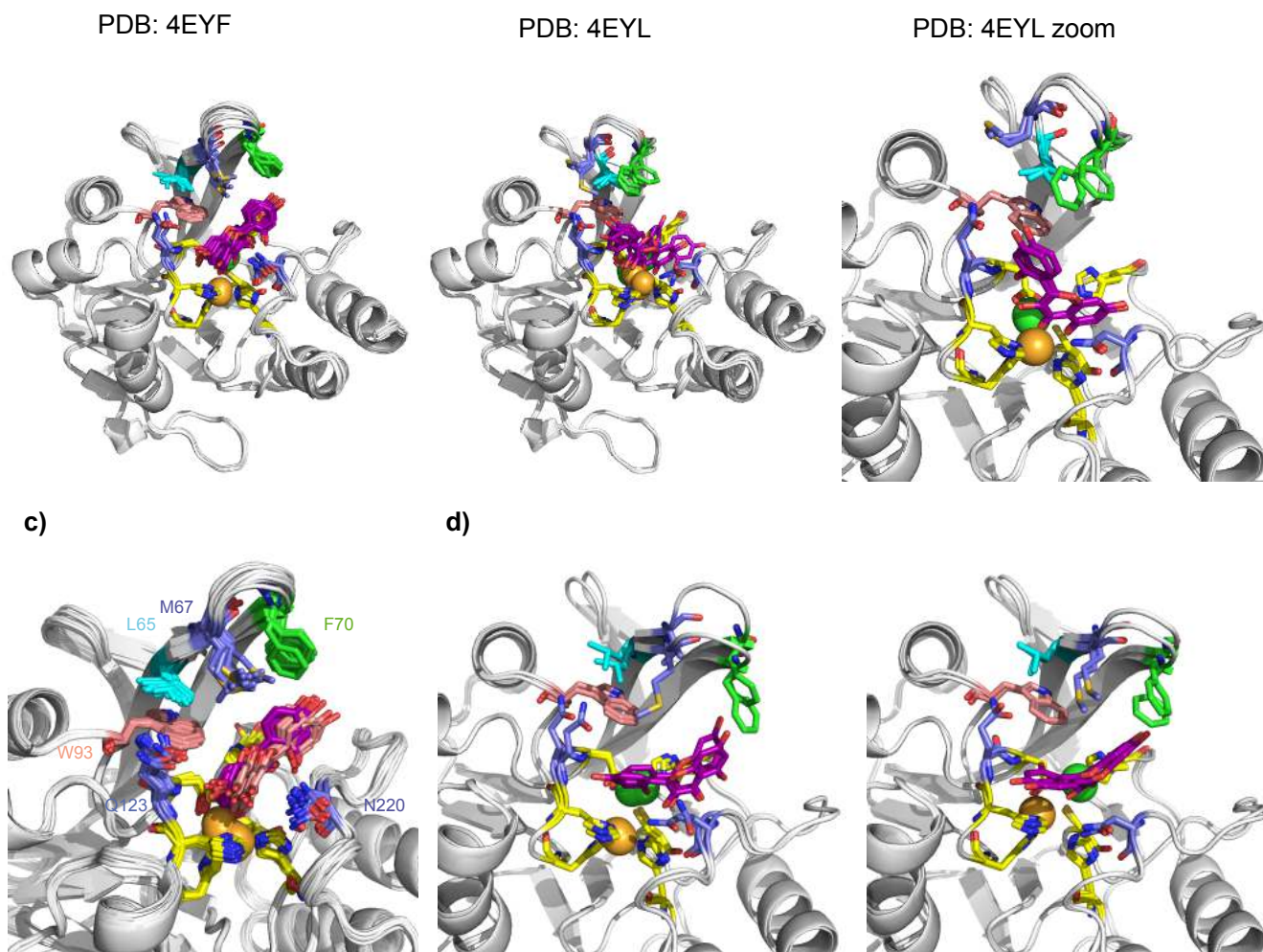


**Figure S18.** Models of the NDM-1/morin complexes generated using the HADDOCK webserver with ten crystal structures of NDM-1 in complex with a ligand. (PDB: 4EXS, 4EY2, 4EYB, 4EYF, 4EYL, 4HL2, 4RAM, 4RBS, 4RL2, 4RL0). (a) Superimposition of the ten crystal structures of NDM-1 used for the docking, showing the flexibility of the ASL1 loop (on the left). On the right only the seven most similar structures are represented (PDB: 4EY2, 4EYB, 4EYF, 4HL2, 4RAM, 4RL2, 4RL0). All these structures were used for docking after removing of the ligand localized in the active site of the NDM-1 crystallographic structures. The residues defined as «passive» during the docking simulations are highlighted (L65 in light blue, M67, Q123, N220 in blue, W93 in pink, F70 in green) as well as the Zn(II) ligands (H120, H122, D124, H189, C208 and H250 in yellow). (b) The best generated models during the docking simulations, were selected on the basis of the HADDOCK score and shown: clusters 1 for 4EXS, 4EYB, 4EYL, 4HL2, 4RBS, 4RL2 and cluters 2 for 4EY2, 4EYF, 4RAM, 4RL0 (Table S6). The top clusters are the most reliable according to HADDOCK. The ranking of the clusters is based on the average score of the top 4 members of each cluster. The «ligand interface RMSD» was used to clustered the structures. The statistics on the top cluster is shown in table S7. The L65, M67, F70, W93, H122, Q123, D124, N220, H250 NDM-1 residues were defined as “passive” residues, the two Zn(II) ions as “active” residues and the flavonol as “active” residue (as define in the HADDOCK software). (c) Superimposition of 21 structures over the of the 40 structures clustered in the top clusters generated using the ten art-apo NDM-1 crystallographic structures showing the majority orientation of the morin in the active site of NDM-1 (orientation-1). These 21 structures adopt two slight different orientations in the active site, in 11 dark pink and 10 in light pink. (d) A minority orientation (orientation-2) is also observed in the docking generated structures (on the left: PDB: 4RAM (cluster 2: structure 2 and 3) and 4RBS (cluster 1: structure 4); and on the right: PDB: 4RBS (cluster 1: structures 1 and 3).

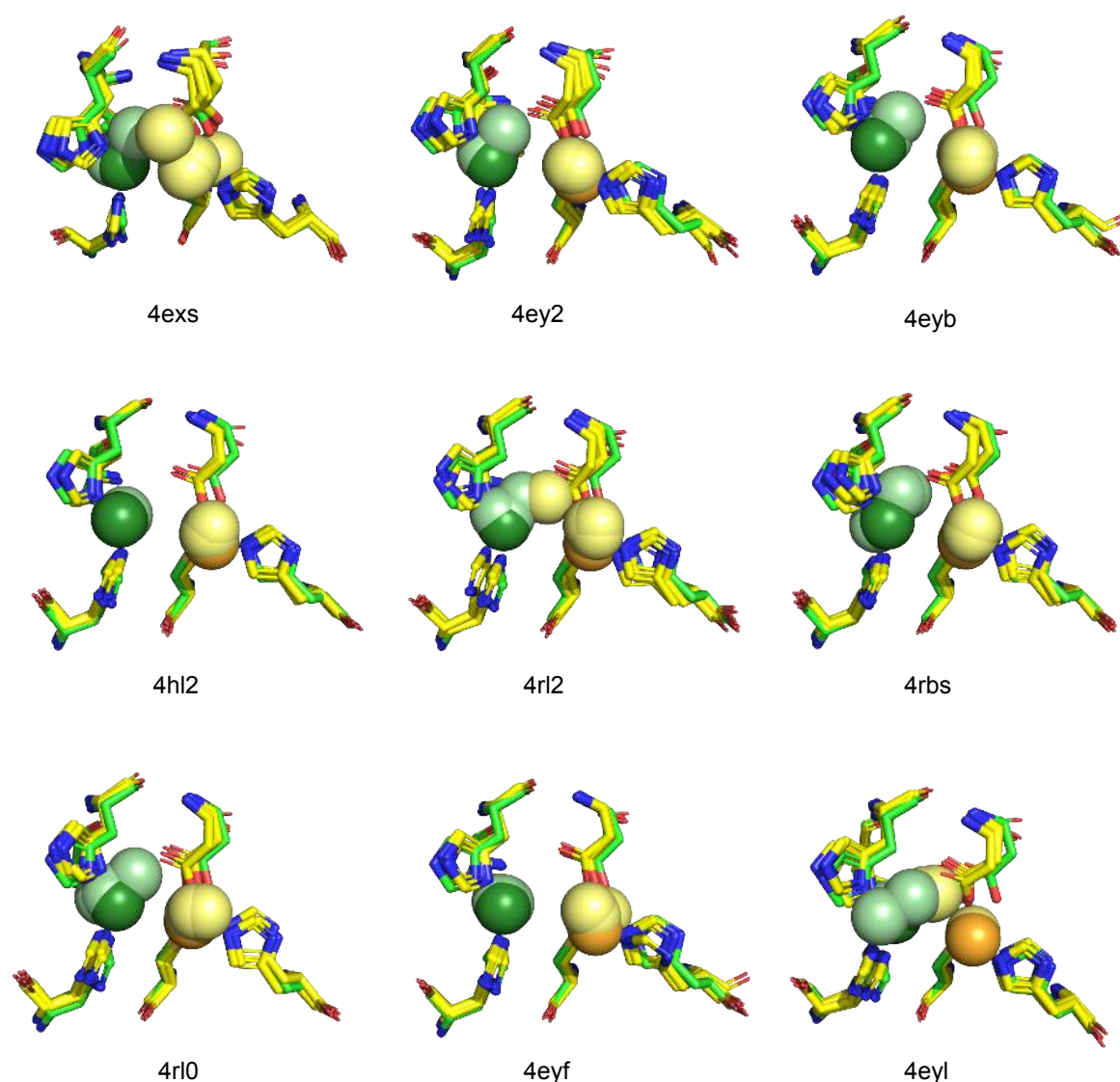
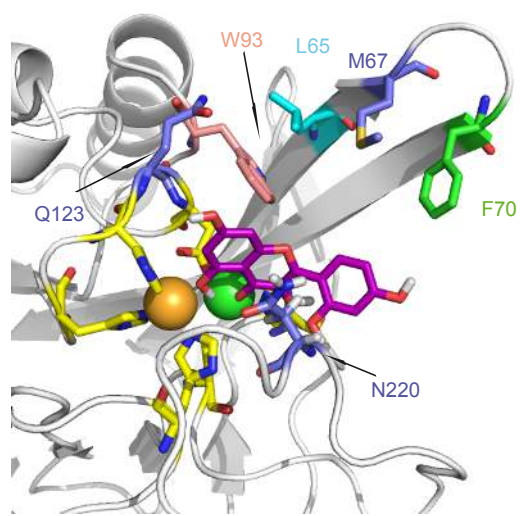
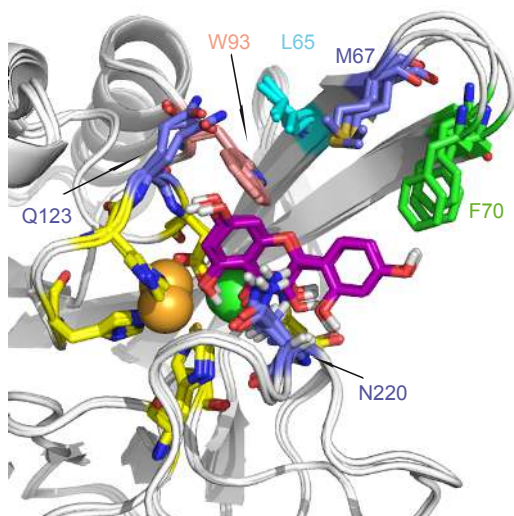


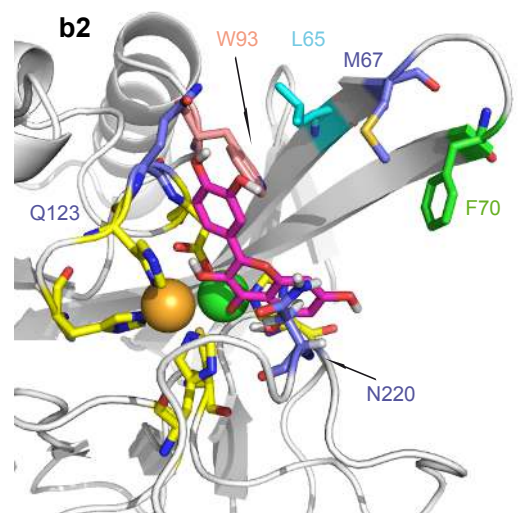
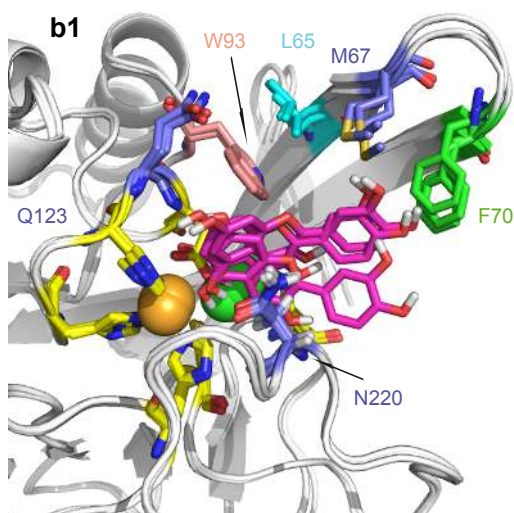
**Figure S19.** Models of the NDM-1/morin complexes generated using the HADDOCK webserver with ten crystal structures of NDM-1 in complex with a ligand: (PDB: 4EXS, 4EY2, 4EYB, 4EYF, 4EYL, 4HL2, 4RAM, 4RBS, 4RL2, 4RL0). All these structures were used for docking after removing of the ligand localized in the active site of the NDM-1 crystallographic structures. The best generated models during the docking simulations, were selected on the basis of the HADDOCK score and shown: clusters 1 for 4EXS, 4EYB, 4EYL, 4HL2, 4RBS, 4RL2 and cluters 2 for 4EY2, 4EYF, 4RAM, 4RL0 (Table S7). The top clusters are the most reliable according to HADDOCK. The ranking of the clusters is based on the average score of the top 4 members of each cluster.

This figure highlights the deviations of Zn1 and Zn2, in the active site, induced by docking with morin, compared to their positions in the starting crystal structures, after superimposition on the (45-271) backbone atoms of the ten art-apo NDM-1 crystal structures and those generated during the docking simulations. Zn1 and Zn2 are in dark green and orange respectively in the crystal structures and in light green and yellow in NDM-1/morin complexes generated using the HADDOCK. The Zn(II) ligands are highlighted by green sticks in the cristal structures and in yellow in the docking generated structures.

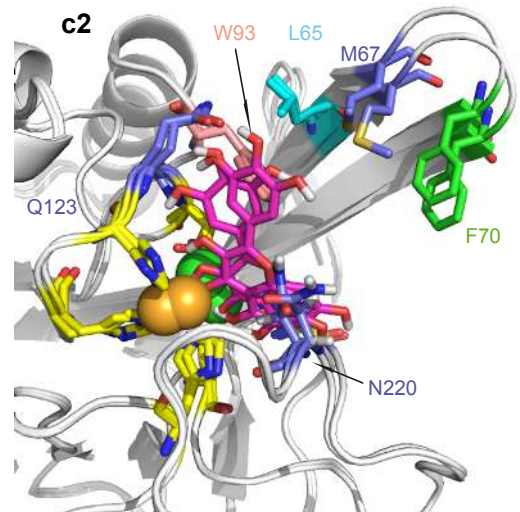
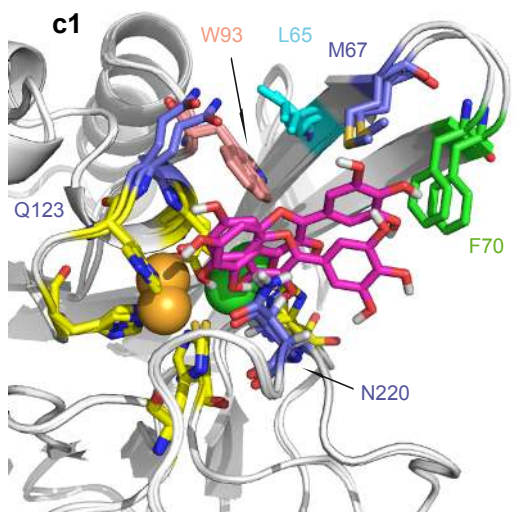
a) PDB: 4EYB + Morin



b) PDB: 4EYB + Quercetin



c) PDB: 4EYB + Myricetin



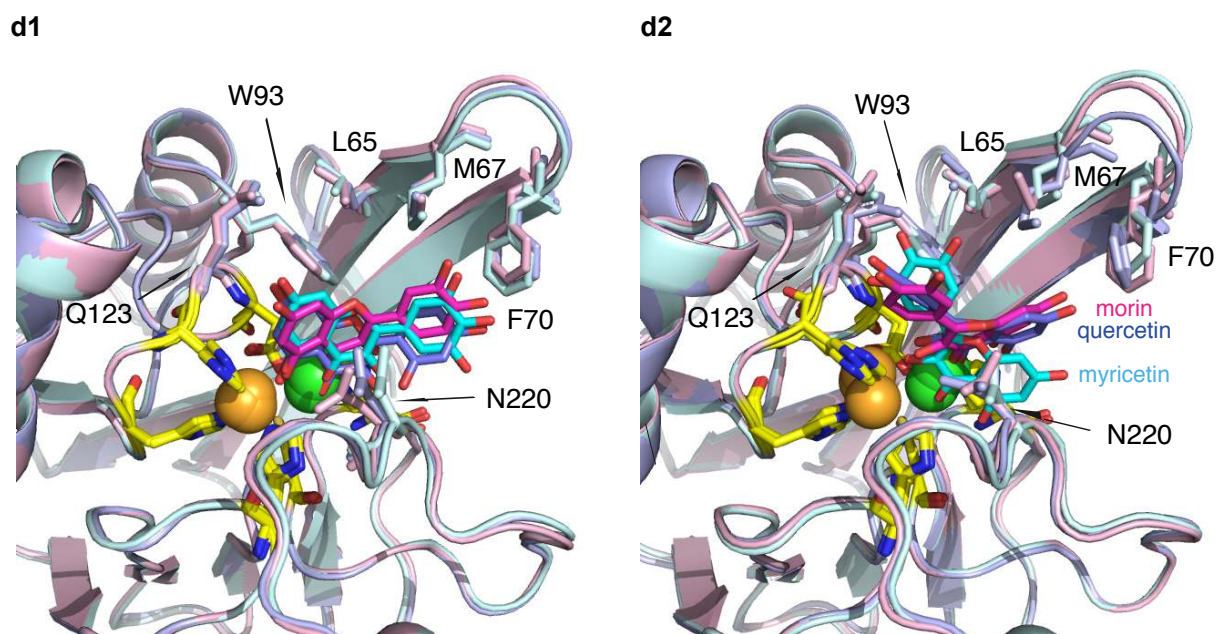


**Figure S20.** Comparison of models of the NDM-1/morin, NDM-1/quercetin and NDM-1/myricetin complexes generated using the HADDOCK. The best generated models during the docking simulations, using the PDB: 4EYB crystallographic structure, were selected on the basis of the HADDOCK scores and shown, in presence of morin (a), quercetin (b) and myricetin (c). While only one orientation (orientation-1) is observed for morin in complex with PDB: 4EYB (a) orientation-1 (b1 and c1) and orientation-2 (b2 and c2), which results from a 180° rotation of the ligand in the active site of NDM-1 from orientation-1, is also observed in presence of quercetin and myricetin. Superimposition on the NDM-1 backbone atoms showing the relative orientation of the three flavonols (morin in pink, quercetin in blue and myricetin in cyan) in orientation-1 (d1) and orientation-2 (d2).

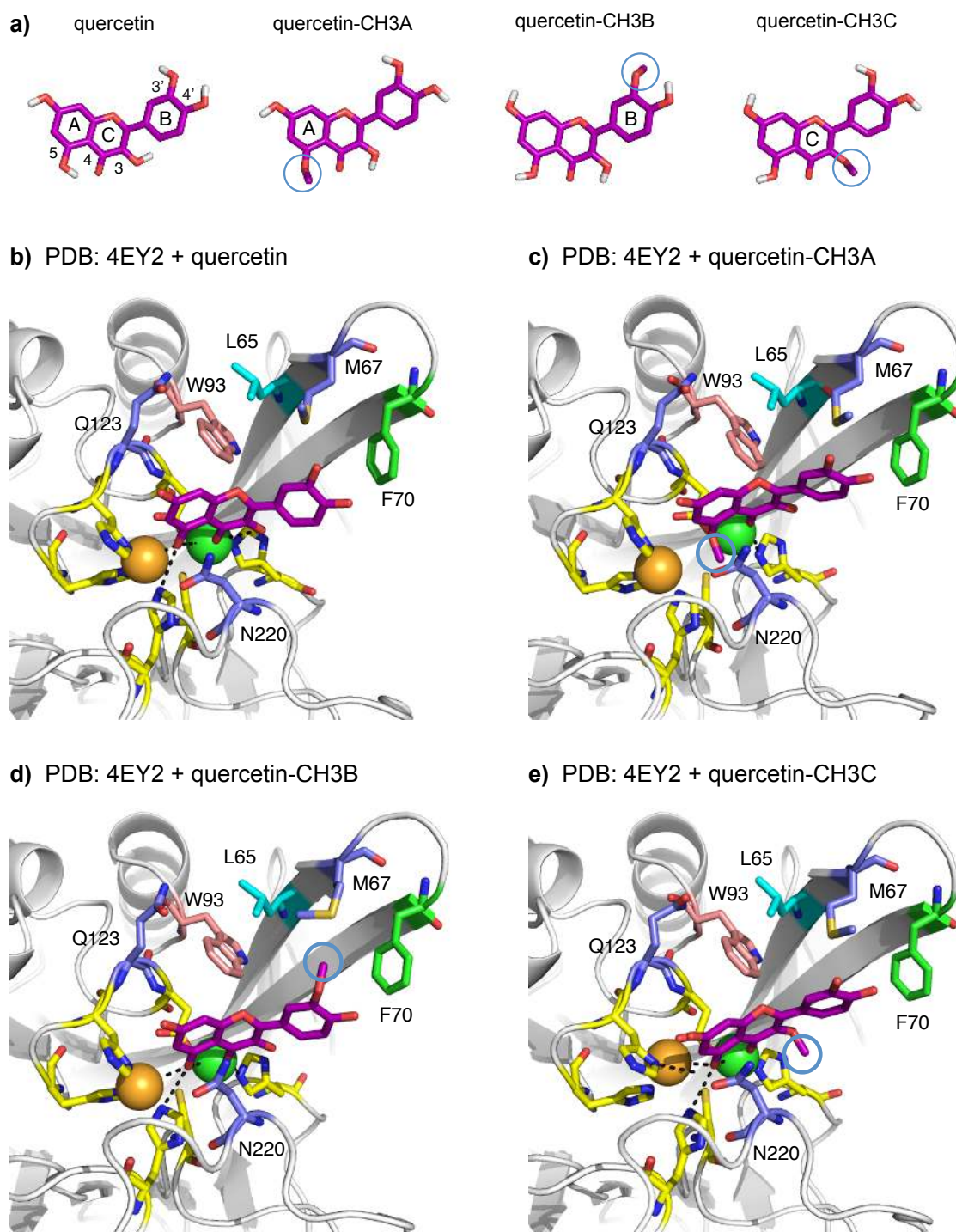


**Figure S21.** Comparison of models of the NDM-1/quercetin and NDM-1/quercetin conjugates generated using HADDOCK. (a) Structures of the quercetin conjugates. The best generated models during the docking simulations, using the PDB: 4EY2 crystallographic structure, were selected on the basis of the HADDOCK scores and shown, in presence of quercetin (b), quercetin with OMe in position 5 (quercetin-CH3A) (c), quercetin with OMe in position 3' (quercetin-CH3B) (d) and quercetin with OMe in position 3 (quercetin-CH3C) (e).

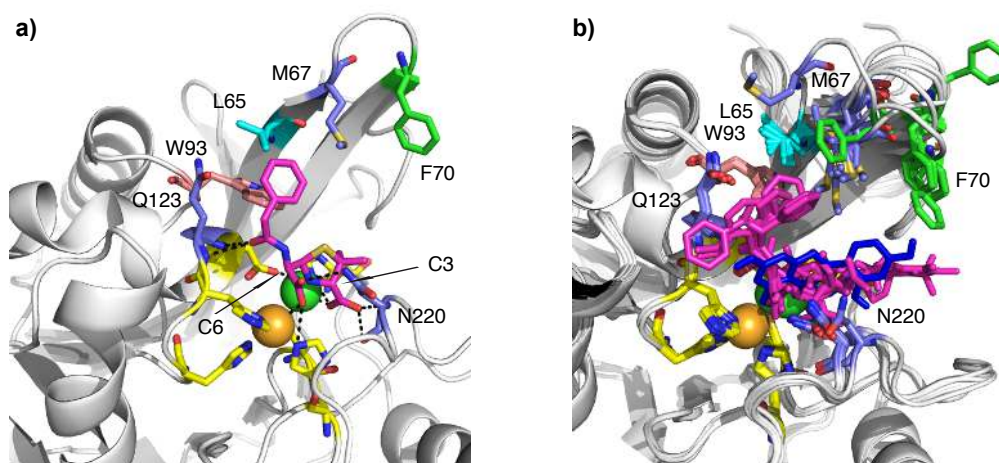


**Figure S22.** NDM-1 ligand interactions. (a) Interaction of the hydrolyzed benzylpenicillin in the NDM-1 active site (PDB: 4EYF). The polar interactions of the ligand with NDM-1 are highlighted by black dash lines. (b) Superimposition of one NDM-1/morin structure obtained after docking with the art-apo NDM-1 PDB:4EYB (morin in dark blue) and the cristallographique structures of NDM-1 in complex with ligand in pink (PDB: 4EY2 (hydrolysed methicillin), 4EYL (hydrolysed meropenem), 4RL0 (hydrolysed cefuroxime), 4RL2 (hydrolysed cefalexin), 4EYB (hydrolysed oxacillin), 4EYF (hydrolysed benzylpenicillin), 4RBS (hydrolysed meropenem), 4HL2 (hydrolysed ampicillin). The residues implicated in the flavonol recognitions are highlighted by sticks. Zn1 is in orange and Zn2 in green.

## Supplemental materials and Methods

### Chemistry synthesis of the compounds: MG188c, MG187c, MG195c, MG194c2 and MG219F3

#### Chemistry synthesis.

All chemical reagents were of analytical grade, obtained from Acros, Alfa Aesar, or Aldrich, and used without further purification. Solvents were obtained from SDS or VWR-Prolabo. Chromatography was performed using silica gel (35-70  $\mu\text{m}$ , Merck). Analytical TLC was performed using Silica Gel 60 F<sub>254</sub> pre-coated aluminum plates (Merck). NMR spectra were collected on Bruker DRX 250 (<sup>1</sup>H at 250 MHz and <sup>13</sup>C at 62.5 MHz), DRX 300 (<sup>1</sup>H at 300 MHz and <sup>13</sup>C at 75 MHz) or DRX 360 (<sup>1</sup>H at 360 MHz and <sup>13</sup>C at 90 MHz) spectrometers and analyzed using MestReNova software. Chemical shifts are reported in ppm ( $\delta$ ) and coupling constants in Hz (*J*). Multiplicity is given as follow: s, singlet; d, doublet; t, triplet; q, quartet; m, multiplet; bs, broad singlet. <sup>1</sup>H NMR spectra were performed in CDCl<sub>3</sub>, (CD<sub>3</sub>)<sub>2</sub>CO, CD<sub>3</sub>OD or D<sub>2</sub>O. High-resolution mass spectrometry (HRMS) analyses were performed by electrospray with positive or negative ionization mode (ESI<sup>+</sup> or ESI<sup>-</sup>).

The synthetic routes are presented on Figures S8, S9 and S10

#### Procedure for benzylation

##### A-Benzoylation of quercetin (Fig. S8)

To a solution of quercetin **1** (CAS 6151-25-3) in anhydrous DMF (*c*=1.9mol/L) under argon and at room temperature were added 4 eq of potassium carbonate (K<sub>2</sub>CO<sub>3</sub>). The solution was then cooled at 0°C for the dropwise addition of 4 eq. of benzylbromide (BnBr). The resulting solution was kept under stirring 1h at 0°C and then allowed to return to room temperature for 15h. AcOEt was added, the resulting solution was washed twice with HCl (1M), with distilled water (until neutral pH) and twice with brine. The organic layer was dried over Mg<sub>2</sub>SO<sub>4</sub> and filtered. The solvent was removed under reduced pressure to give a brown oil. Flash chromatography (silica, elution cyclohexane/acetone, 3/1) yielded to three pure fractions: Tetrabenzylated quercetin (F1, **2a** 14%), Tribenzylated quercetin (F2, **2b** 46%) and Dibenzylated quercetin (F3, 12%).

**2a**: <sup>1</sup>H NMR ((CD<sub>3</sub>)<sub>2</sub>CO): 12.78 (s, 1H, OH 5), 7.88 (d, *J*<sub>1</sub>=2.1, 1H, H2'), 7.72 (d\*d, *J*<sub>1</sub>=2.1, *J*<sub>2</sub>=8.6, 1H, H6'), 7.57-7.21 (m, 21H, Bn and H5'), 6.76-6.74 (m, 1H, H8), 6.47-6.45 (m, 1H, H6), 5.29-5.27 (m, 4H, CH<sub>2</sub>Bn), 5.18 (s, 2H, CH<sub>2</sub>Bn), 5.04 (s, 2H, CH<sub>2</sub>Bn). HRMS *m/z* Found: 663.2354 [M+H]<sup>+</sup>. Calcd for C<sub>43</sub>H<sub>35</sub>O<sub>7</sub>: 663.2377.

**2b**: <sup>1</sup>H NMR (CDCl<sub>3</sub>): 12.68 (s, 1H, OH 5), 7.68-7.62 (m, 1H, H6'), 7.45-7.30 (m, 16H, Bn and H2'), 6.98 (d, *J*=9.2, 1H, H5'), 6.54-6.52 (m, 1H, H8), 6.47-6.45 (m, 1H, H6), 5.71 (s, 1H, OH), 5.18 (s, 2H, CH<sub>2</sub>Bn), 5.11 (s, 2H, CH<sub>2</sub>Bn), 5.04 (s, 2H, CH<sub>2</sub>Bn). HRMS *m/z* Found: 573.1894 [M+H]<sup>+</sup>. Calcd for C<sub>36</sub>H<sub>29</sub>O<sub>7</sub>: 573.1908.

##### B-Benzoylation of Rutin [1] (Fig. S9)

To a solution of dried rutin **7** (CAS 153-18-4) in anhydrous DMF (*c*=1.9mol/L) under argon and at room temperature were added 4.5 eq of cesium carbonate (Cs<sub>2</sub>CO<sub>3</sub>). 6 eq. of benzylbromide (BnBr) were added dropwise to the solution at room temperature. The resulting solution was kept under stirring 16h at room temperature then heated to 60°C for 4 h. The solution was then poured in an ice-cold solution of acetic acid (0.7mol/L). The precipitate was diluted in AcOEt. The resulting solution was washed twice with distilled water and twice with brine. The organic layer was dried over Mg<sub>2</sub>SO<sub>4</sub>. The solvent was removed under reduced pressure to give orange solid. This solid was diluted in ethanolic solution of hydrochloric acid (1.8mol/L) and heated to 75°C for 6h. The mixture was poured into ice-cold distilled water. The precipitate was filtered off and washed with distilled water to yield a bright yellow solid. This solid was then diluted in DCM, the resulting organic layer was dried over MgSO<sub>4</sub> and filtered. The solvent was evaporated under reduced pressure. The title compound **2c** was isolated as a yellow solid after flash chromatography (silica, elution cyclohexane/AcOEt, 85/15 to 80/20) with 32% yield.

**2c**: <sup>1</sup>H NMR (CDCl<sub>3</sub>): 7.88 (d, *J*<sub>1</sub>=1.9, 1H, H2'), 7.78 (d\*d, *J*<sub>1</sub>=1.9, *J*<sub>2</sub>=8.5, 1H, H6'), 7.52-7.31 (m, 20H, Bn), 7.03 (d, *J*<sub>2</sub>=8.6, 1H, H5'), 6.59 (d, *J*=2.0, 1H, H8) 6.48 (d, *J*=1.9, 1H, H6), 5.26-5.24 (m, 6H, CH<sub>2</sub>Bn), 5.12-5.15 (m, 3H, CH<sub>2</sub>Bn et OH3). HRMS *m/z* Found: 663.2369 [M+H]<sup>+</sup>. Calcd for C<sub>43</sub>H<sub>35</sub>O<sub>7</sub>: 663.2377.

#### Procedure for methylation [2] (Fig. S8 and S9)

Benzylated quercetin **2a**, **2b** or **2c** (*c*=0.08mol/L) and 2eq cesium carbonate (Cs<sub>2</sub>CO<sub>3</sub>) were dissolved in anhydrous DMF under argon, Methyl iodide (2eq) was added, and the resulting mixture was stirred at

room temperature and under argon for 16h (**2a**, **2b**) or 24h (**2c**). The mixture was then diluted in DCM and washed with distilled water, diluted HCl (1M), distilled water again and brine. The organic layer was dried over Mg<sub>2</sub>SO<sub>4</sub> and filtered. The solvent was evaporated under reduced pressure.

**3a** was isolated after Flash chromatography (silica, elution cyclohexane/acetone 7/3) with 99% yield. <sup>1</sup>H NMR(CDCl<sub>3</sub>): 7.75 (d, J<sub>1</sub>=1.9, 1H, H2'), 7.56 (d\*d, J<sub>1</sub>=1.9, J<sub>2</sub>=8.6, 1H, H6'), 7.47-7.19 (m, 20H, Bn), 6.95 (d, J<sub>1</sub>=8.6, 1H, H5'), 6.53 (d, J=2.1, 1H, H8), 6.44 (d, J=2.0, 1H, H6), 5.24 (s, 2H, CH<sub>2</sub>Bn), 5.14 (s, 2H, CH<sub>2</sub>Bn), 5.07 (s, 2H, CH<sub>2</sub>Bn), 4.97 (s, 2H, CH<sub>2</sub>Bn), 3.97 (s, 3H, OCH<sub>3</sub>). HRMS *m/z* Found: 677.2525 [M+H]<sup>+</sup>. Calcd for C<sub>44</sub>H<sub>37</sub>O<sub>7</sub>: 676.2461.

**3b** was isolated after Flash chromatography (silica, elution cyclohexane/acetone 9/1 to 8/2) with 50% yield. <sup>1</sup>H NMR (CDCl<sub>3</sub>): 7.63 (d, J<sub>1</sub>=2.1, 1H, H2'), 7.54 (d\*d, J<sub>1</sub>=2.1, J<sub>2</sub>=8.6, 1H, H6'), 7.48-7.23 (m, 15H, Bn), 6.93 (d, J<sub>2</sub>=8.6, H5'), 6.51 (d, J=2.2, 1H, H8), 6.44 (d, J=2.2, 1H, H6), 5.25 (s, 2H, CH<sub>2</sub>Bn), 5.13 (s, 2H, CH<sub>2</sub>Bn), 5.06 (s, 2H, CH<sub>2</sub>Bn), 3.72 (s, 1H, OCH<sub>3</sub>). HRMS *m/z* Found: 609.1874 [M+Na]<sup>+</sup>. Calcd for C<sub>37</sub>H<sub>30</sub>NaO<sub>7</sub>: 609.1884.

**3c** was isolated after Flash chromatography (silica, elution cyclohexane/acetone 7/3) with 98% yield. <sup>1</sup>H NMR (CDCl<sub>3</sub>): 7.77 (d, J<sub>1</sub>=2.0, 1H, H2'), 7.66-7.62 (m, 3H, Bn and H6'), 7.50-7.20 (m, 18H, Bn), 7.02 (d, J<sub>2</sub>=8.6, 1H, H5'), 6.53 (d, J=2.1, 1H, H8), 6.46 (d, J=2.1, 1H, H6), 5.27-5.25 (m, 4H, CH<sub>2</sub>Bn), 5.23 (s, 2H, CH<sub>2</sub>Bn), 5.10 (s, 2H, CH<sub>2</sub>Bn), 3.71 (s, 3H, OCH<sub>3</sub>). HRMS *m/z* Found: 677.2524 [M+H]<sup>+</sup>. Calcd for C<sub>44</sub>H<sub>37</sub>O<sub>7</sub>: 677.2524.

#### Procedure for (3'-O)-alkylation (Fig. S8)

Benzylated quercetin **2b** (c=0.06mol/L in acetone), 12 eq of potassium carbonate, and 0.4 eq of tetrabutylammonium iodide were dissolved in acetone. 4.5 eq of chloromethyl-isopropyl carbonate were added to the mixture then DMF (1/1 to acetone) to solubilize the starting materials. The solution was kept under stirring and at 50°C for 24h. The reaction was quenched by the addition of distilled water and equal volume of DCM. The organic layer was washed with distilled water and brine, the solvent evaporated under reduced pressure and the residue was purified by flash chromatography (silica, elution cyclohexane/acetone 9/1). Compounds **5a** and **5b** (conversion 65%) were co-eluted in these conditions and were not further separated. The proportions of each compound were evaluated by NMR to 60% of **5a** and 40% of **5b**.

**5a+5b**: <sup>1</sup>H NMR (CDCl<sub>3</sub>): 12.70 (**5b**, OH5), 12.69 (**5a**, OH5), 7.92 (d\*d, J<sub>1</sub>=2.1, J<sub>2</sub>=8.7, **5a**, H6'), 7.88 (d, J<sub>1</sub>=2.2, **5a**, H2'), 7.82 (d, J<sub>1</sub>=2.1, **5b**, H2'), 7.73 (d\*d, J<sub>1</sub>=2.2, J<sub>2</sub>=8.7, **5b**, H6'), 7.49-7.21 (m, **5a+5b**, Bn), 7.05 (d, J<sub>2</sub>=8.7, **5a**, H5'), 6.98 (d, J<sub>2</sub>=8.7, **5b**, H5'), 6.53-6.51 (m, **5a+5b**, H8), 6.48-6.46 (m, **5a+5b**, H6), 5.72 (s, **5b**, OCH<sub>2</sub>O), 5.23-5.11 (m, **5a+5b**, CH<sub>2</sub>Bn), 5.04-4.94 (m, **5a**, CH *i*-Pr), 4.95-4.86 (m, **5b**, CH *i*-Pr), 1.34 (d, J=6.2, **5a**, CH<sub>3</sub> *i*-Pr); 1.28 (d, J=6.2, **5b**, CH<sub>3</sub> *i*-Pr). HRMS *m/z* Found: 681.2078 [M+Na]<sup>+</sup> **5a**. Calcd for C<sub>40</sub>H<sub>35</sub>NaO<sub>9</sub>: 681.2095 **5a**. HRMS *m/z* Found: 711.2188 [M+H]<sup>+</sup> **5b**. Calcd for C<sub>41</sub>H<sub>36</sub>NaO<sub>10</sub>: 711.2201 **5b**.

#### Procedure for hydrogenolysis (debenzylation) (Fig. S8 and S9)

Compounds **3a**, **3b**, **3c**, (**5a + 5b**) were all debenzylated by catalytic hydrogenation. Benzylated compound was added to a degassed solution of EtOH/THF (1v/1v) (**3a** or **3b**) or DCM/MeOH (1v/1v) (**3c** and (**5a + 5b**)) containing 5% of Pd/C. The reaction mixture was stirred for 16h under hydrogen atmosphere. The solution was filtered over celite, washed with THF or MeOH and evaporated.

The crude compound **4a** was then washed with Et<sub>2</sub>O and filtered. Pure **4a** was isolated as a yellow solid with 50% yield.

<sup>1</sup>H NMR (CD<sub>3</sub>OD): 7.68 (d, J<sub>1</sub>=1.8, 1H, H2'), 7.58 (d\*d, J<sub>1</sub>=1.8, J<sub>2</sub>=8.4, 1H, H6'), 6.84 (d, J<sub>2</sub>=8.5, 1H, H5'), 6.46 (d, J=1.6, 1H, H8), 6.34 (d, J=1.5, 1H, H6), 3.87 (s, 3H, OCH<sub>3</sub>). HRMS *m/z* Found: 339.0472 [M+Na]<sup>+</sup>. Calcd for C<sub>16</sub>H<sub>12</sub>NaO<sub>7</sub>: 339.0475.

The crude compound **4b** was then washed with Et<sub>2</sub>O and filtered. Pure **4b** was isolated as a dark yellow solid with quantitative yield.

<sup>1</sup>H NMR (CD<sub>3</sub>OD): 7.87 (s, 1H, H2'), 7.74 (d, J=7.4, 1H, H6'), 6.93 (d, J=7.3, 1H, H5'), 6.41 (s, 1H, H8), 6.19 (s, 1H, H6), 3.77 (s, 3H, OCH<sub>3</sub>). HRMS *m/z* Found: 315.0513 [M-H]<sup>+</sup>. Calcd for C<sub>16</sub>H<sub>11</sub>O<sub>7</sub>: 315.0510. The crude compound **4c** was dissolved in chloroform then precipitated with pentane. The precipitate was filtered off and pure **4c** was isolated as a brown/green solid with quantitative yield.

<sup>1</sup>H NMR (CD<sub>3</sub>OD): 7.61 (s, 1H, H2'), 7.52 (d, J=8.4, 1H, H6'), 6.88 (d, J=8.5, 1H, H5'), 6.32 (s, 1H, H8), 6.14 (s, 1H, H6), 3.94 (s, 3H, OCH<sub>3</sub>). HRMS *m/z* Found: 315.0514 [M-H]<sup>+</sup>. Calcd for C<sub>16</sub>H<sub>11</sub>O<sub>7</sub>: 315.0510. The mixture of compounds **6a + 6b** were isolated without further treatment as a dark green solid.

$^1\text{H}$  NMR ( $\text{CD}_3\text{OD}/\text{D}_2\text{O}$ ): 7.99 (s, **5b**, H2'), 7.92-7.88 (m, **5b**, H6'), 7.75 (s, **5a**, H2'), 7.65 (d,  $J_2=8.0$ , **5a**, H6'), 7.06-7.00 (m, **5b**, H5'), 6.93 (d,  $J_2=8.3$ , **5a**, H5'), 6.43-6.40 (m, **5a** + **5b**, H8), 6.19-6.21 (m, **5a** + **5b**, H6), 5.81 (s, **5b**,  $\text{OCH}_2\text{O}$ ), 1.38 (d,  $J=6.1$ , **5b**,  $\text{CH}_3$  *i*-Pr); 1.28 (d,  $J=6.1$ , **5a**,  $\text{CH}_3$  *i*-Pr). The CH *i*-Pr are masked by water residual pic. 6a HRMS  $m/z$  Found: 411.0880  $[\text{M}+\text{Na}]^+$  Calcd for  $\text{C}_{19}\text{H}_{16}\text{NaO}_9$ : 411.0614. and Found : 441.0772  $[\text{M}+\text{Na}]^+$  Calcd for  $\text{C}_{20}\text{H}_{18}\text{NaO}_{10}$ : 441.0792.

#### Synthesis of the oxime of Naringenin (Fig. S10)

Commercially available naringenin **8** (CAS 67604-48-2) was dissolved in EtOH ( $c=0.04\text{mol/L}$ ), 30 eq of aqueous hydroxylamine and 20 eq of pyridine were added. The resulting mixture was stirred at  $65^\circ\text{C}$  for 6h. The reaction mixture was evaporated to dryness and the residue was purified by flash chromatography (silica, elution DCM to DCM/MeOH (2%)) to afford **9** in 52 % yield.

**9**:  $^1\text{H}$  NMR ( $(\text{CD}_3)_2\text{CO}$ ): 11.04 (s, 1H, OH 5), 10.35 (bs, 1H, OH), 8.69 (bs, 1H, OH), 7.41, 7.38, 6.93, 6.89 (Ar Syst AA'BB', 4H, H2' and H3'), 6.01 (d,  $J=2.3$ , 1H, H8), 5.98 (d,  $J=2.3$ , 1H, H6), 5.80 (d\*d,  $J_1=3.1$ ,  $J_2=12.0$ , 1H, H2), 3.47 (d\*d,  $J_1=3.1$ ,  $J_3=17.1$ , 1H, H3a), 3.13 (bs, 1H, OH), 2.79 (d\*d,  $J_2=12.0$ ,  $J_3=17.1$ , 1H, H3b). HRMS  $m/z$  Found: 286.0720  $[\text{M}-\text{H}]^+$ . Calcd for  $\text{C}_{15}\text{H}_{12}\text{O}_5$ : 286.0721.

[1] Vrba J, Gazak R, Kuzma M, Papouskova B, Vacek J, Weissenstein M, et al. A novel semisynthetic flavonoid 7-O-galloyltaxifolin upregulates heme oxygenase-1 in RAW264.7 cells via MAPK/Nrf2 pathway. *J Med Chem.* 2013;56:856-66.

[2] Mattarei A, Biasutto L, Marotta E, De Marchi U, Sassi N, Garbisa S, et al. A mitochondriotropic derivative of quercetin: a strategy to increase the effectiveness of polyphenols. *Chembiochem.* 2008;9:2633-42.

## Supporting Information

### Tables

#### **NMR characterization of the influence of zinc(II) ions on the structural and dynamic behavior of the New-Delhi Metallo- $\beta$ -lactamase-1 and on the binding with flavonols as inhibitors**

Gwladys Rivière,<sup>†</sup> Saoussen Oueslati,<sup>‡</sup> Maud Gayral,<sup>§</sup> Jean-Bernard Créchet,<sup>||</sup> Naïma Nhiri,<sup>†</sup> Eric Jacquet,<sup>†</sup> Jean-Christophe Cintrat,<sup>⊥</sup> François Giraud,<sup>†</sup> Carine van Heijenoort,<sup>†</sup> Ewen Lescop,<sup>†</sup> Stéphanie Pethe,<sup>‡</sup> Bogdan I. Iorga,<sup>†</sup> Thierry Naas,<sup>\*,‡</sup> Eric Guittet,<sup>†</sup> and Nelly Morellet<sup>\*,†</sup>

<sup>†</sup>Institut de Chimie des Substances Naturelles, CNRS UPR 2301, Université Paris-Sud, Université Paris-Saclay, LabEx LERMIT, 1 avenue de la Terrasse, 91190, Gif-sur-Yvette, France;

<sup>‡</sup>EA7361 'Structure, Dynamic, Function and Expression of Broad Spectrum  $\beta$ -Lactamases', Faculty of Medicine, Université Paris-Sud, LabEx LERMIT, Université Paris-Saclay, Le Kremlin-Bicêtre, France.

<sup>§</sup>Institut de Chimie Moléculaire et des Matériaux d'Orsay (ICMMO), CNRS, Univ Paris Sud, Université Paris-Saclay, 15 rue Georges Clemenceau, 91405 Orsay Cedex, France.

<sup>||</sup>Ecole Polytechnique, Route de Saclay, F-91120 Palaiseau, France;

<sup>⊥</sup>Service de Chimie Bio-organique et Marquage (SCBM), CEA, Université Paris-Saclay, LabEx LERMIT, 91191 Gif/Yvette, France.

#### **\*Corresponding Authors:**

Nelly Morellet : E-mail: nelly.morellet@cnsr.fr. phone :(33)169823762. Fax : (33)169823784

Thierry Naas: E-mail: thierry.naas@aphp.fr. phone :(33)145212019 or (33)145213030. Fax : (33)145216340

**Table S1** Effect of Zn(II) on NDM-1 thermal stability. The thermal denaturation temperature of NDM-1 was determined by thermal Shift assay in presence and in absence of EDTA and ZnCl<sub>2</sub>

	ZnCl <sub>2</sub> (μM)						EDTA (mM)
	0	3.12	6.25	12.5	25	50	2.5
Td <sub>1/2</sub> NDM-1 (°C)	40.5±0.3	41.5±0.4	46.6±0.3	49.8±0.2	52.8±0.2	56.2±0.4	41.1±0.3

**Table S2** Average of the relaxation parameters of the flexible and rigid domains of NDM-1

	-Zn(II)	+Zn(II)
		R1 (s <sup>-1</sup> )
RIGID*	0.73 ± 0.08	0.64 ± 0.05
ASL1 (64-74)	0.73 ± 0.06	<b>0.67 ± 0.04</b>
ASL2 (118-123)	Not shown	0.61 ± 0.04
L9 (154-158)	Not shown	0.62 ± 0.04
ASL3 (184-195)	0.74 ± 0.08	0.65 ± 0.05
ASL4 (209-225)	<b>0.85 ± 0.10</b>	<b>0.68 ± 0.06</b>
α3 helix (226-239)	0.75 ± 0.09	0.62 ± 0.05
		R2(s <sup>-1</sup> )
RIGID*	24.22 ± 1.69	31.19 ± 1.27
ASL1 (64-74)	<b>19.73 ± 0.91</b>	<b>25.56 ± 0.67</b>
ASL2 (118-123)	Not shown	30.54 ± 1.18
L9 (154-158)	Not shown	32.40 ± 1.13
ASL3 (184-195)	24.14 ± 2.26	30.45 ± 1.70
ASL4 (209-225)	<b>22.64 ± 1.71</b>	31.01 ± 2.15
α3 helix (226-239)	24.95 ± 1.65	32.28 ± 1.59
		hetNOE
RIGID*	0.87 ± 0.15	0.85 ± 0.12
ASL1 (64-74)	<b>0.65 ± 0.10</b>	<b>0.70 ± 0.09</b>
ASL2 (118-123)	Not shown	0.86 ± 0.13
L9 (154-158)	Not shown	0.84 ± 0.10
ASL3 (184-195)	0.83 ± 0.30	0.87 ± 0.17
ASL4 (209-225)	<b>0.74 ± 0.19</b>	<b>0.82 ± 0.16</b>
α3 helix (226-239)	0.85 ± 0.15	0.87 ± 0.16

RIGID\*: average calculation on the folded domain. The values from the 28-44 (N-terminal domain), 64-74 (ASL1), 118-123 (ASL2), 154-158 (L9), 184-195 (ASL3), 209-225 (ASL4) and 226-239 (α3 helix) were removed from the calculation

**Table S3** LogP estimation of morin, quercetin and myricetin\*

	Morin	Quercetin	Myricetin
Log P	0.35	0.35	-0.04

\* ChemBioDraw was used to predict values for LogP

**Table S4** Estimated Kd values of morin and myricetin in complex with NDM-1

residues	Kd morin ( $\mu\text{M}$ ) (5eq final)	Kd Myricetin ( $\mu\text{M}$ ) (3eq final)
L65	359.2 $\pm$ 35.3	375.4 $\pm$ 66.6
D66	229.5 $\pm$ 23.82	139.6 $\pm$ 48.5
W93	1495 $\pm$ 472	Not determined
Q123	1586.0 $\pm$ 280.8	524.1 $\pm$ 54.5
D124	988.7 $\pm$ 513.1	Not determined
L218	330.8 $\pm$ 68.1	1745.0 $\pm$ 261.4
G222	433.3 $\pm$ 83.7	268.2 $\pm$ 17.1
H250	2136 $\pm$ 436.5	Not determined

**Table S5** Zn1-Zn2 distances in structures of NDM-1 in complex with different products.

PDB number	Product in complex	Zn1-Zn2* distance Å	Zn1-Zn2+ distance Å after docking with morin
<b>4EY2</b>	hydrolyzed methicillin	<b>4.6</b>	Cluster1 (4.0, 4.4, 4.3, 4.5) Cluster2 (4.6, 4.0, 4.6, 4.6)
<b>4EYB</b>	hydrolyzed oxacillin	<b>4.5</b>	Cluster1 (4.3, 4.0, 4.3, 4.4) Cluster2 (4.9, 5.4, 6.7, 4.3)
4EXS	L-captopril	3.6	Cluster1 (4.9, 5.3, 3.6, 5.0) Cluster2 (5.0, 2.6, 2.6, 2.6)
4EYL	hydrolyzed meropenem	4.0	Cluster1 (2.6, 2.6, 3.9, 2.6) Cluster2 (4.3, 2.6, 2.6, 5.1)
4RBS	hydrolyzed meropenem	4.0	Cluster1 (4.2, 4.1, 4.2, 4.9) Cluster2 (4.2, 4.0, 4.4, 4.5)
<b>4EYF</b>	hydrolyzed benzylpenicillin	<b>4.6</b>	Cluster1 (4.2, 4.4, 5.0, 4.4) Cluster2 (4.5, 4.9, 4.4, 4.4)
4RL0	hydrolyzed cephalosporins	3.8	Cluster1 (4.2, 4.3, 4.3, 4.4) Cluster2 (4.2, 4.4, 4.6, 3.9)
4RL2	hydrolyzed cephalosporins	4.5	Cluster1 (4.4, 4.4, 2.6, 5.0) Cluster2 (4.4, 2.6, 3.7, 4.9)
4RAM	hydrolyzed penicillin G	4.1	Cluster1 (4.2, 4.0, 4.4, 4.5) Cluster2 (5.0, 3.9, 4.6, 5.1)
<b>4HL2</b>	hydrolyzed ampicillin	<b>4.6</b>	Cluster1 (4.5, 4.5, 4.5, 4.4) Cluster2 (4.5, 7.1, 4.1, 6.8)

\* Zn1-Zn2 distances measured in ten NDM-1 crystal structures in complex with products.

+ Zn1-Zn2 distances measured in the NDM-1/morin complexes generated using HADDOCK

**Table S6** NDM-1/MORIN docking using the molecular-docking simulations in the data-driven program HADDOCK. The art-apo NDM-1 structures (from PDB: 4EXS, 4EY2, 4EYB, 4EYF, 4EYL, 4HL2, 4RAM, 4RBS, 4RL2, 4RL0) used for docking. The two Zn(II) were not defined as either passive or active residues. Only the results for the top clusters are shown

	4EXS	4EY2	4EYB	4EYF	4EYL	4HL2	4RAM	4RBS	4RL2	4RL0
nb structures	398	392	389	393	390	387	390	395	398	394
nb clusters	3	7	6	6	5	6	6	7	7	6
	<b>Cluster 1</b>	<b>Cluster 2</b>	<b>Cluster 1</b>	<b>Cluster 2</b>	<b>Cluster 2</b>					
HADDOCK score	-58 +/- 9	-75 +/- 4	-71 +/- 3	-74 +/- 3	-74 +/- 1	-75 +/- 3	-71 +/- 2	-75 +/- 3	-68 +/- 2	-64 +/- 4
Cluster size	258	130	83	96	83	94	142	180	115	67
RMSD from the overall lowest-energy structure	0.3 +/- 0.2	0.2 +/- 0.1	0.3 +/- 0.2	0.4 +/- 0.2	0.3 +/- 0.2	0.2 +/- 0.1	0.2 +/- 0.1	0.3 +/- 0.2	0.3 +/- 0.2	0.3 +/- 0.0
Van der Waals energy	-14 +/- 4	-23 +/- 3	-17 +/- 5	-20 +/- 4.0	-18 +/- 2	-19 +/- 5	-19 +/- 4	-17 +/- 5	-20 +/- 5	-21 +/- 4
Electrostatic energy	-9 +/- 4	-47 +/- 18	-63 +/- 18	-25 +/- 28	-30 +/- 34	-80 +/- 39	-61 +/- 45	-64 +/- 19	-36 +/- 37	-44 +/- 49
Desolvation energy	-10 +/- 4	-6 +/- 3	-9 +/- 4	-11 +/- 2	-11 +/- 5.0	-8 +/- 2	-5 +/- 4	-11 +/- 2	-6 +/- 4	-3 +/- 3
Restraints violation energy	0.0 +/- 0.0	0.0 +/- 0.0	0.1 +/- 0.1	0.0 +/- 0.1	0.2 +/- 0.2	0.1 +/- 0.1	0.1 +/- 0.2	0.0 +/- 0.1	0.0 +/- 0.1	0.5 +/- 0.1
Buried Surface Area	348 +/- 74	518 +/- 23	487 +/- 9	513 +/- 17	461 +/- 48	477 +/- 12	479 +/- 17	536 +/- 16	481 +/- 22	526 +/- 35
Z-Score	-1.4	-1.6	-1.9	-1.3	-1.7	-1.6	-1.7	-1.3	-1.5	-1.7

Apo form of NDM-1 (PDB: 4TYF, 3S0Z, 4TZF, 4TZE, 3SPU) used for docking.

	4TYF	3S0Z	4TZF	4TZE	3SPU
nb structures	390	393	398	392	390
nb clusters	9	3	6	5	8
	<b>Cluster 3</b>	<b>Cluster 2</b>	<b>Cluster 2</b>	<b>Cluster 3</b>	<b>Cluster 2</b>
HADDOCK score	-77 +/- 6	-74 +/- 7	-67 +/- 7	-64 +/- 3	-76 +/- 5
Cluster size	54	50	65	49	87
RMSD from the overall lowest-energy structure	0.3 +/- 0.2	0.4 +/- 0.2	0.3 +/- 0.2	0.3 +/- 0.2	0.3 +/- 0.2
Van der Waals energy	-22 +/- 3	-17 +/- 3	-18 +/- 1	-22 +/- 5	-14 +/- 4
Electrostatic energy	-76 +/- 4	-27 +/- 9	-26 +/- 9	-74 +/- 32	-74 +/- 40
Desolvation energy	-4 +/- 2	-21 +/- 3	-5 +/- 3	-2 +/- 4	-7 +/- 5
Restraints violation energy	0.0 +/- 0.0	0.0 +/- 0.0	0.0 +/- 0.0	0.0 +/- 0.0	0.0 +/- 0.0
Buried Surface Area	527 +/- 3	469 +/- 67	440 +/- 16	522 +/- 27	465 +/- 18
Z-Score	-1.6	-1.1	-1.2	-1.4	-2.1

The L65, M67, F70, W93, H122, Q123, D124, N220, H250 NDM-1 residues were defined as “passive” residues and morin as “active” residue.

**The two Zn(II) are not defined as either passive or active residues.**

The **fraction of native contacts (FCC)** clustering were used to clustered the structures.

**nb structures:** is the water-refined models HADDOCK generated

**nb clusters:** is the number of clusters in which all the water-refined models HADDOCK generated are clustered.

**HADDOCK score:** is calculated as function of the intermolecular van der Waals energy, the intermolecular electrostatic energy, the empirical desolvation energy term and the Ambiguous Interaction Restraints (AIRs) energy.

**Z-Score:** indicates how many standard deviations from the average this cluster is located in terms of score.

	3PG4	3RKJ	3RKK	3SBL
nb structures	385	392	389	389
nb clusters	8	6	6	7
	Cluster 4	Cluster 3	Cluster 2	Cluster 2
HADDOCK score	-78 +/- 4	-58 +/- 4	-59 +/- 2	-70 +/- 2
Cluster size	27	36	91	118
RMSD from the overall lowest-energy structure	0.4 +/- 0.2	0.4 +/- 0.0	0.4 +/- 0.0	0.3 +/- 0.0
Van der Waals energy	-18 +/- 3	-13 +/- 4	-21 +/- 2	-21 +/- 4
Electrostatic energy	-35 +/- 20	-9 +/- 8	-14 +/- 4	-15 +/- 5
Desolvation energy	-7 +/- 4	-3 +/- 2	-2 +/- 3	-7 +/- 3
Restrains violation energy	0.0 +/- 0.0	0.0 +/- 0.0	0.0 +/- 0.0	0.0 +/- 0.0
Buried Surface Area	468 +/- 22	404 +/- 28	491 +/- 41	545 +/- 34
Z-Score	-1.7	-1.0	-1.2	-1.4

**Metal-free apo form of NDM-1** (PDB:3PG4, 3RKJ, 3RKK, 3SBL) used for docking.

The L65, M67, F70, W93, H122, Q123, D124, N220, H250 NDM-1 residues were defined as “passive” residues and morin as “active” residue.

There is no zinc ions in these RX structures

**The fraction of native contacts** (FCC) clustering were used to clustered the structures.

**nb structures:** is the water-refined models HADDOCK generated

**nb clusters:** is the number of clusters in which all the water-refined models HADDOCK generated are clustered.

**HADDOCK score:** is calculated as function of the intermolecular van der Waals energy, the intermolecular electrostatic energy, the empirical desolvation energy term and the Ambiguous Interaction Restraints (AIRs) energy.

**Z-Score:** indicates how many standard deviations from the average this cluster is located in terms of score.

**Table S7** NDM-1/MORIN docking using the molecular-docking simulations in the data-driven program HADDOCK. The **art-apo NDM-1 structures** (PDB: 4EXS, 4EY2, 4EYB, 4EYF, 4EYL, 4HL2, 4RAM, 4RBS, 4RL2, 4RL0) used for docking. The two Zn(II) were defined as active residues. Only the results for the top clusters are shown

	4EXS	4EY2	4EYB	4EYF	4EYL	4HL2	4RAM	4RBS	4RL2	4RL0
<b>nb structures</b>	194	195	198	200	186	198	191	197	193	193
<b>nb clusters</b>	4	5	6	4	4	6	5	4	5	4
	<b>Cluster 1</b>	<b>Cluster 2</b>	<b>Cluster 1</b>	<b>Cluster 2</b>	<b>Cluster 1</b>	<b>Cluster 1</b>	<b>Cluster 2</b>	<b>Cluster 1</b>	<b>Cluster 1</b>	<b>Cluster 2</b>
<b>HADDOCK score</b>	-83 +/- 3	-81 +/- 4	-79 +/- 1	-79 +/- 2	-82 +/- 7	-81 +/- 3	-78 +/- 6	-78 +/- 2	-78 +/- 5	-70 +/- 2
<b>Cluster size</b>	85	74	107	71	70	71	65	155	65	74
<b>RMSD from the overall lowest-energy structure</b>	0.4 +/- 0.0	0.3 +/- 0.2	0.5 +/- 0.0	0.4 +/- 0.0	0.2 +/- 0.1	0.3 +/- 0.2	0.2 +/- 0.2	0.4 +/- 0.0	0.3 +/- 0.2	0.3 +/- 0.1
<b>Van der Waals energy</b>	-19 +/- 5	-18 +/- 6.0	-15 +/- 3	-17 +/- 3	-17.4 +/- 0.2	-16.4 +/- 0.4	-18 +/- 6	-20 +/- 7	-15 +/- 3	-15 +/- 4
<b>Electrostatic energy</b>	-64 +/- 26	-61 +/- 20	-70 +/- 4	-55 +/- 24	-107 +/- 21	-77 +/- 5	-48 +/- 28	-68.8 +/- 9.0	-84.8 +/- 21.4	-73.8 +/- 0.8
<b>Desolvation energy</b>	-8.0 +/- 3.1	-11.1 +/- 1.4	-11.5 +/- 1.6	-14.1 +/- 0.9	-11.0 +/- 1.9	-10.7 +/- 2.1	-8.0 +/- 2.3	-9 +/- 2	-4 +/- 1	-3 +/- 3
<b>Restraints violation energy</b>	0.2 +/- 0.2	0.1 +/- 0.1	0.1 +/- 0.1	0.0 +/- 0.1	0.1 +/- 0.2	0.0 +/- 0.1	0.4 +/- 0.5	0.0 +/- 0.1	0.1 +/- 0.1	0.5 +/- 0.4
<b>Buried Surface Area</b>	486 +/- 12	501 +/- 12	494 +/- 14	493 +/- 16	495 +/- 33	509 +/- 18	491 +/- 25	527 +/- 30	481 +/- 5	491 +/- 24
<b>Z-Score</b>	-0.9	-1.3	-1.7	-0.7	-1.0	-1.3	-1.1	-1.5	-1.6	-1.2

Apo form of NDM-1 (PDB: 4TYF, 3S0Z, 4TZF, 4TZE, 3SPU) used for docking.

	4TYF	3S0Z	4TZF	4TZE	3SPU
nb structures	197	195	188	193	200
nb clusters	4	5	4	5	5
	Cluster 2	Cluster 1	Cluster 2	Cluster 1	Cluster 3
HADDOCK K score	-80 +/- 9	-89 +/- 4	-75 +/- 4	-76 +/- 3	-76 +/- 3
Cluster size	34	105	53	110	26
RMSD from the overall lowest-energy structure	0.2 +/- 0.1	0.5 +/- 0.1	0.3 +/- 0.2	0.4 +/- 0.1	0.3 +/- 0.2
Van der Waals energy	-23 +/- 5	-22 +/- 1	-22 +/- 6	-22 +/- 2	-15 +/- 4
Electrostatic energy	-78 +/- 31	-0.0 +/- 2.3	-95 +/- 32	-73 +/- 36	-28 +/- 36
Desolvation energy	-7 +/- 2	-24 +/- 3	-5 +/- 4	-1 +/- 2	-14 +/- 5
Restraints violation energy	0.2 +/- 0.3	1.5 +/- 1.2	0.7 +/- 0.7	0.0 +/- 0.1	0.8 +/- 0.4
Buried Surface Area	542 +/- 9	537 +/- 17	530 +/- 20	528 +/- 7	463 +/- 36
Z-Score	-1.1	-0.9	-1.2	-1.2	-1.1

L65, M67, F70, W93, H122, Q123, D124, N220, H250 NDM-1 residues were defined as “passive” residues and morin as “active” residue.

The two Zn(II) were defined as “active” residues.

The «ligand interface RMSD» was used to cluster the structures.

**nb structures:** is the number of water-refined models HADDOCK generated

**nb clusters:** is the number of clusters in which all the water-refined models HADDOCK generated are clustered.

**HADDOCK score:** is calculated as function of the intermolecular van der Waals energy, the intermolecular electrostatic energy, the empirical desolvation energy term and the Ambiguous Interaction Restraints (AIRs) energy.

**Z-Score:** indicates how many standard deviations from the average this cluster is located in terms of score.

**Table S8** Rmsd calculated on the morin atoms after superimposition on the (45-271) backbone atoms of the ten art-apo NDM-1 structures after docking simulation.

PDB number	rmsd cluster 1 (A)	rmsd cluster 2 (A)
4EY2	1.2 ± 0.3	<b>1.1 ± 0.7</b>
4EYB	<b>0.8 ± 0.2</b>	4.2 ± 3.5
4EXS	<b>5.4 ± 2.4</b>	3.5 ± 2.9
4EYL	<b>3.2 ± 3.5</b>	6.6 ± 0.2
4RBS	<b>3.6 ± 3.1</b>	6.1 ± 2.0
4EYF	1.0 ± 0.4	<b>1.4 ± 0.2</b>
4RL0	0.7 ± 0.3	<b>1.1 ± 0.4</b>
4RL2	<b>2.6 ± 2.4</b>	3.5 ± 2.9
4RAM	1.1 ± 0.7	<b>5.0 ± 3.0</b>
4HL2	<b>0.6 ± 0.4</b>	3.6 ± 2.5

The rmsd were calculated within each cluster for cluster 1 and cluster 2 for each PDB starting structures.

The top cluster of each series is in bold (either the cluster 1 or the cluster 2 depending on the PDB starting structures); the ranking of the clusters is based on the average score of the top 4 members of each cluster. The HADDOCK score is calculated as function of the intermolecular van der Waals energy, the intermolecular electrostatic energy, the empirical desolvation energy term and the Ambiguous Interaction Restraints (AIRs) energy.

**Table S9 NDM-1/QUERCETIN** docking using the molecular-docking simulations in the data-driven program HADDOCK.

quercetin	4EXS	4EY2	4EYB	4EYF	4EYL	4HL2	4RAM	4RBS	4RL2	4RL0
nb structures	194	200	194	193	198	193	198	200	199	194
nb clusters	3	4	3	3	5	4	4	5	5	4
	Cluster 2	Cluster 1	Cluster 1	Cluster 2	Cluster 1	Cluster 2	Cluster 2	Cluster 1	Cluster 2	Cluster 1
<b>HADDOCK score</b>	-85 +/- 6	-80 +/- 3	-77 +/- 4	-83 +/- 1	-78 +/- 1.0	-82 +/- 5	-75 +/- 6	-77 +/- 2	-74 +/- 4	-69 +/- 4
<b>Cluster size</b>	78	131	85	71	83	75	45	118	59	87
<b>RMSD from the overall lowest-energy structure</b>	0.4 +/- 0.2	0.4 +/- 0.0	0.3 +/- 0.2	0.3 +/- 0.2	0.4 +/- 0.1	0.4 +/- 0.2	0.4 +/- 0.1	0.5 +/- 0.1	0.3 +/- 0.2	0.3 +/- 0.2
<b>Van der Waals energy</b>	-15 +/- 2	-12 +/- 1	-15 +/- 4	-17 +/- 4	-17 +/- 3	-15 +/- 2	-18 +/- 5	-15 +/- 2	-14 +/- 1	-15 +/- 3
<b>Electrostatic energy</b>	-117 +/- 5	-72 +/- 5	-72 +/- 3	-51 +/- 34	-111 +/- 7	-79 +/- 5	-63 +/- 20	-74 +/- 2	-80 +/- 12	-90 +/- 22
<b>Desolvation energy</b>	-9 +/- 3	-11 +/- 1	-11 +/- 4	-12 +/- 2	-8 +/- 3.0	-11 +/- 3	-8 +/- 2	-9 +/- 3	-4 +/- 3	-4 +/- 3
<b>Restraints violation energy</b>	0.1 +/- 0.1	0.0 +/- 0.0	0.1 +/- 0.1	0.1 +/- 0.2	0.1 +/- 0.0	0.2 +/- 0.3	9.4 +/- 14.9	0.1 +/- 0.1	0.3 +/- 0.3	0.7 +/- 0.2
<b>Buried Surface Area</b>	499 +/- 12	468 +/- 17	484 +/- 11	485 +/- 14	489 +/- 33	486 +/- 36	470 +/- 23	507 +/- 13	453 +/- 18	505 +/- 21
<b>Z-Score</b>	-1.3	-1.6	-1.1	-1.2	-0.9	-1.6	-1.2	-0.8	-1.1	-0.9

The "artificial apo" NDM-1 structures (PDB: 4EXS, 4EY2, 4EYB, 4EYF, 4EYL, 4HL2, 4RAM, 4RBS, 4RL2, 4RL0) used for docking

The two Zn(II) were defined as active residues. Only the results for the top clusters are shown.

-The L65, M67, F70, W93, H122, Q123, D124, N220, H250 NDM-1 residues were defined as "passive" residues and quercetin as "active" residue.

-The «**ligand interface RMSD**» was used to clustered the structures.

-**nb structures:** is the water-refined models HADDOCK generated  
**-nb clusters:** is the number of clusters in which all the water-refined models HADDOCK generated are clustered.

**Table S10 NDM-1/MYRICETIN** docking using the molecular-docking simulations in the data-driven program HADDOCK.

MYRICETIN	4EXS	4EY2	4EYB	4EYF	4EYL	4HL2	4RAM	4RBS	4RL2	4RL0
nb structures	199	198	197	198	194	198	198	196	198	198
nb clusters	5	5	4	5	5	5	4	3	5	5
	Cluster 2	Cluster 1	Cluster 1	Cluster 1	Cluster 2	Cluster 1	Cluster 2	Cluster 1	Cluster 3	Cluster 2
HADDOCK score	-85 +/- 4	-77 +/- 8	-77 +/- 2	-82 +/- 2	-82 +/- 4	-82 +/- 3	-78 +/- 4	-78 +/- 2	-73 +/- 5	-73 +/- 4
Cluster size	70	92	104	94	55	85	76	103	26	77
RMSD from the overall lowest-energy structure	0.2 +/- 0.1	0.2 +/- 0.2	0.5 +/- 0.1	0.5 +/- 0.1	0.3 +/- 0.2	0.3 +/- 0.2	0.3 +/- 0.2	0.3 +/- 0.1	0.3 +/- 0.2	0.2 +/- 0.1
Van der Waals energy	-13 +/- 3	-15 +/- 2	-15 +/- 5	-16 +/- 2	-15 +/- 2	-15 +/- 3	-15 +/- 3	-20 +/- 3	-15 +/- 5	-17 +/- 4
Electrostatic energy	-120 +/- 5	-71 +/- 3	-84 +/- 25	-83 +/- 21	-107 +/- 21	-83 +/- 22	-80 +/- 19	-60 +/- 17	-71 +/- 40	-89 +/- 27
Desolvation energy	-11 +/- 4	-10 +/- 3	-8 +/- 2	-11 +/- 1	-6 +/- 3	-9 +/- 3	-7 +/- 3	-9 +/- 2	-5 +/- 2	-3 +/- 4
Restraints violation energy	0.0 +/- 0.1	0.0 +/- 0.0	0.1 +/- 0.1	0.0 +/- 0.0	0.1 +/- 0.1	0.1 +/- 0.1	0.3 +/- 0.2	0.0 +/- 0.0	0.3 +/- 0.1	0.5 +/- 0.2
Buried Surface Area	486 +/- 27	514 +/- 23	483 +/- 30	511 +/- 19	499 +/- 28	462 +/- 24	486 +/- 18	534 +/- 14	460 +/- 16	509 +/- 13
Z-Score	-1.0	-1.0	-1.1	-1.4	-1.2	-1.2	-0.8	-1.2	-0.9	-1.2

The "artificial apo" NDM-1 structures (PDB: 4EXS, 4EY2, 4EYB, 4EYF, 4EYL, 4HL2, 4RAM, 4RBS, 4RL2, 4RL0) used for docking.

The two Zn(II) were defined as active residues. Only the results for the top clusters are shown.

-The L65, M67, F70, W93, H122, Q123, D124, N220, H250 NDM-1 residues were defined as "passive" residues and myricetin as "active" residue.

-The «ligand interface RMSD» was used to cluster the structures.

-nb structures: is the water-refined models HADDOCK generated

-nb clusters: is the number of clusters in which all the water-refined models HADDOCK generated are clustered.

**Table S11 NDM-1/QUERCETIN and QUERCETIN derivatives** docking using the molecular-docking simulations in the data-driven program HADDOCK. In CH3A, CH3B and CH3C an OCH3 group replace 3'OH, 3OH and 5OH respectively  
The "artificial apo" NDM-1 structures (PDB: 4EYB and 4EY2) used for docking. The two Zn(II) were defined as active residues. Only the results for the top clusters are shown.

4EYB	quercetin	CH3A	CH3B	CH3C		4EY2	quercetin	CH3A	CH3B	CH3C
nb structur	194	196	197	196		nb structur	200	200	196	196
nb clusters	3	4	4	4		nb clusters	4	5	4	3
	Cluster 1	Cluster 1	Cluster 2	Cluster 1			Cluster 1	Cluster 1	Cluster 2	Cluster 1
HADDOCK score	-77 +/- 4	-79 +/- 3	-78 +/- 4	-80 +/- 3		HADDOCK score	-79 +/- 3	-78 +/- 1	-75 +/- 2	-81 +/- 3
Cluster size	85	120	71	119		Cluster size	131	124	74	100
RMSD from the overall lowest-energy structure	0.3 +/- 0.2	0.3 +/- 0.0	0.3 +/- 0.2	0.6 +/- 0.1		RMSD from the overall lowest-energy structure	0.4 +/- 0.0	0.4 +/- 0.0	0.3 +/- 0.2	0.4 +/- 0.2
Van der Waals energy	-15 +/- 4	-13 +/- 2	-12 +/- 5	-23 +/- 5		Van der Waals energy	-12 +/- 1	-12 +/- 4	-11 +/- 2	-18 +/- 5
Electrostatic energy	-71 +/- 3	-75 +/- 7	-73 +/- 4	-42 +/- 29		Electrostatic energy	-72 +/- 6	-76 +/- 7	-70 +/- 5	-47 +/- 33
Desolvation energy	-11 +/- 4	-11 +/- 2	-10 +/- 2	-14 +/- 5		Desolvation energy	-11 +/- 1	-11 +/- 2	-11 +/- 3	-13 +/- 5
Restraints violation energy	0.1 +/- 0.1	0.1 +/- 0.2	0.1 +/- 0.1	0.5 +/- 0.4		Restraints violation energy	0.0 +/- 0.0	0.4 +/- 0.4	0.1 +/- 0.1	0.5 +/- 0.4
Buried Surface Area	484 +/- 11	511 +/- 15	497 +/- 13	533 +/- 6		Buried Surface Area	468 +/- 17	527 +/- 31	506 +/- 20	517 +/- 12
Z-Score	-1.1	-1.1	-1.1	-0.9		Z-Score	-1.6	-1.5	-1.5	-1.0

-The L65, M67, F70, W93, H122, Q123, D124, N220, defined as "passive" residues and quercetin as "active" residue.  
-The «ligand interface RMSD» was used to clustered the structures.  
-nb structures: is the water-refined models HADDOCK generated  
-nb clusters: is the number of clusters in which all the water-refined models HADDOCK generated are clustered.

## References

- (1) Yao, C., Wu, Q., Xu, G. & Li, C. (2017) NMR backbone resonance assignment of New Delhi metallo-beta-lactamase, *Biomol NMR Assign.* **11**, 239-242.
- (2) Piotto M, Saudek V, Sklenar V. Gradient-tailored excitation for single-quantum NMR spectroscopy of aqueous solutions. *J Biomol NMR.* 1992; 2: 661-665